“Growth and characterization of doped and undoped lithium niobate and lithium tetraborate crystals in bulk and nano form”

By
SUJAN KAR
Enrolment number PHYS03200904007
Crystal Growth Lab, LMDDD

Raja Ramanna Centre for Advanced Technology

Indore-452013

A thesis submitted to the

Board of Studies in Physical Sciences

In partial fulfillment of requirements for the Degree of

DOCTOR OF PHILOSOPHY

Of

HOMI BHABHA NATIONAL INSTITUTE

August 2016

Homi Bhabha National Institute

Recommendation of viva voce committee

As member of Viva Voce board, we certify that we have read the dissertation prepared by **Sujan Kar** entitled **"Growth and characterization of doped and undoped lithium niobate and lithium tetraborate crystals in bulk and nano form"** and recommend that it may be accepted as fulfilling the dissertation requirement for the degree of Doctor of Philosophy.

Date: 20/03/2017
Chairman- Dr. S. B. Roy

KSBartwal
Date: 20/03/2017
Guide - Dr. K. S. Bartwal

Date: 20/03/2017
Member 1 Dr. T. K. Sharma

Date: 20/03/2017
Member 2 Dr. Sangeeta

SGanesamoorthy
Date: 20/03/2017
Member 3 Dr. S. Ganesamoorthy

Date: 20/03/2017
External Examiner- Dr. S. Moorthy Babu

Final approval and acceptance of this dissertation is contingent upon the candidate's submission of the final copies of the dissertation to HBNI. I hereby certify that I have read this dissertation prepared under my direction and recommend that it may be accepted as fulfilling the dissertation requirement.

Guide: KSBartwal
(Dr. K. S. Bartwal)

Date: 20/3/17

Place: RRCAT, Indore

STATEMENT BY AUTHOR

This dissertation has been submitted in partial fulfillment of requirements for an advanced degree at Homi Bhabha National Institute (HBNI) and is deposited in the Library to be made available to borrowers under rules of the HBNI.

Brief quotations from this dissertation are allowable without special permission, provided that accurate acknowledgment of source is made. Requests for permission for extended quotation from or reproduction of this manuscript in whole or in part may be granted by the Competent Authority of HBNI when in his or her judgment the proposed use of the material is in the interests of scholarship. In all other instances, however, permission must be obtained from the author.

August 2016 **Sujan Kar**

DECLARATION

I, hereby declare that the investigation presented in the thesis has been carried out by me. The work is original and has not been submitted earlier as a whole or in part for a degree /diploma at this or any other Institution / University.

August 2016 **Sujan Kar**

List of publications

A. International Journals:

1. **S. Kar**, Sunil Verma, K.S. Bartwal, Growth Optimization and Optical Characteristics of Fe Doped $LiNbO_3$ Crystals, Cryst. Growth Design **8** (2008) 4424-4427.

2. **S. Kar**, Sunil Verma, M.W. Shaikh, K.S. Bartwal, Effect of proton exchange and annealing on diffraction efficiency of Fe:$LiNbO_3$ crystals, Physica B **404** (2009) 3507–3509.

3. **S. Kar**, Sunil Verma, M.S. Khan, K.S. Bartwal, Growth and optical homogeneity investigations on Fe and Fe-Mn cooped lithium niobate crystals, Cryst. Res.Technol. **44** (2009) 1303-1307.

4. **S. Kar**, Sunil Verma, and K.S. Bartwal, Structural and optical investigations on Mn doped LBO crystals, Cryst. Res.Technol. **44** (2009) 305-308.

5. **S. Kar**, Sunil Verma, K.S. Bartwal, Preparation of Mn doped $Li_2B_4O_7$ nanoparticles by glass quenching, J. Alloy and Compounds **495** (2010) 388-391.

6. **S. Kar,** S. Bairagi, C. Debnath, S. Verma, K.S. Bartwal, Thermoluminescence studies on γ-irradiated Mn: $Li_2B_4O_7$ single crystals, Appl. Phys. Lett.**101** (2012) 071904.

7. **S. Kar,** S. Logad, O.P. Choudhury, C. Debnath, S.Verma, K.S. Bartwal, Preparation of lithium niobate nanoparticles by high energy ball milling and their characterization, Universal J. Materials Science **1** (2013) 18-24.

8. **S. Kar**, L. A. Joseph, C. Debnath, S. Verma, V.P. Dhamgaye, G.S. Lodha , K.S. Bartwal, New scheme for dual readout of dose in polycrystalline $Li_2B_4O_7$ irradiated with synchrotron X-rays from Indus-2, Radiat. Meas. **67** (2014) 55-58.

9. **S. Kar**, L. A. Joseph, C. Debnath, S. Verma, V.P. Dhamgaye, G.S. Lodha, K.S. Bartwal, Thermoluminescence studies on single crystal, polycrystalline and glass lithium tetraborate samples irradiated by X-rays from Indus-2, Physica B **456** (2015) 1-4.

B. Seminars:

1. **S. Kar**, S. Verma, M.W. Shaikh, K.S. Bartwal, Influence of proton exchange and annealing on holographic properties of Fe doped lithium niobate crystal, International Conference on Fiber Optics & Photonics (PHOTONICS - 2008), IIT Delhi, Dec., 15-17, 2008.
2. **S. Kar**, S. Verma, K.S. Bartwal, Growth and characterization of Mn doped LBO crystals, National Symposium on Growth of Detector-Grade Single Crystals, BARC Mumbai, Nov., 19-21, 2009.
3. **S. Kar**, S.Verma, M.S. Khan, K.S.Bartwal, P.K.Gupta, Growth and photorefractive characteristics of doubly doped lithium niobate crystals, 13th National Seminar on Crystal Growth, SSN College of Engg., Chennai, Jan. 27-29, 2009.
4. **S. Kar,** Sunil Verma, K.S. Bartwal, P.K. Gupta, Thermoluminescence characteristics of Mn doped $Li_2B_4O_7$ single crystals, DAE-BRNS National Laser Symposium, RRCAT Indore, Dec.1-4, 2010.
5. Sunil Verma, **S. Kar**, K.S. Bartwal, P.K. Gupta, Holographic data storage properties of single (Fe) and double (Fe, Mn) doped congruent lithium niobate crystal, DAE-BRNS National Laser Symposium, RRCAT Indore, Dec.1-4, 2010.
6. **S. Kar**, C. Debnath, S. Verma, K.S. Bartwal, P.K. Gupta, Thermoluminescence studies on glass and crystalline samples of $Li_2B_4O_7$, DAE BRNS National Laser Symposium, Anna University, Chennai, Jan. 9-12, 2012.
7. **S. Kar**, L.A. Joseph, C. Debnath, S. Verma, V.P. Dhamgaye, G.S. Lodha, K.S. Bartwal, P.K. Gupta, Thermoluminescence studies on undoped and doped $Li_2B_4O_7$ single crystals irradiated with synchrotron X- rays from Indus-2, DAE BRNS National Laser Symposium, Manipal University, 2014.

Dedicated to Ma and Baba

Acknowledgments

During my PhD at LMDDD, RRCAT I would like to acknowledge the several people who were the driving force for the completion of my thesis.

I bestow my heartiest gratitude to my guide Dr. K.S. Bartwal for his excellent scientific knowledge and appropriate guidance that helped me to carry out this work. It has been my pleasure working with him. I greatly appreciate the time he spent with me in the past few years.

I am extremely grateful to Dr. P.K. Gupta, Head, LMDDD for allowing me to carry out the research works for the Ph.D. degree. As a chairman of doctoral committee, Dr. P.K. Gupta has given me various suggestion and critical comments which helps me to improve my level of understanding. I greatly appreciate the time he spent with me during my synopsis writing.

I am extremely thankful to Dr. Sunil Verma for his guidance and valuable suggestion during the thesis work. I did many of the optical experiment of my thesis work with the help of him. To my benefits, he has made me more critical on scientific and technical issues.

I am also grateful to my expert of doctoral committee Dr. S. B. Roy for his valuable comments and suggestion during my all yearly presentation. Questions asked by him during presentation made me think in some new direction.

I would also like to thank other members of my doctoral committee, Dr. Sangeeta and Dr. S. Ganesh Moorthy for their critical comments and suggestions regarding my thesis work.

I would also like to thank Dr. A. K. Karnal, Head, Laser Materials Section for his support during my PhD.

I express my special thanks to all faculty member of HBNI who taught me during my course work.

I would like to show my gratitude to all teachers to whom I was associated from my primary stage up to the journey of PhD.

I express heartfelt thanks to, Dr. Rajeev Bhatt, Dr. Indranil Bhoumik, Dr. Gurvinderjit Singh, Dr. M.K. Singh, S.K. Sharma, Chiranjeet Debnath, Dr. V.P. Dhamgaye for scientific discussion regarding my thesis work.

I am thankful to the valuable technical supports provided by Yash Pal Sigh, S. R. Markam, Prem Kumar, S.R. Bagade, B.K. Sajith, S.M. Sharma, Amit Saxena. These people extended their support during my experimental work whenever it was needed.

I would like to thank all the other members of LMDDD with special mention to, Dr. V.S.

Tiwari, Dr. S.M. Gupta, Sanjeev Karmakar, S.K. Pathak, Dr. S. Satpathy, Rachana Selvamani. I am also thankful to all my friends and well-wishers in RRCAT.

Acknowledgment would not become complete if I don't mention the contribution of my parent. I would like to thank my parents for their moral support and motivation during my thesis work.

Special thanks go to my wife (Shraboni) and children (Sayan and Sourin) for their constant support and encouragement during my PhD.

I express my thanks to all other family member who directly or indirectly motivate me to complete my PhD.

Sujan Kar

Contents

Page No

Synopsis XVIII-XX

List of figures XXI-XXIV

List of tables XXV

Chapter 1: Introduction and overview 1-31

1.1 Historical background 1

1.2 Growth of single crystals 1-14

1.2.1 The thermodynamics of crystal growth 1

1.2.2 Nucleation 2-3

1.2.3 Crystal growth theories 3-5

A. Surface energy theory 3

B. Diffusion theory 4

C. Surface nucleation model theory 4

D. Screw dislocation theory 5

1.2.4 Crystal growth techniques 5-14

A. Growth from solid 6

B. Growth from vapor 6

C. Growth from melt 7-13

D. Growth from solution 13-14

1.3 Nanoparticles and preparation techniques 14-18

1.3.1 Definition of nanoparticles 14

1.3.2 Preparation techniques 15-18

A. Physical method 15

B. Chemical method 15-16

I. High energy ball milling 16-18

II. Melt quenching 18

1.4 Photo refractive effect **18-21**
1.4.1 Mechanism of the photo refractive effect **19-20**
1.4.2 Desirable properties of PR materials **20-21**
1.4.3 Materials perspective **21**
1.5 Thermoluminscence (TL) **22-29**
1.5.1 Basic principle **22-23**
1.5.2 Important properties of a TL dosimeter **24-25**
1.5.3 Materials perspective **25-29**
References **29-31**

Chapter 2: Characterization techniques **32-49**

2.1 X-ray diffraction **32-34**
2.1.1 Introduction **32**
2.1.2 Working principle **32-33**
2.1.3 Peak shape analysis **33-34**
A. Instrumental broadening **33**
B. Size broadening **33**
C. Strain broadening **34**
2.1.4 Application **34**
2.2 High resolution X-ray diffraction **34-35**
2.2.1 Introduction **34**
2.2.2 Working principle **34-35**
2.2.3 Application **35**
2.3 Transmission electron microscopy **36-39**
2.3.1 Introduction **36**
2.3.2 Sample preparation **36**
2.3.3 Working principle **37-38**
2.3.4 Component of TEM **38-39**
2.3.5 Imaging in TEM **39**
2.3.6 Application **39**
2.4 Scanning electron microscopy **39-41**

2.4.1 Introduction **39**

2.4.2 Sample preparation **40**

2.4.3 Working principle **40-41**

2.4.4 Component of TEM **41**

2.4.5 Application **41**

2.5 UV-Visible transmission spectra **41-43**

2.5.1 Introduction **41**

2.5.2 Working principle of UV-VIS spectrometer **42**

2.5.3 Application **43**

2.6 Dynamic light scattering **43-45**

2.6.1 Introduction **44**

2.6.2 Sample preparation **44**

2.6.3 Working principle **44-45**

2.6.4 Component of DLS **45**

2.6.5 Limitation **45**

2.6.6 Application **45**

2.7 Thermoluminescence study **46-47**

2.7.1 Introduction **46**

2.7.2 Working principle **46-47**

2.7.3 Application **47**

2.8 Birefringence interferometry study **47-48**

2.8.1 Introduction **47**

2.8.2 Working principle **47-48**

2.8.3 Application **48**

2.9 Conoscopic study **48-49**

2.9.1 Introduction **48**

2.9.2 Working principle **48-49**

2.9.3 Application **49**

References **49**

Chapter 3: Growth and characterization of undoped and doped lithium niobate crystals **50- 72**

3.1 Introduction **50-54**

3.1.1 Structure of lithium niobate **50-51**

3.1.2 Phase diagram **52**

3.1.3 Problems arises during growth of good quality crystal **53**

3.1.4 Material potential **53-54**

3.2 Growth of undoped and doped lithium niobate crystals **54-60**

3.2.1 Material Synthesis **54-55**

3.2.2 Crystal Growth **55-60**

3.3 Characterization of grown crystals **60-66**

3.3.1 XRD study **61**

3.3.2 UV-VIS transmission spectra **62-63**

3.3.3 Birefringence Interferometry **63-64**

3.3.4 Conoscopic study **64-65**

3.3.5 Etch pit study **65-66**

3.4 Photorefractive study of as grown and proton exchanged sample **66-70**

3.4.1 Preparation of Proton Exchanged sample **66-67**

3.4.2 Measurement of photorefractive properties of LN crystal by two wave coupling **67-70**

3.5 References **71-72**

Chapter 4: Growth and characterization of doped and undoped lithium tetraborate crystals **73- 86**

4.1 Introduction **73-75**

4.1.1 Structure **73-74**

4.1.2 Material Potential **75**

4.2 Growth of undoped and doped lithium tetraborate crystal **76-78**

4.2.1 Material synthesis **76**

4.2.2 Crystal growth experiment **76-78**

4.3 Characterization of grown crystals 78-85
4.3.1 XRD and HRXRD study 78-80
4.3.2 Etching study of grown crystal 81
4.3.3 UV-VIS transmission spectra 82
4.3.4 Birefringence Interferometry 83
4.3.5 Conoscopy study 83-84
4.3.6 Hardness measurement 84-85
References 85-86

Chapter 5: Thermoluminescence studies on irradiated doped and undoped lithium tetraborate single crystal, polycrystal and glass 87-123

5.1 Introduction 87-93
5.1.1 Basic concept of thermoluminescence 87
5.1.2 Mathematical description 87-89
A. First order kinetics 88-89
B. Second order kinetics 89
5.1.3 Kinetic parameters of TL material 90-91
A. Order of kinetics 90
B. Activation energy 91
C. Frequency factor 91
5.1.4 Lithium tetraborate as thermoluminescence material 91-93
5.2 TL studies on gamma irradiated Mn: LTB single crystal 93-100
5.2.1 Determination of kinetic parameters 94-96
5.2.2 Calculation of activation energy from UV-VIS transmission spectra 96-98
5.2.3 Mass dependency of TL spectra 98
5.2.4 Dose dependency, sensitivity and fading 99
5.2.5 Fading study 99-100
5.3 TL studies of X-ray irradiated undoped and doped LTB glass 100-107
5.3.1 Sample preparation 100-101
5.3.2 Sample irradiation 101

5.3.3 TL glow curve of undoped, Mn doped and Cu doped glass **101-105**
A. Determination of order of kinetics from glow curve **103-104**
B. Determination of activation energy and frequency factor **104-105**
5.3.4 Transmission spectra of irradiated Mn doped LTB glass **106**
5.3.5 Fading study of irradiated LTB glass sample **106-107**
5.4 TL studies of X-ray irradiated undoped and doped LTB polycrystalline pallet **107-116**
5.4.1 Sample preparation **107**
5.4.2 Sample irradiation **108**
5.4.3 TL glow curve of Mn doped and Cu doped LTB pallet **108-111**
A. Determination of order of kinetics from glow curve **109-111**
B. Determination of activation energy and frequency factor **111**
5.4.4 TL glow curve of Mn doped LTB poly crystalline pallet at different heating rate **112**
5.4.5 Dual reading of irradiated undoped and doped LTB pallets **112-114**
5.4.6 Fading studies of irradiated pallets **114-116**
5.5 TL studies of X-ray irradiated undoped and doped LTB single crystal **116-121**
5.5.1 Sample preparation **116**
5.5.2 Sample irradiation **116**
5.5.3 Studies of TL glow curve of irradiated sample **117-121**
A. Determination of order of kinetics from glow curve **118-119**
B. Determination of activation energy and frequency factor **119-121**
5.6 Comparison of TL intensity of undoped LTB, Mn doped LTB and Cu doped LTB single crystal, poly crystal and glass samples **121**
References **122-123**

Chapter 6: Synthesis and characterization of lithium niobate and lithium tetraborate nanoparticles 124-141

6.1 Introduction **124-125**

6.2 Synthesis and characterization of lithium niobate nanoparticles by high energy ball milling **125-132**

6.2.1 Synthesis of lithium niobate nanoparticles by high energy ball milling **125-126**

6.2.2 Characterizations lithium niobate nanoparticles **126-132**

A. X-ray diffraction **126-127**

B. Dynamic light scattering **128**

C. Scanning electron microscopy **128-129**

D. Transmission electron microscopy **129-130**

E. UV-VIS transmission spectra **130**

F. SHG study of lithium niobate nanoparticles dispersed in glass **131-132**

6.3 Synthesis and characterization of lithium tetraborate nanoparticle by high energy ball milling **133-137**

6.3.1 Synthesis of lithium tetraborate nanoparticle by high energy ball milling **133**

6.3.2 Characterization of lithium tetraborate nanoparticle by high energy ball milling **133-137**

A. X-ray diffraction **133-134**
B. Transmission electron microscopy **135**
C. Dynamic light scattering **135-136**
D. TL study **136-137**

6.4 Synthesis of lithium tetraborate nanoparticle by melt quenching technique and characterization **137**

6.4.1 Synthesis of lithium tetraborate nanoparticle by melt quenching technique and characterization **137-138**

6.4.2 Characterization of lithium tetraborate nanoparticle by melt quenching technique and characterization **138-141**

A. X-ray diffraction **138-139**

B. Scanning electron microscopy **139-140**

C. Transmission electron microscopy **140-141**

References **141**

Chapter 7: Conclusions **142-144**

Synopsis

"Growth and characterization of doped and undoped lithium niobate and lithium tetraborate crystals in bulk and nano form"

Oxide crystals ($LiNbO_3$ and $Li_2B_4O_7$) are technologically important materials, because of their broad transmission range (UV to far infrared), excellent electro optic, acousto optic, piezoelectric, pyroelectric and non linear optical properties. These materials are being widely used as electro optic modulator, holographic data storage device, pyroelectric temperature sensor, harmonic generator of Nd:YAG laser, and for thermoluminescence dosimetry of X-ray, gamma ray and neutron radiation. Present thesis reports the growth and characterization of doped and undoped lithium niobate and lithium tetraborate crystals in bulk and nano form and investigations of their use for some applications of current interest.

Lithium niobate crystals were grown by Czochralski technique. Good optical quality and almost uniform diameter crystals were grown by optimizing various growth parameters like pulling rate, rotation rate, post growth cooling rate, temperature gradient of the furnace, and crystal to crucible diameter ratio. Because Lithium niobate is an incongruently melting material and undergoes phase transition at 1160 °C which is very close its melting point (1260 °C), therefore precise control of growth parameters was needed to ensure that imperfection is not introduced inside the crystal during post growth cooling. As one of the major objective of the thesis was to grow lithium niobate crystals suitable for holographic data storage, LN crystals were also grown with Fe doping because the latter is known to enhance its photorefractive properties. Photorefractive properties of the grown crystals were studied by two wave coupling method using a He-Ne laser. The use of proton exchange on doped crystals to enhance its photorefractive properties has also been investigated. It was observed that diffraction efficiency increases significantly (~ 20%) in case of proton exchanged samples.

Doped and undoped lithium tetraborate crystals (LTB) were grown by Cz technique. By careful optimization of growth parameters, good optical quality crystals of size 25 mm dia and 35 mm length were obtained. The main objective of growing LTB crystals was to investigate the use of these for dosimetry applications because LTB is a very good tissue equivalent material. Effective atomic number of LTB is 7.3 which is very close to that of soft biological tissue (Z_{eff}= 7.42). Kinetic parameters such as order of kinetics, activation energy and frequency factors were measured from the TL glow curve of irradiated sample. It was found that compared to polycrystalline material single crystals of LTB show a large variation in TL intensity even with a small variation in the sample mass. Further, because the two TL peaks were observed to be well separated in a temperature span, the system can be used to read the TLD badge twice. The first peak is used to measure the dose immediately and second peak is used to measure the dose in future.

Because the growth of single crystals is a costly and demanding exercise we have also investigated the possibility of the use of nanoparticles of these materials embedded in a suitable polymers as an alternative to single crystals. Lithium niobate and lithium tetraborate nanoparticles were prepared by high energy ball milling and characterized for phase and particle size. These were embedded in glass matrix and the SHG properties of the composite were investigated.

The present thesis is divided into seven chapters as discussed below.

Chapter 1 of the thesis deals with various techniques for crystal growth and nanoparticles synthesis. Basic principles of photorefractive effect, thermoluminescence phenomena and materials perspective are discussed briefly.

Chapter 2 of the thesis describes working principle of different characterization techniques used in the present work such as UV-VIS spectro-photometer, Powder XRD, HRXRD, DLS, TEM, etc. are discussed.

Chapter 3 of the thesis deals with growth and characterization of doped and undoped lithium niobate crystals. Various parameters were optimized to get crack free, transparent, uniform diameter crystals. Optical qualities of the grown crystals were checked by UV-Vis spectro-photometer and conoscopy pattern. Photorefractive studies on proton exchanged Fe:LN sample was done and compared with the as grown sample. It was observed that in proton exchanged samples diffraction efficiency increases by ~ 20 %.

Chapter 4 of the thesis deals with growth and characterization of doped and undoped lithium tetraborate $Li_2B_4O_7$ single crystals. Optimization of growth parameters such as pulling rate, rotation rate, etc are discussed in this chapter. Grown crystals were studied for phase by XRD. Crystalline perfection of grown crystal is examined by HRXRD rocking curve. For optical quality UV-Vis transmission spectra and conoscopy pattern were studied. As lithium tetraborate (LTB) is a very good TLD material, the extensive study of TL properties of doped and undoped LTB is discussed in next chapter.

Chapter 5 of the thesis describes the thermoluminescence studies of irradiated doped and undoped single crystals, polycrystalline pallet and glass. Determination of various kinetic parameters such as order of kinetics, activation energy and frequency factors are discussed. Mass sensitivity of single crystal TLD material is discussed, which is a crucial parameter for making dosimeter. High mass sensitivity of single crystal arises because of the absence of grain boundaries. In the TL glow curves for undoped and doped polycrystalline pallets, two well separated peaks were present. The first peak is from 50 °C to 210 °C and the second peak is from 210 °C to 320 °C. The area under the first and second peaks was measured separately. A new scheme developed for dual reading of TLD badge is discussed in detail in this chapter.

Chapter 6 of the thesis deals with synthesis of lithium niobate and lithium tetraborate nanoparticles by high energy ball milling. Optimization of milling parameters such as milling time, rotation rate, ball to powder mass ratio are discussed. Phase of the synthesized particles were checked by XRD. Particle sizes were calculated from DLS and TEM. The synthesized nanoparticles were examined by UV-Vis spectro-photometer for determination of UV cut off. Blue shift in UV cut off was found which is due to increase in band gap in nano material. The nanoparticles were embedded in glass matrix and the SHG properties of the composite were investigated.

Chapter 7 of the thesis presents the conclusion of the work done. Good quality lithium niobate and lithium tetraborate crystals were grown by Cz technique. Photorefractive properties of Fe doped lithium niobate crystals were studied and enhanced diffraction efficiency was observed in proton exchanged Fe doped lithium niobate sample. TL intensity from single crystal was observed to be highly mass sensitive. Taking consideration of this mass sensitivity, more accurate dose measurement is possible. Based on the observation of two well separated TL peaks A new scheme of dual reading of TLD badge has been proposed. It is hoped that this new method of dual read out scheme will make the material more useful for personal dosimetry.

List of Figures

Page No

Fig. 1.1 Free energy change of nucleus as a function of radius **2**

Fig. 1.2 Possible lattice site for attachment of adsorbed atom. A- terrace site, B-Ledge site, C- kink site **4**

Fig. 1.3 Development of spiral during crystal growth **5**

Fig. 1.4 Schematic representation of natural and forced convective flow in crucible **9**

Fig. 1.5 Schematic diagram of a typical mechanism of ball milling **16**

Fig. 1.6 Mechanism of formation of refractive index grating inside a PR material **19**

Fig. 1.7 Energy band model showing the electronic transitions in a TL material according to a simple two-level model **23**

Fig. 2.1 Ray diagram of diffracted X-rays **32**

Fig. 2.2 Ray diagram of HRXRD instrument **35**

Fig. 2.3 Ray diagram for rocking curve measurement **35**

Fig. 2.4 Ray diagram of TEM **37**

Fig. 2.5 Basic ray diagram of scanning electron microscope **40**

Fig. 2.6 Ray diagram of UV-VIS spectrometer **42**

Fig. 2.7 Ray diagram of DLS **44**

Fig. 2.8 Block diagram of TLD reader **46**

Fig 2.9 Ray diagram of birefringence setup **48**

Fig 2.10 Ray diagram for conoscopy study **49**

Fig. 3.1 (a)The ideal lithium niobate with the chain Li–Nb–vacancy, Li–Nb–vacancy (b) One single octahedra **51**

Fig. 3.2 Phase diagram of Li_2O- Nb_2O_5 system **52**

Fig. 3.3 Heat flow mechanism in melt and crystal **56**

Fig. 3.4 Zirconia bricks, muffle and crucibles **56**

Fig. 3.5 Axial temperature gradient of the furnace (a) above the melt level and (b) below the melt **57**

Fig. 3.6 Seed crystal with alumina rod **57**

Fig. 3.7 Crystal growth system used for CZ method **58**

Fig. 3.8 Photograph of (a) undoped (b) Fe doped and (c) Fe: Mn doped LN crystals **58**

Fig. 3.9 Position of melt level with time **59**

Fig. 3.10 Photograph of uniform diameter Fe: LN crystal **60**

Fig. 3.11 Polished sample of (a) undoped LN (b) Fe doped LN (c) Fe: Mn doped LN **61**

Fig. 3.12 Powder XRD pattern for (a) undoped $LiNbO_3$ (b)Fe doped (c) Fe: Mn doped $LiNbO_3$ crystal **61**

Fig. 3.13 UV-VIS Transmission spectra of (a) undoped LN (b) Fe: LN (c) Fe: Mn: LN sample **63**

Fig. 3.14 Photograph of the birefringence interferometry set up **64**

Fig. 3.15 Birefringence interferogram for (a) Fe: $LiNbO_3$ crystal plate and (b) Fe: Mn: LN crystal plate **64**

Fig. 3.16 Photograph of polarizing microscope **65**

Fig. 3.17 Conoscopic pattern of (a) Fe doped LN, and (b) Fe: Mn doped LN **65**

Fig. 3.18 Etch pits of (a) Fe doped LN (b) Fe: Mn doped LN crystal (Magnification =300 x) **66**

Fig. 3.19 Proton exchanged setup **67**

Fig. 3.20 Optical set up for photorefractive experiment **68**

Fig. 3.21 Ray diagram for two wave coupling **68**

Fig. 3.22 Diffraction efficiency for an as-grown (a) Fe: LN sample (b) Fe: Mn: LN sample **69**

Fig. 3.23 Diffraction efficiency of (a) Fe: LN sample (b) Fe: Mn: LN sample after and before proton exchange **70**

Fig. 4.1 Main crystal motif of lithium tetraborate consisting of two basic elements **74**

Fig. 4.2 The Czochralski growth system used for LTB growth **77**

Fig. 4.3 Axial temperature gradient of the furnace **77**

Fig. 4.4 Photograph of grown crystals (a) undoped LTB (b) Mn doped LTB (c) Cu doped LTB **78**

Fig. 4.5 Photograph of grown LTB crystals with modified gradient **78**

Fig. 4.6 XRD pattern of (a) undoped LTB, (b) Mn doped LTB and (c) Cu doped LTB **79**

Fig. 4.7 High Resolution X-ray diffraction curves recorded for (004) planes of $Li_2B_4O_7$ crystal **80**

Fig. 4.8 Etch pits on LTB plate (a) etched for 1 min., (b) etched for 40 sec, and (c) etched for 20 sec. Magnification for all (300 x) **81**

Fig. 4.9 Transmission spectra of (a) undoped LTB crystal (b) Mn doped LTB crystal (c) Cu doped LTB crystal **82**

Fig. 4.10 Birefringence interferogram for Undoped LTB crystal **83**

Fig. 4.11 Conoscopy pattern of undoped LTB crystal **84**

Fig. 4.12 Indentation mark on face of the LTB crystal plate **85**
Fig. 5.1 General TL glow curve **90**
Fig. 5.2 Polished crystal pieces **93**
Fig. 5.3 Thermoluminescece reader analyzer (model-RA 04) **93**
Fig. 5.4 Thermoluminescence spectra of gamma irradiated Mn: LTB single crystal **94**
Fig. 5.5 TL curves with various heating rate **95**
Fig. 5.6 Plot of ln (T_m^2/β) vs1/T_m (at 2 kgray) **96**
Fig. 5.7 Transmittance of Mn LTB before and after γ-irradiation **96**
Fig. 5.8 Plot of $(\alpha h\nu)^2$ vs $h\nu$ **97**
Fig. 5.9 Mass dependence of TL intensity **98**
Fig.5.10 Dose dependency of TL intensity of Mn: LTB single crystal **99**
Fig.5.11 Fading studies of irradiated Mn: LTB single crystal **100**
Fig. 5.12 Photograph of undoped and doped glass plate **101**
Fig. 5.13 TL glow curve of undoped, Mn doped and Cu doped glass **102**
Fig. 5.14 Glow curve of (a) undoped (b) Mn doped (c) Cu doped LTB glass with T_1, T_2 and T_m **103**
Fig. 5.15 Plot of ln(I) vs 1/T for (a) undoped LTB glass (b) Mn doped LTB glass and (c) Cu doped LTB glass **105**
Fig. 5.16 Transmission spectra of irradiated Mn: LTB glass **106**
Fig. 5.17 Fading study of irradiated (a) Mn doped LTB glass sample and (b) Cu doped LTB glass sample **107**
Fig. 5.18 Photograph of undoped, Mn doped and Cu doped LTB polycrystalline pallet **107**
Fig. 5.19 TL spectra of undoped, Mn doped and Cu doped LTB pallets (per mg) **108**
Fig. 5.20 Plot of 1/T vs ln(I) for (a) first peak (b) second peak of polycrystalline undoped, Mn doped and Cu doped pallet **111**
Fig. 5.21 TL glow curve of Mn: LTB pallets at various heating rates **112**
Fig. 5.22 Dual reading of dosimeter; TL curve in whole temperature range (a),TL curve for temperature range 50-210 °C (b), TL curve for second time reading of same sample from 50-320 °C (c) **114**
Fig. 5.23 TL glow curves for (a) undoped LTB pallets (b) Mn doped LTB pallet (c) Copper doped LTB pallet on same day and after 36 days of irradiation **115**
Fig. 5.24 TL glow curve of X-ray irradiated (a) Undoped, (b) Mn doped and (c) Cu doped LTB single crystal **117**
Fig. 5.25 Plot of ln(I) Vs 1/T for undoped LTB single crystal for peak I **120**

Fig. 5.26 Plot of ln(I) Vs 1/T for Mn doped LTB single crystal of (a) peak I and (b) peak II **120**
Fig. 5.27 Plot of ln(I)Vs 1/T for Cu doped LTB single crystal for (a) peak I and (b) peak II **120**
Fig. 6.1 Photograph of high energy ball milling machine **126**
Fig. 6.2 XRD pattern of high energy ball milling at different milling time **127**
Fig. 6.3 DLS study of lithium niobate nanoparticles **128**
Fig. 6.4 SEM images of $LiNbO_3$ nanocrystals ball milled at 700 rpm for 8h **129**
Fig. 6.5 TEM images of $LiNbO_3$ nanocrystals ball milled at 700 rpm for 8 h in (a) normal image and (b) high resolution mode. The corresponding SAED patterns are inserted into the micrographs **129**
Fig. 6.6 Transmission spectra of (a) LN nanoparticles (b) bulk crystal **130**
Fig. 6.7 LN nanoparticles dispersed LTB glass **131**
Fig. 6.8 Transmission spectra of lithium niobate nanoparticle dispersed in LTB glass **131**
Fig. 6.9 Block diagram of SHG setup **132**
Fig. 6.10 Photograph of (a) SHG setup (b) Measured SHG signal **132**
Fig. 6.11 XRD pattern of ball milled Cu: LTB powder **134**
Fig. 6.12 TEM micrograph of LTB nanoparticles **135**
Fig. 6.13 Size distribution of lithium niobate nanoparticle **136**
Fig. 6.14 TL glow curve of Cu: LTB (a) polycrystalline pallet and (b)pallet of nanoparticles **137**
Fig. 6.15 Photograph of quenched LTB glass **138**
Fig. 6.16 XRD pattern of LTB glass annealed at different temperature **139**
Fig. 6.17 SEM micrograph for LTB sample annealed at (a) 450 °C and (b) 570 °C **140**
Fig. 6.18 HRTEM bright field micrograph for the glass sample annealed at (a) 490 °C and (b) 570 °C **140**

List of Tables

		Page No
Table 1.1	Values for the response of a number of TL materials to a fluence of 10^{10} thermal neutrons/ cm^2 in terms of an equivalent exposure to ^{60}Co gamma rays.	**28**
Table 1.2	Various properties of different TLD material	**29**
Table 3.1	Recording time, erasing time, diffraction efficiency of crystal sample before and after proton exchange	**70**
Table 5.1	Calculation of symmetry factor of undoped, Mn doped and Cu doped glass	**104**
Table 5.2	Activation energy and frequency factor of undoped, Cu doped and Mn doped	**105**
Table 5.3	Calculation of geometric factor for undoped LTB pallet	**109**
Table 5.4	Calculation of geometric factor for Mn doped LTB pallet	**110**
Table 5.5	Calculation of geometric factor for Cu doped LTB pallet	**110**
Table 5.6	Activation energy and frequency factor of undoped, Cu doped and Mn doped LTB pallet	**111**
Table 5.7	Fractional area under peak-I and peak-II for undoped, Mn doped and Cu doped LTB pallets	**113**
Table 5.8	Calculated symmetry factor for Mn doped LTB single crystal from glow curve	**118**
Table 5.9	Calculated symmetry factor for Cu doped LTB single crystal from glow curve	**119**
Table 5.10.	Activation energy and frequency factor of undoped, Mn doped and Cu doped single crystal	**121**
Table 5.11	TL counts of doped and undoped LTB glass, polycrystalline pallet and single crystals per pass per mg per mA	**121**
Table 6.1	Milling parameters for preparation of lithium niobate nanoparticles	**126**

Chapter 1

Introduction and Overview

1.1 Historical background

Crystals are the back bone of present scientific and technological development. Single crystals have long-range ordered periodic structure. In polycrystalline materials, several grains as well as grain boundaries are present, which are the limiting factors to their use in devices. Since crystals of high quality of different materials are required for various research and technological applications, therefore several scientific groups throughout the world are working on the research and development of crystal growth technology.

1.2 Growth of single crystal

1.2.1 The thermodynamics of crystal growth

Crystal growth is actually change of phase where molecules of the material lose their randomness gradually and arrange in a long-range periodic order in the form of crystal [1]. The thermodynamic equilibrium between solid and liquid phases occur when the free energy of the two phases are equal i.e. $G_L=G_S$. The free energy of a system is related to the internal energy and the entropy of the system by the Gibbs equation G=H-TS [2], where H is the enthalpy, S is the entropy and T is the temperature. The creation of a crystal can be thought as slow change to solid phase from liquid/melt or gas phase. The driving force for the change in phase comes due to the decrease in free energy. The free energy change during this transformation is $\Delta G = \Delta H - T\Delta S$, where $\Delta G = G_L - G_S$, $\Delta H = H_L - H_S$, $\Delta S = S_L - S_S$. At equilibrium $\Delta G=0$, hence ΔH becomes $= T_e\Delta S$, where T_e is equilibrium temperature. Now $\Delta G = T_e\Delta S - T\Delta S = (T_e - T)\Delta S = \Delta T\Delta S$ and also $\Delta G = \Delta T\ \Delta H/T_e$, where $\Delta T = (T_e - T)$. Hence ΔG become positive when $T_e > T$ and it depends on the latent heat of transition. This representation is useful for melt growth. For solution growth one may depend on concentrations instead of super cooling. In case of solution growth $\Delta G = RT \ln (C/C_0)$, where C/C_0 is the supersaturation ratio. Above two equations describe the dependence of the free energy change on the parameters like super cooling and supersaturation which are the driving force for crystallization.

1.2.2 Nucleation

Nucleation process is the aggregation of atom or molecules to form a cluster called nucleus of the atoms/molecules having same composition as the bulk crystal. It is the initiation of phase change in a small region. In general there are two types of nucleation, primary nucleation and secondary nucleation. Primary nucleation does not contain crystalline material but secondary nucleation is induced by seed crystal. There are two types of primary nucleation, homogeneous nucleation and heterogeneous nucleation. Homogeneous nucleation occurs spontaneously and heterogeneous nucleation occurs due to presence of foreign particles.

A theory of nucleus formation from group of atom was given by Volmer and Weber [3]. The probability that a stable nucleus form, which depends on change in free energy. If the free energy change between the solid and liquid is ΔG_V, the free energy of the system decreases by this amount per unit volume of the developed solid. Free energy of the system increases by σ (inter facial energy) per unit increase in surface area. Hence change in free energy during formation of spherical nucleus of radius r is given by $\Delta G = 4\pi r^2\sigma - 4/3\ \pi r^3\ \Delta G_V$. A graphical representation of this equation is given in figure 1.1.

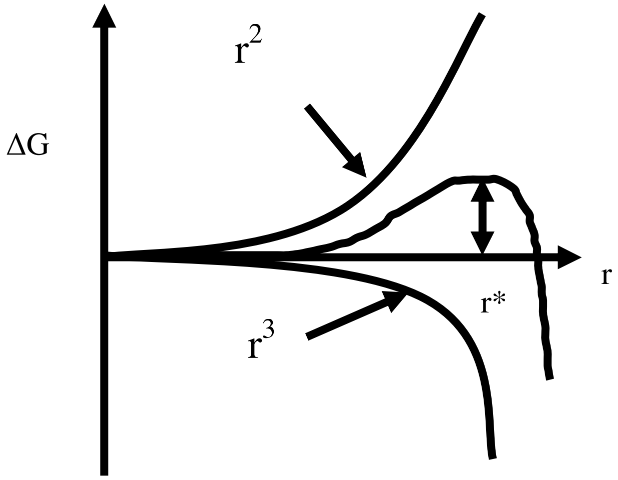

Fig. 1.1 Free energy change of nucleus as a function of radius

The surface energy term increases with r^2 and the volume energy term decreases with r^3. The net free energy change increases with the increase in size, attains a maximum and then decreases for the further increase in the size of the nucleus. The size of the nucleus where maximum free energy change occurs is called critical nucleus. On the other hand if nucleus size is less than critical value it will dissolve into the mother system. The minimum size of a stable, critically sized nucleus is obtained by differentiating the equation $\Delta G = 4\pi r^2\sigma - 4/3\ \pi r^3\ \Delta G_V$ with respect to r and equating it to zero. This gives $r^* = 2\sigma/\Delta G_V$. It may be noted that the value of r* decreases with ΔG_V, i.e. with super saturation or super cooling. The free energy change ΔG due to the formation of the critical nucleus can be calculated by substituting r*. After replacing value of r* in above equation we get $\Delta G^* = 16\pi\sigma^3/3\Delta G_V^2$. This value is less for heterogeneous nucleation than for homogeneous nucleation.

1.2.3 Crystal growth theories

Crystal growth is a process of diffusion and integration. The solute molecules or ions reach the growing surface of the crystal by diffusion through the liquid medium, where they get adsorbed and arranged in a regular space lattice [4]. For understanding the mechanism and the kinetics of growth, several theories have been developed; these are surface energy theory, diffusion theory, and etc. which have been extensively described by a number of authors [5-6].

A. Surface energy theory

The surface energy theories are explained by Gibbs. The surface energy theory tells us that shape of the growing crystal will be that which has a minimum surface free energy [7]. Although Gibbs was aware of the limitation of this theory, P. Curie [8] found it useful for a general theory of crystal growth, and finally Wulff [9] showed that the growth rates of growing crystal faces are proportional to their corresponding surface energies. Bravais [10] suggested that the velocities of the growth of the different faces of a crystal would depend on the linear density. Soehnke [11] proposed that the faces which have the greatest linear densities have minimum surface energy. These faces have minimum velocities of growth. Berthoud [12] and Valeton disputed the surface energy theory on the basis of supersaturation. According to surface energy theory when supersaturation increases, the growth becomes rapid in all directions. Consequently, the crystal habit should come in a spherical shape. But experimentally it has been observed that when the supersaturation is high, well defined faces are developed.

B. Diffusion theory

The diffusion theories, proposed by Noyes and Whimey [13] and by Nernst [14] are based on the following assumptions.

(a) There is a gradient of concentration near growing surface.

(b) The growth phenomena is a reverse process of dissolution.

According to them, the amount of solute molecules that will deposit on the surface of growing crystal can be written as

$$dm/dt = (D/\delta) \quad A\,(C-C_0),$$

where dm is the mass of the solute deposited over the crystal surface of area A during time dt, D is the diffusion coefficient of the solute, C is the actual concentration, C_0 is the equilibrium concentration of the solute and δ is the thickness of the stagnant layer adjacent to the crystal surface.

C. Surface nucleation model theory

The basis of surface nucleation model is the function of surface inhomogeneities on the growth process. A perfect single crystal has surface covered by steps. There are three types of sites; terrace, ledge and kink sites. This model developed by Kossel [15], Volmer [4] and Stranski [16] suggested that crystal growth is a discontinuous process taking place by the adsorption of matter layer by layer on the crystal surface. According to this theory the growth units coming to the crystal surface do not go immediately into the lattice, but become adsorbed and then they migrate over the surface. The possible lattice sites for the attachment of atoms on crystal surface are illustrated in figure 1.2.

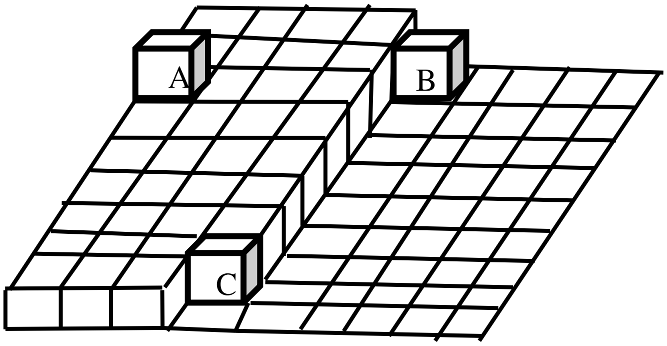

Fig. 1.2 Possible lattice site for attachment of adsorbed atom (A- Terrace site, B-Ledge site, C- Kink site)

An atom coming to the kink site is attracted by three nearest neighbors. For ledge site nearest neighbor is two and for terrace site nearest neighbor is one. Therefore the binding energy become maximum between the atom and the existing crystal surface at a kink site. Hence the atom over the crystal surface goes towards a step and moves along it to a kink site and gets attached. This step wise stacking will continue until the whole layer is completed.

D. Screw dislocation theory

This theory describes a spiral growth on screw dislocations of the crystal surface. It is known as BCF theory [17]. Completely smooth face never appears under conditions of spiral growth so surface nucleation is not essential and the crystal grows as if the surface were covered with kinks. Frank [18] proposed that dislocations having a screw component can act as a continuous source of steps on the surface of the crystal which eliminates the need for surface nucleation. A screw dislocation coming out at a point on the crystal surface produces a step on the surface. This mechanism is explained in figure 1.3. Under a given condition of super saturation these steps wind themselves up into a spiral, centered on the dislocation. This theory assumes the existence of dislocations in the crystal in order to enhance the growth of a surface.

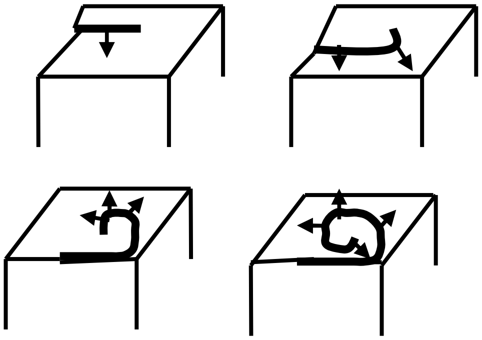

Fig. 1.3 Development of spiral during crystal growth

1.2.4 Crystal growth techniques

Crystal growth is a change of state in controlled manner. This transition may occur from the solid, liquid or vapor state. The crystal growth methods can generally be classified into four main categories [19-20] according to the involved phase transition.

A. Solid growth (solid to solid)

B. Vapor growth (vapor to solid)

C. Melt growth (liquid to solid)

D. Solution growth (liquid to solid)

A. Growth from solid

In solid growth technique, single crystals are developed from poly crystalline mass. This can be achieved by straining the material and subsequent annealing. Large crystals of several materials, especially metals have been grown by this method [21]. The main advantage of this method is growth occur at relatively low temperature without the presence of additional component.

B. Growth from vapor

Vapor growth techniques are applicable for material which does not have suitable solvent and sublime before melting at normal pressure. Vapor growth methods are used to produce bulk crystals and to prepare thin layers on crystals with a high degree of purity. Growth from vapor phase may generally be subdivided in to

1) Physical vapor transport
2) Chemical vapor transport.

Physical vapor transport (PVT)

In PVT technique the crystal is grown from its own vapors and here no extraneous compound form. There are two types of techniques used in physical vapor transport process, sublimation-condensation and sputtering. In first method sublimation of the charge occurs at the high temperature end of the furnace and the condensation occurs at the colder end [22]. Sputtering techniques are used for substance having low vapor-pressure. This method is used to prepare thin films. The main advantage of this technique is that film growth can be possible at lower temperature.

Chemical vapor transport

In chemical vapor transport technique chemical reaction occurs between the source material and a transporting agent. Initially the parent material to be crystallized is converted into gaseous product. It is then diffuses to the colder end or it transported by a carrier gas. At the cold end reverse reaction occurs. The gaseous product decomposes to deposit the parent material and the remaining transporting agent which diffuses to the hotter end and repeats the reaction with the charge. By chemical vapor deposition thin layer is produced [23-24].

Epitaxial layer of silicon and germanium are grown by this method.

C. Growth from melt

Melt growth is the method of crystallization by melting and re-solidification. The melt means a liquid very close to its solidification point. This growth method is the fastest of all crystal growth methods. This method is widely used to grow big size single crystals of congruently melting materials. Here the material to be grown is first melted by suitable technique and then it is cooled for crystallization. The main techniques of melt growth are:

1. Czochralski technique
2. Bridgman technique
3. Verneuil technique
4. Kyropoulos technique
5. Zone- melting technique.

In the present context, we will mainly concentrate only on the Czochralski technique.

1. Czochralski technique

This method was invented by Jan Czochralski in 1916 [25]. Initially this technique was used to measure the crystallization rate of metals. But at present it is the most popular and commercially preferred crystal growth techniques. In this process the congruently melting material is melted in a crucible by means of resistance or induction heating. After that a seed-crystal of same material is slowly made to touch the melt surface. In controlled super-cooling conditions, the material starts to deposit on the seed-crystal. Pulling is employed along with rotation. The rotation and thermal gradients in the melt, as well as above the melt, play crucial roles in the quality control. In Cz growth rotation of the seed helps to give the crystal a desire circular cross-section. Rotation also helps to achieve uniform distribution of dopants. The selection of parameters for CZ growth depends upon different factors. These are the thermal conductivity of both solid and liquid phases, anisotropy in thermal expansion, melt viscosity and its chemical properties, difference in solubility of dopant in liquid and solid phases, melt microstructure etc.

Condition for Czochralski growth

a. Axial gradient of temperature dT/dX = const.

b. Radial gradient of temperature dT/dr = 0.

c. The heat of crystallization must flow from melt to the crystal and dissipated by seed rod and radiation to the ambient.

d. The material should be melted congruently without decomposition.

e. The material must not be reactive with the crucible.

Heat balance equation in Cz growth

The net heat flow through the melt-solid interface is equal to rate of generation of latent heat during crystallization. For planer interface this condition can be expressed as $K_sG_s - K_LG_L = L_v$, where K_s = Thermal conductivity of crystal, K_L= Thermal conductivity of melt, G_s = Axial temperature gradient in crystal, G_L = Axial temperature gradient in melt and L_v = Latent heat of crystallization per unit volume. Axial temperature gradient is required to provide heat loss during crystal growth process. It should have some optimum value to get crack free crystal. The value of maximum axial temperature gradient depends on radius and breaking strain of the crystal. If the breaking strain is smaller than elastic strain, then under the conditions of large axial temperature gradient the crystal cracks [26].

Growth rate for Cz growth technique

The growth rate is a function of the crystal diameter, crucible diameter and the densities in the molten and solid states. Growth rate of crystal is

$V=V_p \rho_L R^2/(\rho_L R^2 - \rho_s r^2)$, where ρ_L: density of liquid, ρ_s: density of solid, R : radius of crucible, r : radius of crystal. Material for which densities are almost equal in solid and liquid, the growth in a crucible which is having twice the crystal radius occurs at a rate which is 33% greater than the pulling speed. The upper limit for the growth rate is determined by

(i) Thermoelastic properties of the crystal,

(ii) Segregation of dopant/impurity ions at the growth interface and their diffusion to the bulk,

(iii) Ease with which defects can be generated during growth etc.

Materials which have high thermal conductivity and burger vector can be pulled at faster rates if segregation effects permits. The upper limit of pull rate depends on maximum temperature gradient that can be kept above the melt level.

Effect of crystal melt interface

The solid liquid interface phenomena are very important as the crystal growth takes place at the interface. A flat interface is required during the entire growth process. If the interface is not flat then different types of defect may be developed. These are stresses, cracks, non-homogeneous impurity concentration, core phenomena, gas bubble entrapment, etc. The shape of interface depends on rotation rate of seed, thermal symmetry of the growth chamber and the heat transfer of entire system.

Convection in Cz Growth

In Cz growth, cylindrical crucible is heated from the side wall, and therefore the fluid adjacent to the crucible wall is at a higher temperature and hence it has a lower density. At the heated vertical wall of the crucible the melt is made buoyant, rises and then turned inward radially at the melt surface. The rotating crystal acts as a centrifugal fan sucking up fluid axially. Figure 1.4 shows natural and forced convective flow in crucible.

Natural convection **Forced convection**

Fig. 1.4 Schematic representation of natural and forced convective flow in crucible

The radially outward flow due to the rotating crystal meets the radially in flowing fluid driven by the hot vertical crucible wall and a down flow occur at some radial distance which depends on the relative strength on the crystal flow and the buoyancy driven convection [27].

Origin of stress during cooling the crystal in Cz technique

With respect to external forces the existence of the crystal itself gives rise to the stress due its own mass exposed to the gravitational forces. The composition of each growth layer differ slightly by Δx_i from the average composition x. These layers may shrink at different rate during cooling and tensile and compressive strain may locally alternate in different layers due to the difference in their thermal expansion coefficients [28]. Since during crystal growth, temperature gradient is required, this gradient also generates stress inside the crystal. The crystal may also crack during post growth cooling. To get crack free crystal proper post growth cooling rate is required.

Mechanism of dislocation creation in crystal grown in Cz technique

Mechanisms by which dislocations can be introduced into a crystal during growth are:

(1) Propagation of dislocations into the growing crystal from the seed crystal;
(2) Thermal stresses
(3) Constitutional stresses
(4) Dendrite growth

When segregation occurs during crystal growth lattice misfit may occur. This lattice misfit causes stress which results in dislocation [29].

Effect of segregation coefficient in Cz grown crystal

The effective segregation coefficient (K_{eff}) is the ratio of the solute concentration in the solid to that in the bulk of the liquid from which it is grown. The interface segregation coefficient (K*) is the ratio of the concentration in the solid to that in the liquid at the solid-liquid interface. In equilibrium both these ratios become equal to the ratio (K_0) which is equal to $C_S/C_{L.}$ In Czochralski pulling a dopant can segregate significantly along the growing crystal which causes significant variations in electronic and optical properties of the grown crystal.

Effect of constitutional super cooling in Cz technique

The impurity or dopant is rejected at the solid liquid interface during crystal growth. During growth the impurity is accumulated near the interface and hence lowers the melting point in that region. Thus the effective temperature driving force $\Delta T=T^* -T$ is decreased and crystal growth rate is retarded. However the melting point of the remaining charge away from the interface remains same, so ΔT increases away from the interface. This condition is known as constitutional super cooling. In this situation the advancing face usually breaks up into finger like cell, which progress in a more or less regular bunched array. By this manner heat of crystallization is more readily dissipated and crystal growth occurs under condition of near maximum driving force. It is undesirable to occur constitutional super cooling because it produces instability in planar crystal melt interface.

Facet formation during growth

Facets are crystallographic faces which form on the solid fluid interface during crystal growth [30]. Facet formation is observed in many crystals grown by Cz technique. Faceting is observed in the melt crystal interface and along the sides of solidified crystalline material. Primary causes of faceting are anisotropy in interfacial attachment kinetics and anisotropy in surface energy. Faceting of the melt-crystal interface affects the crystal quality.

Advantages and disadvantages of Cz growth

Cz growth technique has many advantages. Growth from free surface gives stress free crystal. Crystal can be observed during the growth process. In this technique large crystal with high crystal perfection can be grown. The most disadvantage of this process is delicate start and very critical further control. Crystals which can be grown by this technique are lithium niobate, lithium tetraborate etc.

2. Bridgman technique

In Bridgman technique the material is melted in a vertical cylindrical crucible having conical point bottom. The crucible is lowered slowly from hot zone to the cold zone. The rates of going down of crucible in the furnace vary from about 1–30 mm/hr. Crystallization starts at the bottom of the crucible. This technique is not suitable for materials, which decompose before melting [31]. This technique is best suited for materials with low melting point.

Advantages and disadvantages of Bridgman technique:

The main advantages are; shape of the crystal is defined by the container, no radial temperature gradient is required, low thermal stresses result in low level of stress-induced dislocations, crystals may be grown in sealed ampules. The main disadvantages are; confined growth, difficult to observe growth process, changes in natural convection as the melt is depleted and delicate crucible and seed preparation, sealing, etc.

3. Verneuil technique

In this technique a fine powder of parent material is allowed to fall through the oxy-hydrogen flame. Powder melts during passing through the flame and a liquid film is deposited on the top of the seed crystal. This solidifies gradually as the seed crystal is lowered slowly. Constant growth rate and diameter is maintained by balancing the rate of charge feed and rate of lowering the seed. This technique is applied to grow variety of high melting oxide crystal. Here no crucible is required to hold the melt and therefore contamination problem is avoided. As far as crystal perfection is concerned for some specific application (such as optical devices) the flame fusion technique is not suitable. This technique is widely used for the growth of synthetic gems and variety of high melting oxides.

4. Kyropoulos technique

In this technique the crystal is grown in a larger diameter. Here seed is brought into contact with the melt like Cz technique. In this technique seed crystal is not raised during the growth and crystal is allowed to grow by decreasing the temperature of the melt. By this technique alkali halide crystals are grown to make optical components.

5. Zone melting technique

In this technique the parent material is taken in the form of sintered rod and the seed is attached to one end. By careful control of temperature a small molten zone is maintained by surface tension between the seed and the feed. The zone is moved slowly towards the feed. Single crystal is obtained over the seed. This technique is applied for materials having large surface tension. The main advantages of this technique are simplicity of the process, growth of extreme high purity crystal and crystal with low defect density.

D. Growth from solution

Crystal growth by precipitation from aqueous solution is the most simple and oldest technique. In this process, a saturated solution of the parent material in a suitable solvent is used. Crystallization takes place from the solution as the solution becomes critically supersaturated. The supersaturation can be achieved either by lowering the temperature of the solution or by slow evaporation. There are many materials which do not melt congruently. Crystal cannot be grown from this material by melt growth technique. In some cases the crystallized material undergoes a phase transition during post-growth cooling down to room temperature. In these types of situation crystals are grown from solution growth technique. The advantages of this technique are low volatilisation of the compound as the growth temperature is lower than the melt growth technique. In this technique, crystal can be grown at temperatures well below its melting point and even at room temperature and therefore it becomes more applicable in many cases [25]. The slow growth rate is the main drawback of these techniques. It is possible to grow crystals from low-temperature solution as well as high temperature solution, the latter is popularly known as the flux growth technique.

1. Low temperature solution growth

The low temperature solution growth technique is very popular for growing many technologically important crystals. It is the most suitable method for material which are unstable at high temperature and phase transition occurs below melting point. This is a very slow growth process and takes weeks, months and sometimes years. Material which has good solubility in the temperature range from room temperature to 100 °C at atmospheric pressure can be grown by this method. This method has many advantages. As growth is carried out at room temperature, structural imperfection in this method will be less. Single crystals of KH_2PO_4, KD_2PO_4, Triglycine sulphate etc. are grown by this method. In the low temperature solution growth method crystal is grown from supersaturated solution i.e., it contains more solute than it can be in equilibrium with the solid.

2. High temperature solution growth

In this method solution is formed at high temperature. The main aim of this method is to reduce the growth temperature. Flux selection is also a critical issue. Flux should have moderate solubility for the material to be grown, appreciable solubility change with temperature, low melting point, low volatility at high temperatures, low toxicity, low viscosity, low reactivity with the crucible, and easy availability at low cost [32]. There are many advantages of crystal growth from high temperature solution. Here grown crystal is not exposed to a high temperature gradient like Cz method and the crystal can be grown in an unconstrained fashion (unlike in the Bridgman method); hence the crystals are free from mechanical or thermal constraints. Crystal grown by this method will be better in quality. Crystals will have lesser point defects, dislocations densities and low angle grain boundaries compared to crystals grown from direct melt. There are some disadvantages also. Heating material may be attacked by the corrosive nature of the fluxes. Here crystal growth rate is very slow. Solvent may be incorporated into the crystal and dopant distribution may not be uniform throughout the crystal.

1.3 Nanoparticles and preparation techniques

1.3.1 Definition of nanoparticles

Nanoparticles connect between bulk materials and atomic or molecular structures. A particle having one or more dimensions of the order of 100 nm or less is generally called nanoparticle. A bulk material has constant physical properties independent of its size, but at the nano-scale, size-dependent properties are often observed.

Nanoparticles have a very high surface area to volume ratio, which leads to tremendous changes in properties of the material with respect to bulk. As the surface area increases, the number of atom residing on the surface will be increased. The material will be more reactive because of the increase of the surface energy. As the large percentage of the atom lie on or near the surface of the nanoparticle, the electrical, optical, mechanical and thermal properties will be different from that of the bulk.

1.3.2 Preparation techniques

Large numbers of techniques are available to prepare different types of nanomaterials. Synthesis methods for nanoparticles are divided into two categories, top-down and bottom-up. In first method massive solid particle breaks in to smaller part. This is done by different technique such as milling, chemical methods, and volatilisation of a solid followed by condensation of the volatilized components. In bottom-up method, nanoparticles preparation involves condensation of atoms or molecular entities in a gas phase or in solution. The latter approach is far more popular in the synthesis of nanoparticles. In general, preparation of nanoparticles is divided into two categories, physical method and chemical method.

A. Physical methods

In the case of physical methods, most of the synthesizing techniques are involved in the sense of mechanical, evaporation etc. In these processes one can go through only physical changes such as change in state, change in physical properties etc. But there is no possibility of chemical reactions to obtain the nanoparticles.

Physical methods are again sub divided into several methods. These are:

1. High energy ball milling
2. Melt quenching
3. Physical vapor deposition
4. Pulsed laser deposition
5. Sputtering

B. Chemical method

Chemical methods are considered under the basic principle of chemical equations which depends on the chemicals and its proportions such as chemical concentration, reactivity, time, temperature, pH, etc. The chemical methods have some advantages over other methods such as:

- Simple techniques
- Less cost and instrumentation compared to many physical methods
- Reaction occurs at low temperature
- During synthesis process, doping of foreign atoms or molecules is possible
- Large quantities of materials can be synthesized

- ➢ Different kind of shapes and dimensions are possible
- ➢ Materials are obtained in the form of liquid but can be converted into powder or thin films
- ➢ Self assembly or regularized structure is possible

Chemical methods are again sub divided into several methods. These are:

1. Sol gel
2. CVD
3. L-B film

In the present work, high ball milling and melt quenching methods were used; the brief description of the techniques is described here.

I. High energy ball milling

Working principle

In ball mill, material is ground into fine powder. It is very useful technique to reduce the grain size of the material. Different types of milling devices are available. Among these planetary ball mill is most important. Rotation direction of bowl and whole disc of planetary ball mill is shown in figure 1.5.

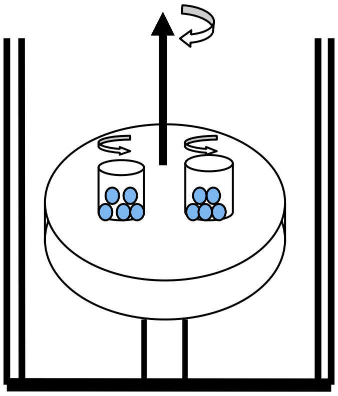

Fig. 1.5 Schematic diagram of a typical mechanism of ball milling

Planetary ball mills are very compact and smaller in dimension. The basic principle of planetary ball mill is based on rotation of planets around Sun. Bowl are arranged on a rotating support disk and a special drive mechanism helps them to rotate around their own axes.

A strong centrifugal force acts on the grinding balls and the material in the grinding bowl due to their high rpm. The grinding bowl and the supporting disc rotate in opposite directions. This leads to frictional effect between the grinding balls and grinding bowl. The energy created in this process is many times higher than that for traditional mills. Initially decrease of grain size occurs very fast and then it slows down after definite milling time. After reaching minimum grain size, further reduction is not possible. Initially dislocation is produced by the kinetic energy transfer. At a definite strain level annihilation of dislocation occur and they form small angle grain boundaries. There are two energy contributions in grain boundary region, surface energy and strain energy. The second term may become particularly high when dislocations are forced to move out from the inner part of small grain [33]. The smallest separation between dislocations, D_c limits the grain refinement. Dislocation becomes unstable and annealed out from the grains at some definite particle size which prevents further grain size reduction. During collision temperature of the material increases which also limits the reduction of grain size. Due to increased local temperature dislocation can easily come out from the material.

Various parameters of ball milling

There are various parameters on which particle size of the sample depends. These parameters are listed below:

- Speed of mill, relative speeds of pot rotation to disk revolution.
- Composition, size, shape and surface of pot.
- Degree of filling pot.
- Number, size(s), material (density, elasticity), and surface of milling balls.
- Weight, shape, size and composition of starting material.
- Macroscopic temperatures of pot, ball and powder.
- Microscopic temperature at collision point.
- Milling atmosphere.
- Milling time.

For reduction of particle size speed of mill and relative speeds of pot rotation to disk revolution in a planetary mill are very important parameters. Speed of mill determines the force exerted on the powder sample. Very high speed of rotation is not desirable because balls and container wall may crack. So optimization of speed is required. In ball milling to break the parent particle balls should have higher kinetic energy. As the kinetic energy of ball depends on mass and velocity, so dense materials are preferred. The hardness of the grinding bowl and grinding balls must be higher than that of the materials used for milling. This is required to prevent abrasion. Normally grinding bowls and grinding balls of the same material should be chosen. Ball to powder mass ratio is also an important parameter. Greater ball to powder mass ratio (BPMR) is required for particle size reduction as this increases the collision frequency. It is reported that filling the pot above 50% reduces the milling efficiency. During reduction of particle size fresh atomic surfaces are generated, so contamination by O_2 may occur. To remove this problem milling is generally done in inert atmosphere.

II. Melt quenching technique

It is a fast and cost effective technique. It is possible to form nanoparticles in glass. When a liquid is cooled below certain temperature, it forms either crystalline or amorphous solid (glass) [34]. Mixture of chemical is prepared by mixing chemicals taking in proper ratio and kept for solid state reaction at some temperature below the melting point. This solid state reacted powder is kept in platinum crucible and then put into furnace. The temperature of crucible is maintained above the melting temperature of that material. After melting the charge, the melt is poured on a metallic plate very fast and pressed it with another metal plate. Most of the formed glasses are annealed in a temperature range that is slightly higher than the glass transition temperature for making nanoparticles. Size of nanoparticles in this technique depends on the annealing temperature.

1.4 Photorefractive effect

The term photorefractive means light induced change of the refractive index. Initially it was considered as undesirable optical damage in non-linear electro-optic crystals, but later it was found that this optical damage can effectively be applied for holographic recording in electro-optic crystals [35-36]. Photorefractive phenomena can be observed in any material which is photo-conductive, transparent to the wavelength of interest and electro-optic.

1.4.1 Mechanism of the photorefractive effect

The photorefractive effect occurs in several stages. Figure 1.6 shows how refractive index grating is formed.

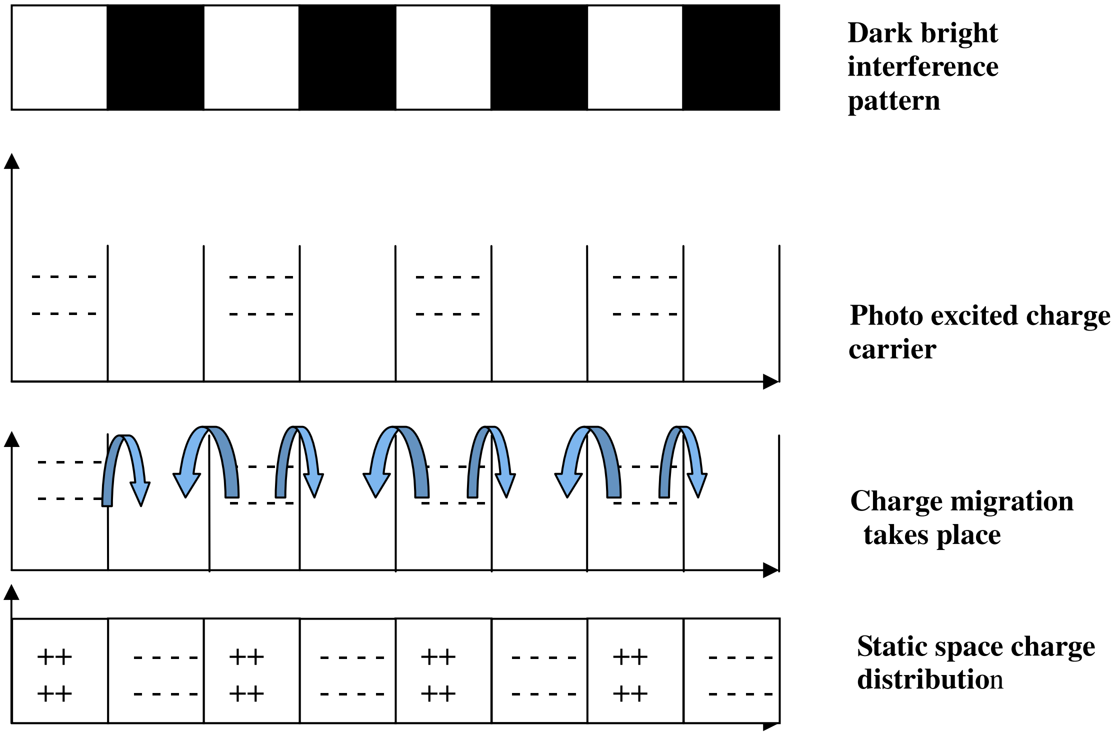

Fig. 1.6 Mechanism of formation of refractive index grating inside a PR material

- Light from two coherent sources are incident on a PR crystal and interference pattern (alternate dark and bright fringes) is formed. Out of the two light beams, one is called as signal beam and other as reference beam.
- In the bright regions, electrons are excited to the conduction band, leaving a hole in the impurity level. The impurity levels have an energy intermediate between the energies of the valance band and conduction band of the material.
- These free electrons migrate due to diffusion towards the dark regions.
- A space charge field is generated due to distribution of charge. As the electrons are trapped at trap centers they become immobile and field remain present even when illumination is stopped.
- This electric field modulates the refractive index of the material through electro-optic (Pockel's linear) effect and refractive index grating is formed (figure 1.6).

- The refractive index grating diffracts the light incident on the crystal.
- By uniform illumination of light this refractive index grating can be removed.

From the figure 1.6 it is clear that the photo refractive effect provides a way to replicate light intensity patterns into refractive index gratings, which can be applied for optical data storage.

1.4.2 Desirable properties of PR materials

The main properties of an electro-optic material for PR applications are:

- Diffraction efficiency (DE)
- Recording (or writing) and erasure time
- Dynamic range (maximum refractive index change)
- PR sensitivity
- Signal-to-noise ratio
- Sensitive to convenient laser wavelength
- Suitable dopant should be available for particular laser wavelength

Diffraction efficiency (DE)

DE (η) of a PR crystal is defined as the ratio of the intensity of light diffracted by the refractive index grating (I_{diff}) to the transmitted light intensity when there exists no grating (I_{trans}). It can be obtained by the relation [37]:

$$\eta = \frac{I_{\text{diff}}}{I_{\text{trans}}} \times 100\%$$

A good PR material should have high DE.

Recording and erasure time

The recording time τ_r is defined as the time period in which DE increases to (1-1/e) of its maximum during recording, while erasure time τ_e is defined as the time period in which DE decreases to 1/e of its maximum during erasing.

Dynamic range

The dynamic range ($M^{\#}$) of a phase storage medium is defined as the maximum possible photo-induced change of its refractive index. The dynamic range determines the number of holograms that can be recorded in a given volume. Its value is given by the relation

$$\eta_M = (M^{\#}/M)^2$$

where, M is the multiplexed page number, η_M is the DE when M^{th} page is written. The value of $M^{\#}$ can also be calculated approximately by a much simpler relation [38].

$$M^{\#} \approx \frac{\tau_e \sqrt{\eta_{max}}}{\tau_r}$$

where, η_{max} is the maximum DE. A good PR material should have large dynamic range.

PR sensitivity

The PR sensitivity (*S*) is defined as the light energy density required to achieve a given holographic DE.

Its value is given by the relation

$$S = \frac{1}{IL}\frac{d\sqrt{\eta}}{dt}$$

where, *I* is light intensity and *L* is the crystal thickness. A good PR material should have higher sensitivity.

Signal-to-noise ratio

In optical holography, noise is a term for non-image-forming light which is diffracted or scattered in the same general direction as the reconstructed image. High signal-to-noise ratio for holographic applications is preferred.

Sensitive to convenient laser wavelength

The electro-optic material considered for recording should be photosensitive at a convenient laser wavelength and should be transparent at that wave length.

1.4.3 Materials perspective

Photorefractive (PR) crystals are excellent materials for recording volume phase holograms in real-time. These materials have excellent resolution, efficiency, storage capacity, sensitivity and reversibility. Number of holograms can be recorded on a single crystal by angular multiplexing. The application of these materials for hologram recording was first considered by Chen, 1968 [35], who suggested that optical damage effect in these crystals could be exploited to record a thick hologram. The photorefractive effect has been detected in number of crystals; the major ones used for holographic application are $LiNbO_3$, $LiTaO_3$, $BaTiO_3$, $Bi_{12}SiO_{20}$, and $Bi_{12}GeO_{20}$.

1.5 Thermoluminescence (TL)

Thermoluminescence (TL) is the thermally stimulated emission of light from the irradiated material. For production of TL, the material must be an insulator or a semiconductor. The material must be irradiated with some ionizing radiation. An irradiated thermoluminescence material released energy in the form of visible light when the material is heated.

1.5.1 Basic principle

In a semiconductor or insulator most of the electrons reside in the valence band. The next band where electron can be placed is conduction band. The energy difference between these two bands is E_g. Due to structural defect and impurities within the lattice, electrons posses energies which are forbidden in the perfect crystal [39].

In a simple TL model two levels are assumed, one situated below the bottom of the conduction band and the other situated above the top of the valence band (figure 1.7). The highest trap level (T) is situated above the Fermi level. This is electron trap. The other level (R) situated below the Fermi level. This is a hole trap and acts as a recombination center. When the material absorbs radiation having energy greater than E_g ionization occur and produce free electrons in the conduction band and free holes in the valence band. The free charge carriers recombine with each other or become trapped. In semiconductors and insulators a certain percentage of the charge carriers are trapped, the electrons at T and the holes at *R* (transition *b*). The probability of releasing the electron from trap center is described by Arrhenius equation $p = s \exp(-E/kT)$, where *p* is the probability per unit time. The term *s* is called the frequency factor or attempt-to-escape factor. The value of s in the order of the lattice vibration frequency, namely 10^{12}-10^{14} s^{-1}. E is called the trap depth or activation energy, the energy required to come out from the trap into the conduction band. The other symbols have their usual meaning, *k*=Boltzmann's constant (=8.617×10^{-5} eV/K), and T the absolute temperature. If the trap depth $E >> kT_0$, with T_0 the temperature at irradiation, then any electron that becomes trapped will remain trap for a long time. When temperature of the material is increased electrons start releasing from the trap center and enter into the conduction band. The charge carrier migrates through the conduction band of the crystal and finally they recombine at recombination center R. In the simple model this recombination center is a luminescent center where the recombination of the electron and hole leaves the center in one of the higher excited states. Return to the ground state from the excited state gives the emission of light quanta i.e. Thermoluminescence.

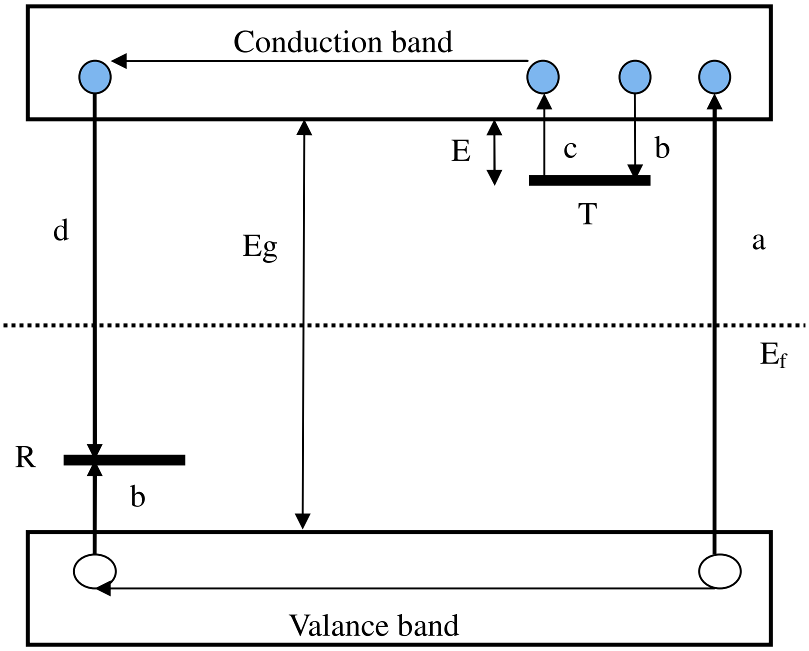

Fig. 1.7 Energy band model showing the electronic transitions in a TL material according to a simple two-level model: (a) generation of electrons and holes; (b) electron and hole trapping; (c) electron release due to thermal stimulation; (d) recombination. Solid circles are electrons, open circles are holes. Level T is a electron trap, level *R* is a recombination centre, E_f is Fermi level, E_g is the energy band gap.

1.5.2 Important properties of a TL dosimeter

Sensitivity

The sensitivity of particular TLD material is defined as TL intensity integrated over an certain temperature region per unit mass per unit absorbed dose. TL sensitivity should be high for a good dosimeter [40].

Dose response

Linear dose response is another critical characteristic. This property shows that the response displayed by the material is directly proportional to the absorbed dose of radiation. In most materials, the linear interval is limited by supralinearity and saturation of the TL intensity at large doses. The useful range is determined by the linear dose dependence. Both supralinearity and sublinear growth approaching saturation creates problem of over or under estimation, respectively. It is desirable for a good dosimeter that supralinearity should start at higher dose. Threshold dose is measured to determine the minimum dose that can be detected by the dosimeter. An additional important property required for radiation detector is that its response should be independent of dose rate.

Glow curve

The glow curve is a plot generated by software connected to TL measurement systems. In this graph the thermoluminescence intensity versus temperature is plotted. The peaks observed on this curve correspond to the ionization of traps at various energy levels. The intensity axis of the plot gives an idea about the relative populations of electrons in different traps [41]. The glow curves are particularly important since they are the main indicators of whether a material can be used for TL dosimetry purposes or not. Generally it is desired that the glow curve should have simple and single peak at around 200 °C. The peaks observed at low temperatures in the proximity of 100 °C fade away quickly hence they do not yield any information about the radiation content.

Fading

Fading is the unintentional loss of TL signal with time. For a good TL material fading should be very small. Thus, fading can be regarded as a quality indicator for the dosimeter. If the trap depth E of the material is very small then much fading will occur during irradiation and after irradiation.

Effective atomic number

It is desirable that the dosimeter should have same atomic composition as that of the human tissue. This concept can be evaluated by the parameter of effective atomic number (Z_{eff}) which should be as close as possible to that of human tissue (7.42.). Tissue equivalence is rare among the dosimeters and the dosimeter which satisfies this requirement the best is lithium tetraborate. Tissue equivalence becomes more important in case the radiation energy lies in the region between 20 and 100 keV. At these energies the photoelectric interaction is predominant and dependent on the third power of the atomic number, so in that region an over response of TL intensity occur for materials having a high atomic number [42].

Emission wavelength

The TL emission spectrum of a material should overlap as much as possible with the absorption spectrum of the PMT. Most PMTs peak absorption efficiency are in the 400 – 450 nm range.

Dependence of TL response on the energy of the incident radiation

The intensity of thermoluminescence emitted from a material is proportional to the amount of energy initially absorbed by that material. It is thus most important to know the materials absorption coefficient with radiation energy. For photon energy < 15 keV, the photoelectric effect dominates, whereas for $15keV<E<10MeV$, Compton scattering dominates in low Z material. For high Z specimen the photoelectric effect remain dominant up to 100keV. For dosimetry, it is obliviously desirable to have a detector which exhibits a constant response over a wide range of energies; therefore low Z materials are preferred. Again tissue equivalent dosimeters are desirable for measurement of the dose delivered to the body tissue. Lithium tetraborate is one such phosphor with $Z_{eff} = 7.4$, equal to that of tissue [43].

1.5.3 Materials perspective

TLD is used to determine the amount of radiation absorbed by the person due to working environment or due to medical treatment. It is very useful for people who are working in nuclear power plant or any radiation environment. In personnel dosimetry, a card containing TLD material is provided to the worker and the amount of absorbed dose is measured periodically. Thermoluminescence dosimeters are also used in clinical dosimetry because of their various advantages. TL dosimeter has wide useful dose range, small physical size, no need for high voltage cable and tissue equivalence for most radiation type. In thermoluminescence dosimetry (TLD) TL output is directly proportional to the radiation dose received by the phosphor and hence the absorbed dose is estimated. Absorbed dose is defined as an amount of energy absorbed per unit mass of an irradiated material. Clinical dosimetry is performed for measuring the absorbed doses to the patient either during therapy or diagnosis.

There are more than 2000 TL materials available, out of them only 8 are appropriate for measuring radiation dose. Four of them have low atomic number (Z) and are characterized as tissue equivalent materials. These are lithium fluoride (LiF), lithium tetraborate ($Li_2B_4O_7$), beryllium oxide (BeO) and magnesium borate (MgB_4O_7). They are used for medical application as well as for personnel monitoring for industrial applications. The other four materials over-respond due to their higher Z. These materials are characterized as non-tissue equivalent materials. These materials are calcium sulphate ($CaSO_4$), calcium fluoride (CaF_2), aluminum oxide (Al_2O_3) and magnesium orthosilicate (Mg_2SiO_4) and are used for environmental monitoring. The main characteristics of these basic TL dosimeters are the wide useful range, sensitivity to small doses, and limited fading [44]. Spectra of commercial luminescent dosimeters exhibit an emission maximum at 380–480 nm, which corresponds to the spectral range of common photo multipliers.

LiF-based dosimeter satisfies all required properties for commercial dosimeters except it fails to provide a simple TL glow curve. For example, the TL curve of LiF: Ti, Mg contains at least seven peaks. Generally, the 5th peak (T_m = 210 °C) is used for dose measurements. A large number of peaks in glow curve make it more complicated. The maximum emission wavelength of LiF is 400 nm.

Lithium tetraborate doped with Mn has linear response up to 300 rad and supralinear up to 30 kgray. It is light sensitive material. This creates a background equivalent to 15 mrad. The wavelength of light emitted from this TLD is 600nm. The sensitivity of gamma rays for Cu doped $Li_2B_4O_7$ is many times more than that of Mn: $Li_2B_4O_7$. This higher TL sensitivity Cu doped lithium tetraborate is due to the favorable spectral location of TL emission at 368 nm.

BeO is a good tissue-equivalent material. When we measure TL intensity on a TL reader having standard PMT, the apparent sensitivity of BeO is low (about seven times less than that of LiF). If we read the TLD with a photo multiplier having quartz window, a better sensitivity results which equals that of LiF. This is because quartz window also allow UV radiation to pass through. BeO containing sodium is very sensitive and allows the measurement of doses down to 1mrad. The dose response curve is linear up to 50 rad. The following supralinear range extends up to doses of 5×10^5 rad after which saturation occurs.

Aluminium oxide (Al_20_3) is also interesting material because it is available at low cost. It has strong emission in the 650 nm region which is difficult to distinguish from black body radiation and a weaker emission between 390 and 550 nm. It is the latter emission which is more interesting because it can be detected with an ordinary commercial TL reader. Al_20_3 has no linear dose characteristic for either glow peak. The lowest detectable dose is about 100 mrad as long as the readings are performed with N_2 flushing. Saturation occurs at 10^6rad.

$CaSO_4$: Dy and $CaSO_4$: Tm is equally more sensitive to photon radiation compared to LiF. The lower detection limit is about 0.1 mrad. The dose response of $CaSO_4$: Dy is linear up to doses of $3x10^3$rad and saturation occurs at 10^5 rad.

CaF_2 is not tissue equivalent (Zeff = 16.57). It is a factor of 15 times more sensitive to 30 keV photon radiation than to the photon radiation from ^{60}Co. CaF_2 has two important advantages over LiF in certain applications. It is considerably more sensitive, the minimum detectable dose is about 10 times less than LiF and it has a larger linear dose response range.

Various studies were done to use commercial TL dosimeters for detection of fast neutron fluxes, but it was less successful [45]. The TL yield of LiF:Ti, Mg; LiF:Mg,Cu,P and Al_2O_3:C proved to be very low. As neutrons have no charge, they are detected through secondary particle produced during neutron irradiation. For thermal neutron in order to obtain high yield for such particles, isotope with high reaction cross-section are incorporated into the detector. LiF and $Li_2B_4O_7$ respond to slow neutrons via reactions with ^{6}Li and ^{10}B. The reactions are

$$^6Li_3 + {}^1n_0 \longrightarrow {}^4He_2\,(\alpha) + {}^3H_1 \quad \text{and} \quad {}^{10}B_5 + {}^1n_0 \longrightarrow {}^4He_2\,(\alpha) + {}^7Li_3.$$

LiF(Mg,Ti) dosimeter have three different varieties. TLD-100, TLD-600, TLD-700. The material TLD-100 is a LiF (Mg,Ti) that contains natural lithium with both ^{6}Li (7.5%) and ^{7}Li (92.5%) not especially useful for neutron dosimetry. TLD-600 is ^{6}Li enriched phosphor [^{6}LiF(Mg, Ti)]. Here ^{6}Li undergoes an (n, α) reaction, and the alpha particle and the tritium that are produced, deposit their kinetic energies in the TLD element. TLD-700 includes a neutron insensitive element. This dosimeter is used to measure the gamma dose. This phosphor is quite insensitive to thermal neutrons and if it is paired with a similar geometry and mass of ^{6}LiF(Mg,Ti) element, the net neutron response is obtained by subtracting the gamma response of the ^{7}Li element from the gamma plus neutron response of the ^{6}Li element. The TLD-1000, 6000, and 7000 are common designations for alternative LiF phosphors containing a different dopant mixture from the LiF noted above, namely LiF (Mg,Cu,P), which has a considerably higher sensitivity than the LiF (Mg,Ti); The 1000, 6000, and 7000 designations have similar meanings to the 100, 600, and 700 descriptions. Other commonly denoted phosphors are TLD-200, 300, 400 and 900 CaF_2 (Dy), CaF_2(Tm),

CaF_2(Mn), $CaSO_4$(Dy) respectively, all relatively high sensitivity phosphors but not used for typical neutron dosimetry. Response of thermal neutons for TLD s is shown in Table 1.1.

Table 1.1 Values for the response of a number of TL materials to a fluence of 10^{10} thermal neutrons/ cm^2 in terms of an equivalent exposure to ^{60}Co gamma rays.

Material	**Response (10^{10}/ cm^2)/ R of ^{60}Co γ rays**
LiF (TLD-100)	350
LiF(TLD-600)	1930
LiF(TLD-700)	1.5
LTB:Mn(TLD-800)	310
CaF_2:Mn	0.6
$CaSO_4$:Dy	0.5
BeO	0.3

It is seen from the above table that the most useful material for performing gamma measurements in a mixed neutron-gamma field is BeO due to its low response. Various properties of different TLD material shown in table 1.2. Here energy dependence is also given. Which shows there response at 30 keV (where the maximum over response occurs) relative to that at 1173 and 1332 keV (i.e. ^{60}Co). The ideal relative response is 1.0 which indicates that the material is energy independent.

Table 1.2 Various properties of different TLD material

Phosphor	**Glow Peak in °C**	**Emission (nm)**	**Z_{eff}**	**Energy response 30keV/ ^{60}Co**	**Sensitivity**	**Linear range (rad)**	**Saturation level (rad)**	**Thermal fading**	**Optical fading**
LiF:Mg,Ti	210	425	8.14	1.3	1.0	$5X10^{-3}$-10^{2}	10^{5}	5-10% per year	NA
LiF:Mg,Cu,P	232	310 410	8.14	1.3	25	10^{-4} -10^{3}	>10^{4}	NA	
$Li_2B_4O_7$:Mn	210	600	7.4	0.9	0.4	0.01-300	$3X10^{6}$	5% in 60 days	sensitive
$Li_2B_4O_7$:Cu	205	368	7.4	0.8	8	0.01-10^{5}	>10^{5}	25% in 60 days	10% in 3 hr
MgB_4O_7:Dy	210	480 570	8.4	1.5	7	0.001-100	10^{3}	10% in 60 days	sensitive
$CaSO_4$:Dy	220	480 570	15.3	10-12	30	10^{-4} -$3X10^{3}$	10^{5}	7-30% in 6 month	30% in 5 hr
$CaSO_4$:Tm	220	450	15.3	10-12	60	10^{-5} -$3X10^{3}$	10^{4}	7-30% in 6 month	30% in 5 hr
CaF_2 (natural)	260	380	16.3	13-15	20-50	10^{-3} -$5X10^{3}$	10^{4}	NA	Sensitive
CaF_2:Dy	200 240	480 575	16.3	13-15	16	10^{-3} -$X10^{3}$	10^{6}	25% in 4 week	Sensitive
CaF_2:Mn	300	500	16.3	13-15	10	10^{-3} -$X10^{3}$	10^{5}	7% in 24hr	Sensitive
BeO	180 to 220	330	7.13	1.4	3	10^{-2} to 50	$5X10^{5}$	7% in two month	50% in 1 hr
Al_2O_3	250	425	10.2	3.5	5	10^{-2} to 100	10^{5}	5% in one month	sensitive

References:

1. S. Toschev, Crystal Growth: An Introduction, Ed. P. Hartman, North Holland, Amsterdam, (1973).
2. J. W. Gibbs, Collected Works, Longmans Green and Co., New York, 1928.
3. M. Volmer and A. Weber, Z. Phys. Chem., 119 (1925) 227.
4. M. Volmer, Kinetic der Phasenbildung, Steinkopf, Leipsig (1939).
5. R. Ueda, J. B. Mullin,. (Eds.), Crystal Growth and Characterization, North Holland

Publishing Company, Amstardam, 1975.

6. A. W. Vere, Crystal Growth: Principles and Progress, Plenum Press, New York, 1987.
7. J. W. Gibbs, The Collected Works of J.W. Gibbs, Vol. 1: Thermodynamics, Yale Univ. Press, New Haven, 1948.
8. P. Curie, Bull. Soc. Fr. Min. Crist. 8 (1885) 145.
9. G. Wulff, Z. Krist. 34 (1901) 449.
10. A. Bravais, and A. Etudes, Crystallographiques, Gauthier Villers, Paris,1866.
11. L. Soehncke, Entwickelung einer theories d. krystatlastrattur, Leipzing. 1879.
12. A. Berthound, J. Chem. Phys., 10 (1912) 624.
13. A. A. Noyes, and W. R. Whitney, Z. Physik. Chern., 23 (1891) 689.
14. W. Nernst, Z. Physik. Chem., 67 (1909) 470.
15. W. Kossel, Nachr. Ges. Wiss. Goettingen Math. Phys., K1 11A (1927) 135.
16. I. N. Stranski , Z. Phys. Chem., 136 (1928) 259.
17. W. K. Burton, N. Cabrera, F. C. Frank, Phil. Trans. Roy. Soc., A 243 (1951) 299.
18. F. C. Frank, Discussions Faraday Soc., 5 (1949) 48.
19. H. E. Buckley, Crystal Growth, John Wiley and Sons, Inc. NY, 1951.
20. J. C. Brice, Crystal Growth Process, John Wiley and Sons, New York, 1986.
21. C. S. Barrat, and T. B. Massalski, Structure of Metals, McGraw-Hills, New York, 3rd edn., 1966.
22. M. M. Faktor, I. Garrett, Growth of Crystals from the Vapour, Chapman and Hall, London, 1974.
23. E. Kaldis, J. Cryst. Growth, 17 (1972) 3.
24. A. K. Kulkarni, Bull. Mater. Sci., 17 (1994) 1379.
25. J. Czochralski, Z. Phys. Chem. 92 (1918) 219.
26. J. C. Brice, J. Cryst. Growth, 2 (1968) 395.
27. Donald T. J. Hurle, Crystal pulling from the melt, Springer-Verlag Berlin Heidelberg 1993.
28. J. C. Brice, J. Cryst. Growth, 7 (1970) 9.
29. Hunt, M. D. Spitlle, J.A .Smith,R.W. J. Cryst. Growth 3, 4 (1968) 656.
30. J. C. Brice, J. Cryst. Growth 6 (1970) 205.
31. P. Santhana Raghavan and P. Ramasamy, Crystal Growth Processes and Methods. KRU

publications, 2000.

32. D. Elwell and H. J. Scheel, Crystal Growth from High-temperature Solutions, Academic Press, London (1975).

33. H. Nalwa (editor), Nanoclusters and nanocrystals, Chapter 1, American Scientific Publishers, 2003.

34. S. K. Kulkarni, Nanotechnology principle and practices Chapter 1, Capital publishing company, 2007.

35. F. S. Chen, J. T. LaMacchia, and D. B. Fraser, Appl. Phys. Lett., 13 (1968) 223.

36. F. S. Chen, 1969, J. Appl. Phys., 40 (1969) 3389.

37. L. Sun, F. Guo, Q. Lv, , H. Li, W. Cai,, Y. Xu, and L. Zhao, J. Cryst. Growth, 307 (2007) 421.

38. H. Hatano, T.Yamaji, S. Tanaka, Y. Furukawa, and K.Kitamura, Jpn. J. Appl. Phys., 38(1999) 1821.

39. A. J. J. Bos, Radiat. Meas. 41 (2007) S45.

40. M. Prokic, Radiat. Prot. Dosim., vol. 33, (2002) 265.

41.K. Mahesh, P. S. Weng, and C. Furetta. Thermoluminescence In Solids And Its Applications. Nuclear Technology Publishing: Ashford, 1989.

42. C. Furetta, M. Prokic, R. Salamon, V. Prokic, and G. Kitis, Nucl. Instrum. Methods. Phys. Res. A 456 (2000) 411.

43. S. W. S. McKeever, Thermoluminescence of solids, Cambridge University Press, Cambridge 1985.

44. V. Kortov, Materials for thermoluminescent dosimetry: Current status and future trends, Radiat. Meas. 42 (2007) 576.

45. G. A. Klemic, N. Azziz, S. A. Marino, Radiat. Prot. Dosim. 65(1–4) (1996) 221.

Chapter 2

Characterization Techniques

2.1 X-ray Diffraction

2.1.1 Introduction

X-rays are electromagnetic radiation. The wave length of X-rays used in diffraction study lies in the range of 0.5 Å to 2.5 Å and which is between gamma and ultraviolet rays. X-rays are produced when an electrically charged particle of sufficient kinetic energy is rapidly decelerated. Characteristic X-ray is created due to inner electron transition.

2.1.2 Working principle

The experimental technique of XRD is based on Bragg's law of diffraction. If a beam of monochromatic X- rays incident on crystalline material, diffraction of the X-rays are observed at different angles from different crystal planes. The ray diagram given in figure 2.1 shows how X- ray diffraction occur from crystalline plane.

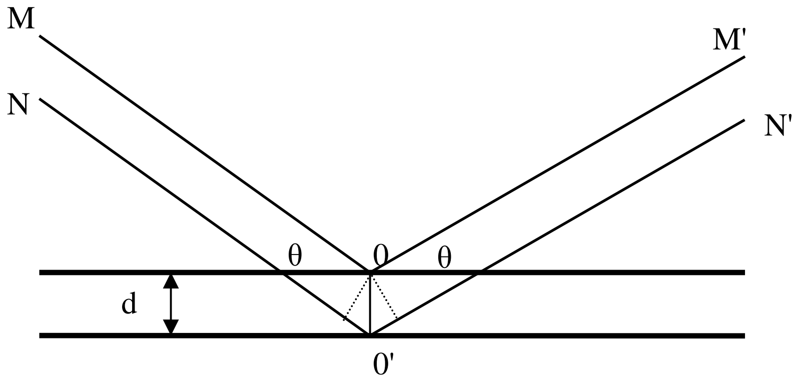

Fig. 2.1 Ray diagram of diffracted X-rays

The Bragg's condition is given by $2d \sin \theta = n \lambda$, where n is an integer and represents the order of diffraction, λ is the wavelength of the X-rays in angstrom unit, d is the inter planar spacing, θ is the diffraction angle. From the above equation we can calculate the inter planner spacing of the crystalline material. In X-ray diffraction, the incident beam falls on crystal planes at angle θ and beam diffracted at an angle 2θ. In powder XRD fine powder of sample is placed on sample holder on which a beam of monochromatic X-ray falls. After getting diffracted from crystalline plane, constructive interference occurs and peak is observed. From the XRD pattern we can identify the phase of the material. By observing peak position lattice parameter can be calculated.

2.1.3 Peak shape analysis

Peak broadening (β) comes from several sources. These are due to instrumental effect, finite crystallite size, and strain. For Lorentzian peak $\beta_{obs} = \beta_{size} + \beta_{strain} + \beta_{inst}$. Therefore $\beta_{obs} - \beta_{inst} = \beta_{size} + \beta_{strain}$. Similarly for Gaussian peak $\beta_{obs}^2 = \beta_{size}^2 + \beta_{strain}^2 + \beta_{inst}^2$. Therefore $\beta_{obs}^2 - \beta_{inst}^2 = \beta_{size}^2 + \beta_{strain}^2$. A perfect crystal extends in all directions to infinity, so we can say that no crystal is perfect due to its finite size. This deviation leads to a broadening of the diffraction peaks. However, above a particular size (100-500 nm) this type of broadening is negligible.

A. Instrumental broadening:

This type of broadening arises due to the following factors:

1. The source of radiation (X-rays) has a finite physical size.
2. The radiation is not perfectly monochromatic, it consists of a small range, $\delta\lambda$, of wavelengths around the mean, λ .
3. Axial divergence of the incident/diffracted beams.
4. Any misalignment of the diffractometer .

B. Size broadening:

In 1918 Scherrer first observed that size of crystallite is related to peak broadening. It means the width of diffraction curve increases when the thickness of crystal decreases. Scherrer derived a well known equation to relate the crystallite size to the broadening of peak, which is called the Scherrer formula. From this equation, calculation of particle size of crystalline material can be done easily. In the Scherrer equation [1], $\beta = \frac{\lambda}{L\cos\theta}$, where λ is wave length, β is the line broadening at half the maximum intensity (FWHM) in radians, and θ is the Bragg angle, L is the grain size of the ordered (crystalline) material.

C. Strain broadening:

Strain is defined as the ratio of deformation of an object to its ideal length (Δd/d). In crystals we can observe two types of strain, uniform strain and non-uniform strain. Uniform strain is that strain in which the unit cell expand or contract in an isotropic manner. This results to a change in the unit cell parameters and shift of the peaks. There is no broadening associated with this type of strain. Non-uniform strain occurs when different crystallite is strained by different amounts which lead to peak broadening. One can derive an approximate relationship relating the mean inhomogeneous strain (ξ) to the peak broadening it produces (β_ξ). This is derived by differentiating Bragg's Law.

$\lambda = 2d\sin\theta$ Or $d = \frac{\lambda}{2\sin\theta}$, Therefore, $\Delta d = \frac{\lambda}{2}\left(\frac{-1}{\sin^2\theta}\right)\cos\theta\Delta\theta$. Now strain $\xi = \frac{\Delta d}{d} = -\cot\theta\Delta\theta$, Which gives $\Delta\theta = \xi\tan\theta$. Hence $\beta_\xi = C\xi\tan\theta$ [2].

2.1.4 Application of XRD

From X-Ray diffraction we can get the following information regarding the sample [3]:

a. Phase analysis
b. Lattice parameter determination (from peak position of XRD pattern)
c. Particle size (from peak broadening)
d. Strain inside the sample

2.2 High resolution XRD

2.2.1 Introduction

High resolution X-ray diffraction is powerful nondestructive technique for structural characterization and used to evaluate crystalline perfection of single crystal. This technique is useful for direct observation of defect and gives valuable feedback for improving structural perfection of the single crystal.

2.2.2 Working principle

In high resolution XRD, divergence and spectral width of the X-ray beam is very small. Ray diagram of HRXRD instrument is shown in figure 2.2. Here X-ray passes through a set of monochromators and then incident on the sample. Such arrangement gives highly collimated and monochromatic X-ray. To measure crystalline perfection rocking curve is studied. Here ω varies and 2θ kept constant. Ray diagram for rocking curve measurement is shown in figure 2.3. Here ω is the angle between incident x-ray and sample surface, 2θ is the angle between incident X-ray and detector. In rocking curve measurement the source position as well as the detector positions are fixed, but the sample is rocked around the Bragg peak slightly. FWHM of the rocking curve is an important indicator of the material for crystalline quality.

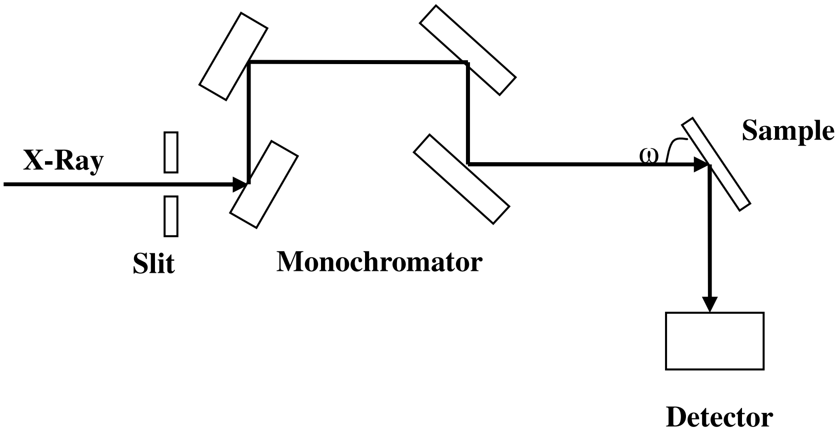

Fig. 2.2 Ray diagram of HRXRD instrument

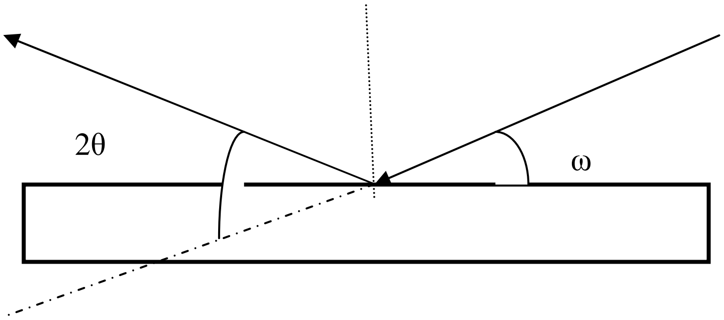

Fig. 2.3 Ray diagram for rocking curve measurement

2.2.3 Application

High resolution XRD provides information about

a) Crystal lattice misfit/ strain

b) Lattice distortion in structure

2.3 Transmission Electron Microscope

2.3.1 Introduction

Transmission electron microscope is the most efficient and important tool for materials characterization. Microscopes are generally used for magnifying things which we cannot see with naked eye. The smallest distance between two points that we can resolve with our eyes is about 0.1 to 0.2 mm. This distance is resolution or resolving power of our eyes. So any instrument that can shows us pictures which provide detail finer than 0.1 mm could be described as microscope. A major attraction to the researcher was that since electrons are smaller than atoms, it would be possible to build a microscope that could see detail well below the atomic level. Our eyes are not sensitive to electron. So an integral part of any electron microscope is a viewing screen of some form, which translate electron intensity to visible light intensity, and which we can observe or record photographically [4]. Resolution is given by, $\delta=0.61\lambda/\mu \sin \beta$, here λ is the wave length of the radiation, μ is the refractive index of the viewing medium, β is the semi angle of collection of magnifying lens. For simplicity we can approximate $\mu \sin \beta$ to unity and so the resolution is equal to about half the wave length of the light. For green light in the middle of the visible spectrum, λ is about 550 nm and so the resolution of a good light microscope is about 300nm. Now although 300 nm is small dimension to us it corresponds to about 1000 atoms diameter. Therefore different features that control the properties of the material lie well below the resolution of light microscope. So to study the material in atomic level, microscope having better resolution is required. That is a major reason why TEM are essential.

2.3.2 Sample preparation

To get information using transmitted electron in TEM, specimen must be thin. For a specimen to be transparent to electron it must be very thin to transmit sufficient electron and transmitted electron reach to the photographic film and give us an interpretable image. Generally this requirement is dependent on electron energy and average atomic number (z) of the specimen.

2.3.3 Working principle

The schematic diagram of TEM is shown in figure 2.4.

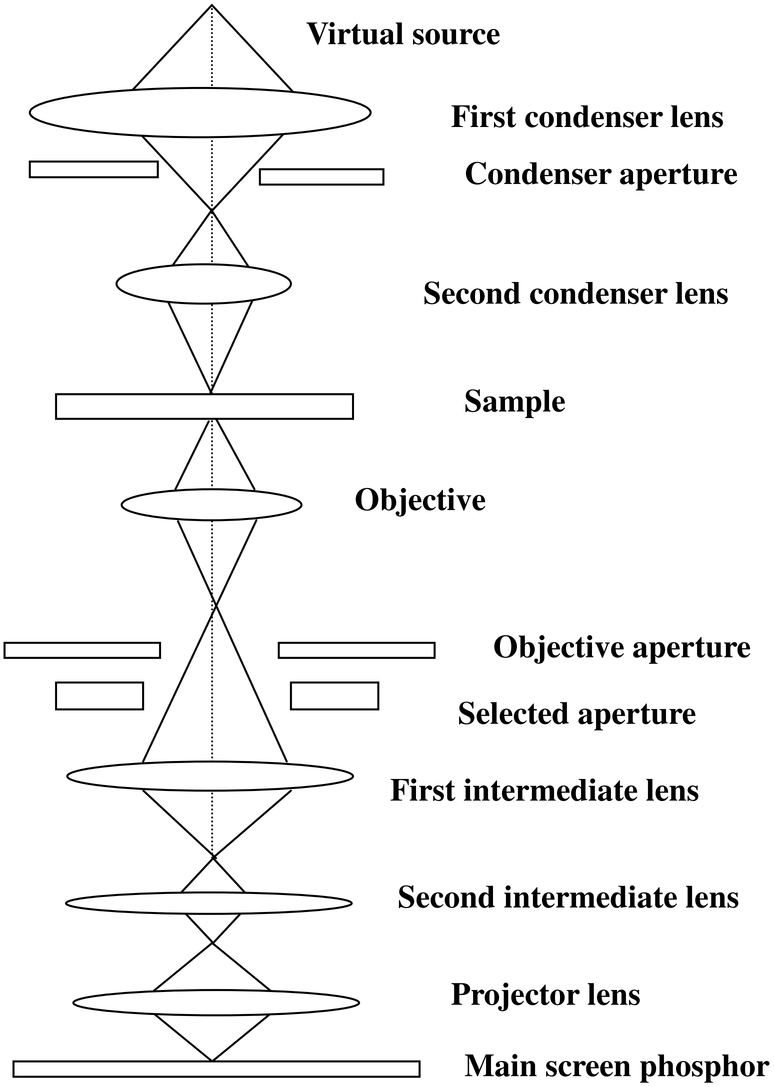

Fig. 2.4 Ray diagram of TEM

In TEM a beam of high energy electron (typically 100-400 keV) is generated at the gun chamber. The electron source may be tungsten filament or LaB_6 crystal or a field emission gun. The virtual source at the top shows the electron gun which produces stream of electrons. This stream is focused to a small and coherent beam by using condenser lenses. The focused beam then falls on the sample and some part of the beam is transmitted. The transmitted beam is then focused by the objective lens to form an image. Optional objective aperture and selected area metal apertures is used to restrict the beam. The objective aperture enhances the contrast by blocking the high angle diffracted electrons. Selected area aperture helps the user to examine the periodic diffraction of electrons by ordered arrangements of atoms in the sample. Then the image is passed through the intermediate lens and projector lens. Finally the image strikes the phosphor image screen and light is generated. Darker area of the image represents region of the sample from where fewer electrons were transmitted and lighter area of the image represents region of the sample from where more electrons were transmitted.

2.3.4 Component of TEM

Electron gun: At the top of the instrument electron gun is situated. The most common type of TEM has thermionic guns. Electrons are accelerated through a selected potential difference in the range 40-200 kV. The actual electron energy depends upon the nature of the specimen and information required. For some applications, if the specimen is relatively thick or very high resolution is required, it is advantageous to use much higher electron energies.

Condenser system: There are two or more condenser lenses below the electron gun. Diameter of electron beam is controlled by condenser lenses. With the help of condenser lens, operator is able to control the illuminated area of the specimen. Convergence angle of the electron beam is controlled by the aperture present between the condenser lenses. Quality of the image is affected by the size of condenser aperture due to spherical aberration of electrons which pass far from the optic axis [5].

Objective and intermediate lenses: The objective lens produces the first intermediate image and diffraction pattern. In the back focal plane, diffraction pattern is formed. The first intermediate lens can be operated in two settings. In the image mode it is focused on the image plane of the objective. The remaining projector lenses control the magnification of the final image on microscope screen. In the diffraction mode intermediate lens is focused on the back focal plane of the objective and finally on the viewing screen diffraction pattern is projected.

Projector system-image: First image produced by objective lens usually has a magnification of 50-100 times. This is further magnified by a series of intermediate and projector lenses and is finally projected on to the fluorescent screen.

Projector system -diffraction pattern: It is used to record the diffraction pattern from a selected area of the specimen. In selected area diffraction technique, an area of specimen is selected.

2.3.5 Imaging in the TEM

Contrast is defined as difference in intensity between two adjacent areas. Image contrast is developed by two ways either by selecting particular electrons or subtracting them from the imaging system. We can produce either bright field or dark field images by selecting the direct or scattered electrons, respectively. Non uniform intensity of electron beam is produced after scattering by the specimen. Therefore variable electron intensity strikes the viewing screen. To convert the scattering electron into the interpretable amplitude contrast either the direct beam or diffracted beam is selected to form BF and DF image, respectively.

2.3.6 Application of TEM

By TEM study we can get the following information regarding the sample.

Morphology: The size, shape and arrangement of the particles.

Crystallographic information: The arrangement of atoms in the specimen and their degree of order.

Information about composition: The elements by which the sample is composed and their relative ratios.

2.4 Scanning Electron Microscopy

2.4.1 Introduction

It is a type of electron microscope in which high energy electron beam scans the sample surface and image is produced on the screen. The interaction between electron beam and surface atom of the sample produces signal and provide information regarding surface feature, composition, etc. It produces high resolution image of the sample. Because of its large depth of focus it provides image having three dimensional appearance of the sample.

2.4.2 Sample preparation

For SEM, surface of the specimen should be electrically conducting and electrically grounded. Non-conducting specimen are usually coated with an ultra thin layer of electrically-conducting material. Gathering of static electric charge during electron scanning is prevented by coating. Coating prevents sparking and it increases surface signal and resolution particularly for samples with low atomic number.

2.4.3 Working principle

Initially electron beam is produced by electron gun placed at the top of the microscope. The electron beam passes through the lens and then it is focused on the sample. Finally the electron beam scans in a raster fashion over a rectangular area of the sample surface. During interaction with the sample, electron and X-rays are ejected. Basic ray diagram of SEM is shown in figure 2.5.

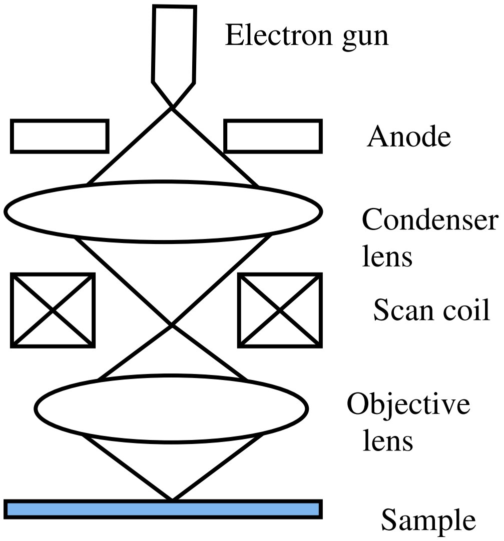

Fig. 2.5 Basic ray diagram of scanning electron microscope

Secondary electrons generally form image of surface structure in SEM. As the secondary electron has low energy, electron produced at higher depth is absorbed by the sample. Only surface electrons will be able to escape the specimen. The secondary electron will be deflected by Faraday cage and form image. Back scattered electrons have higher energy and hence they do not get deflected by Faraday cage. Number of electrons produced varies with position on the sample and therefore image contrast is developed. Number of back scattered electrons depends on specimens atomic number. High atomic number element and low atomic number element can be differentiated by production rate of back scattered electron.

2.4.4 Components of SEM

Electron gun: Electron gun supplies a large stable current in a small electron beam. Electrons are emitted from a hot tungsten filament situated at the top of the column. Emitted electrons are then accelerated down a vacuum column. There are three component of electron gun: filament, Wehnelt electrode and anode. Filament emits electrons, Wehnelt electrode controls the number of electrons leaving the gun and anode accelerates the electrons.

Electromagnetic lenses: Electromagnetic lenses are used to reduce the diameter of the electron beam to a small spot. The condenser lens is located closest to the electron gun and the objective lens is located closest to the specimen.

Scanning system: Scanning system helps the electron beam to scan the sample in raster fashion over a rectangular area.

Electron detector: Back scattered electrons have more energy and they directly excite the detector, which is mounted on the bottom of the objective lens. Secondary electrons are collected at the secondary electron detector by a positive charge placed in front of the detector. They are accelerated towards a scintillator screen and produces light.

2.4.5 Applications

Topography of the sample is studied by SEM. Elemental distribution of sample can also be studied by back scattered electron image.

2.5 UV -VIS spectroscopy

2.5.1 Introduction

During interaction of UV-visible radiation with matter various processes can occur. These are scattering, reflection, absorption, fluorescence/ phosphorescence and photo chemical reaction [6]. In general during measurement of UV-visible spectra only absorption is measured. Total energy of molecule is represented as $E_{total} = E_{electronic} + E_{vibrational} + E_{rotational}$. The energy of different levels are arranged in following manner. $E_{electronic} >$

$E_{vibrational} > E_{rotational}$. If the energy of the incident light is equal to the energy required to move an electron from lower energy state to higher energy state then the light will be absorbed. This transition occurs at very narrow band of wavelength.

2.5.2 Working principle of UV-VIS spectrometer

The principle of UV-VIS spectro-photometer is generally based on Beer-Lambert law which is used to measure the absorption coefficient of the material. $I = I_0 \exp(-\alpha x)$ (1), where α is the measured absorbance, I_0 is the intensity of the incident light at a given wavelength, I is the transmitted intensity, x is the path length through the sample. Ray diagram of UV-visible spectrometer is shown in figure 2.6.

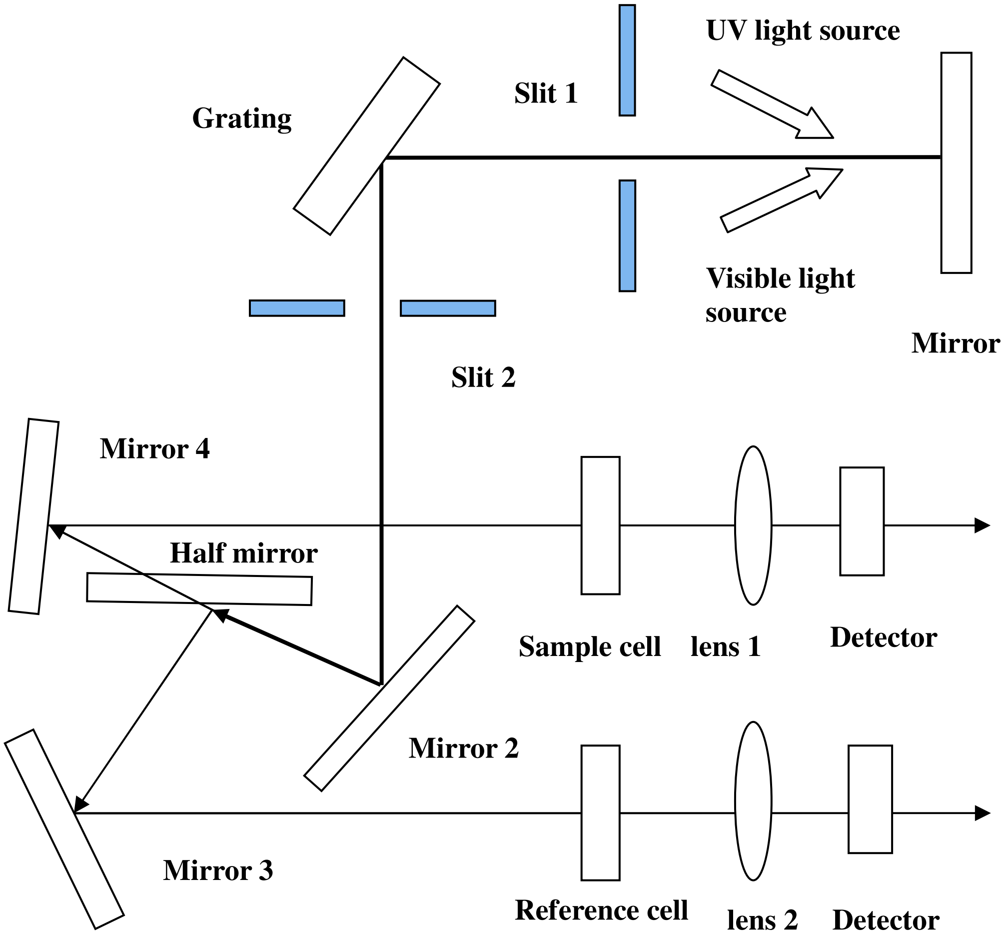

Fig. 2.6 Ray diagram of UV-VIS spectrometer

Light sources producing wavelengths in a broad range are used. When this light is diffracted through a grating it produces beam with continuous variation in wavelength which depends on the angle of the grating in the spectrometer [7]. Sources for UV- visible spectrometer consist of xenon or argon lamp (190-800 nm). Some time two different lamps are used, one is for UV region (Deuterium arc lamp 190-420 nm) and other is for visible region (Tungsten lamp 350-2500 nm). After being diffracted through grating each monochromatic beam is divided into two equal intensity beams. One beam is called the sample beam and other is called reference beam. After that measurement of intensities of these beams is done by PMT or photo diode, they are compared. The intensity of the reference beam, which has no light absorption, is defined as I_0. The intensity of the sample beam is defined as I.

2.5.3 Applications

With the help of UV-VIS spectroscopy we can get the following information.

a) Band gap of the material.
b) Transparency of the material in the UV and Visible range.
c) Presence of dopant/impurity having absorption band in UV-VIS region [8].

2.6. Dynamic light scattering

2.6.1. Introduction

In dynamic light scattering method dynamic fluctuations of light scattering intensity is measured. Due to Brownian motion of the particle dispersed in a liquid medium, fluctuation in concentration of particle occurs within the medium. This causes local inhomogeneities of the refractive index, and as a consequence fluctuation of intensity of the scattered light occurs. This is also known as photon correlation spectroscopy. In this method the sample is illuminated with laser light and fluctuation of scattered light are detected at known scattering angle θ.

2.6.2 Sample preparation

For making suspension, such a liquid medium is chosen so that particles remain suspended in the liquid and not dissolved. Very small amount of sample is dispersed in a liquid medium. Ultrasonication of the suspension is done to homogenize the sample. When the solution is ready for analysis, bottom of the cuvette should be checked. If there are particles at the bottom of the cuvette, then sample distribution is not proper and larger particle will not be measured. This type of suspension is not suitable for DLS measurement. Samples with large particles are not dispersed correctly, which may be due to not enough sonication, not enough dilution time, etc. For low density particles sample may exhibit opposite behavior. They come at the top of cuvette. When the solution is poured in cuvette, bubble formation should be avoided. Slowly tilting or tapping the cuvette on a hard surface, bubbles can be removed.

2.6.3 Working principle of dynamic light scattering

Dynamic fluctuations of intensity of scattered light occur due to random thermal (Brownian) motion of particles. The random motions in particles occur because of the collision of solvent molecules which are moving themselves due to their thermal energy. When laser light is incident on the liquid sample, scattering of light occur due to suspended particles. Scattered light may interfere constructively or destructively with time. The ray diagram of DLS is show in figure 2.7.

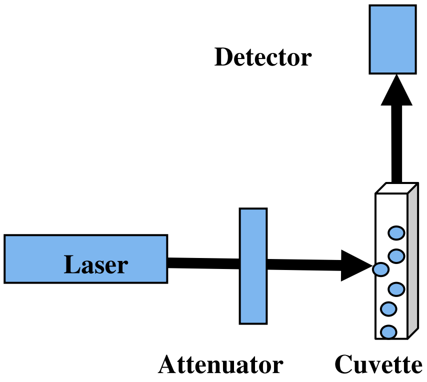

Fig. 2.7 Ray diagram of DLS

Due to this, variation in intensity occurs. The rate of intensity fluctuations depends on the size of the particles. For the small particles intensity fluctuation occur more rapidly than the large ones. Intensity fluctuation is characterized by computing the intensity correlation function and this gives the value of Diffusion coefficient (D) of the particles. The mean radius of the particle is calculated from Stokes-Einstein equation $R=k_BT/6\pi\eta D$, assuming that particles are spherical and non interacting. Where k_B is the Boltzmann constant, T is the temperature, and η is the viscosity of the solvent.

2.6.4 Components of DLS instrument

A dynamic light scattering system consists of following components:

1. **Laser:** Laser provides a light source to illuminate the sample contained in a cell.
2. **Detector:** A photo diode is used to measure the scattered light. Generally detector is positioned at either 173° or 90°.
3. **Attenuator:** It is used to reduce the intensity of laser light and thereby reduce the intensity of scattering. If too much light is detected then detector will become saturated. To avoid this attenuator is used.
4. **Correlator:** It compares the scattering intensity at different time interval and calculate the rate at which the intensity is fluctuating.
5. **Computer:** Correlator information is then given to a computer, where the software analyzes the data and calculates the size information.

2.6.5 Limitations

When particle motion is not random, DLS is not the correct technique to determine particle size. Upper size limit of detection depend on density of particle and solvent. We should not use more viscous medium to prevent sedimentation because it will slow down the Brownian movement. Similarly lower size limit depends on sample concentration, refractive index of sample compared to suspending medium, etc.

2.6.6 Application

This technique is used to determine the particle size and there distribution.

2.7 Thermoluminescence study

2.7.1 Introduction

Thermally stimulated luminescence (TSL) is the phenomenon of light emission during heating a previously irradiated substance. Initially sample should be annealed properly before irradiation.

2.7.2 Working principle of TLD reader analyzer

In TLD reader irradiated material is heated in particular heating rate. The sample is kept in the sample tray which is situated in front of PMT. Light emission of particular wavelength occurs during heating of the irradiated material. The emitted light enters into the PMT. The visible photon is converted into electrical signal inside PMT. The photo multiplier tube is a very sensitive detector for UV and visible light. Photo cathode is the main radiation sensor which is placed inside a tube. When light falls into the photo cathode, electron emission takes place. These photo electrons are accelerated and focused by the focusing electrode on to the first dynode. In first dynode the number of electrons is multiplied by means of secondary emission. In every dynode secondary electron emission is repeated and anode collects all electrical signal. The recorder continuously records the measured data as a function of temperature. Infrared cut-off filter is attached just below the PMT window to remove infrared radiation and allow only visible light. Block diagram of TLD reader is shown in figure 2.8.

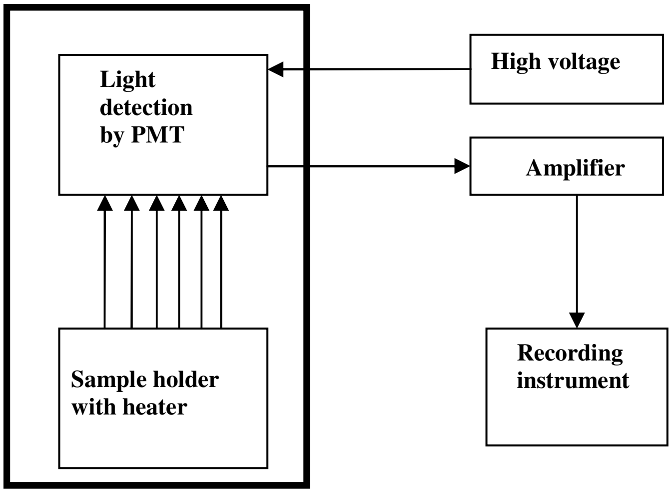

Fig. 2.8 Block diagram of TLD reader

The temperature of TLD reader can be increased from room temperature to 400°C with different heating rate from 0.5°C/sec to 10°C/ sec. Reader factor is very important parameter for determining dose. Reader factor is the total area under the curve after subtracting the background per one mrem (milli rem) absorbed dose. One reader factor is valid for only particular HV and a particular class of material.

2.7.3 Application

Graph of temperature versus thermoluminescence intensity is called glow curve. From the shape of the glow curve, order of kinetic (first order or second order), activation energy and frequency factor of the material can be determined [9]. Total area under the curve gives the total counts which measure the absorbed dose.

2.8 Birefringence interferometry

2.8.1 Introduction

Birefringence is the optical property of a material whose refractive index depends on the polarization and propagation direction of the light. In birefringence interferometry study polarized laser beam is made to incident on the polished anisotropic crystal sample and interference pattern form when emergent light passes througth the analyser.

2.8.2 Working Principle

When polarized laser light passes through the birefringent crystal the light ray decomposes in to two ray having different polarization (mutually perpendicular). These two rays of different polarization then pass through the analyzer. Now the component of electric vector parallel to the analyzer will pass through and they will interfere and interfernce pattern is formed on the screen. Ray diagram of birefringence interferometry is shown in figure 2.9.

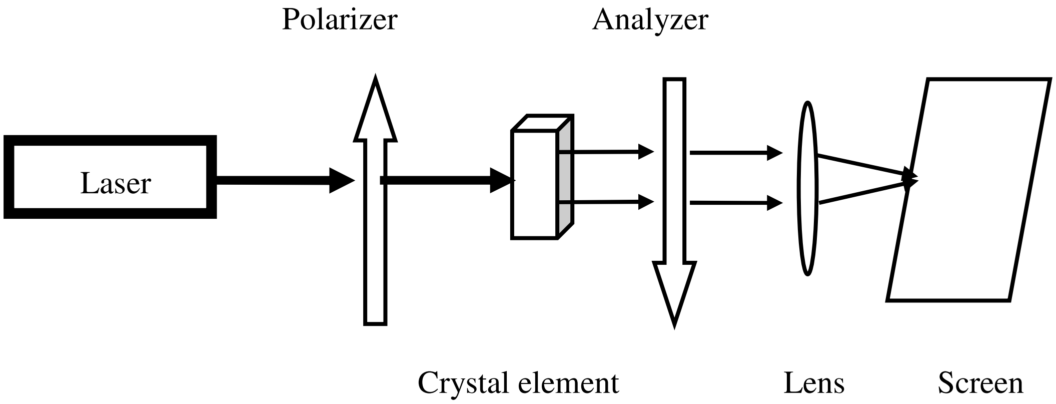

Fig. 2.9 Ray diagram of the birefringence interferometry set up

2.8.3 Applications

In this study by observing the parallelism and straightness of the fringe, we can check the refractive index homogeneity of the crystal.

2.9 Conoscopic study

2.9.1 Introduction

The conoscopic interferometry study is a nondestuctive technique to check optical homogeneity of the anisotropic crystal qualitatively and to determine the optic axis by observing the interference pattern.

2.9.2 Working principle

When a converging beam of white light polarized along a specific direction is passed through the crystal plate, the beam splits into *e*- and *o*-rays. The phase difference between the two rays is $\delta = (2\pi d / \lambda \cos\theta) * (n_e - n_o)$, where d is the thickness of the sample, n_e and n_o are the refractive indices of *e* and *o* rays, respectively, and θ is the angle of refraction. When these two rays emerge from the crystal, they recombine along the analyzer axis. As a result concentric circular coloured ring are formed due to constructive interference of various colur present in white colour. These concentric colour rings are called isochromes. Number of isochrome depends on the thickness of the crystal plate and the birefringence of the material. The polarization direction will be different for different ray path. Those rays whose polarization directions are parallel to the polarizer will be extinct and as a result two perpendicular black strips formed on isochrome. These are called isogyer. The crossing point of these two isogyer is called melatope. This is the location of the optic axis. The ray diagram for conoscopy study is shown in figure 2.10.

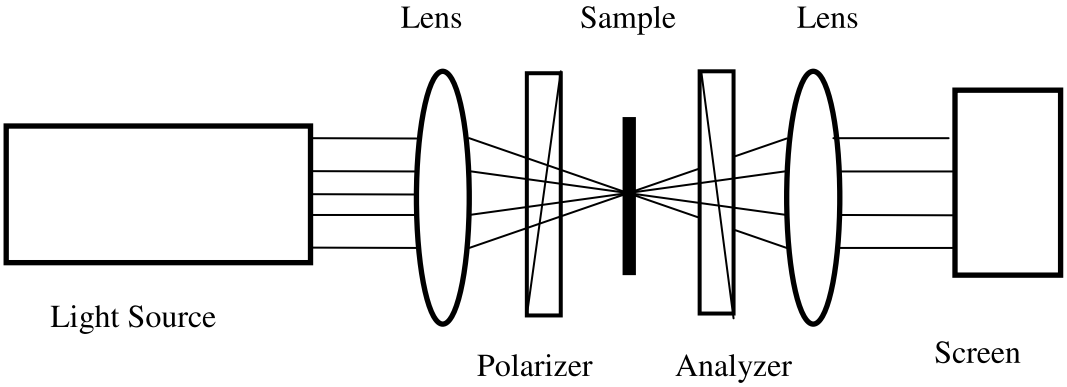

Fig. 2.10 Ray diagram for conoscopic pattern

2.9.3 Applications

Determination of direction of optic axis and to study optical homogeneity of the crystal.

References:

1. V. K. Pecharsky and P. Y. Zavalij, Fundamentals of powder diffraction and structural characterization of materials, Springer, 2009.
2. C. Suryanarayana and M. Grant Norton, X-ray diffraction: A Practical Approach, Plenum Press, New York and London, 1998.
3. J. P. Sibilia, A Guide to Materials Characterization and Chemical analysis, 2nd Edition, Wiely-VCH, 1996.
4. D. B. Williams and C. B. Carter, Transmission Electron Microscopy, A text book for material science, Plenum Press, New York, 1996.
5. P. J. Goodhew, J. Humphreys, R. Beanland, Electron microscopy and analysis, Third edition, Taylor & Francis, 2001.
6. T. Owen, Fundamentals of UV-visible spectroscopy, Agilent Technologies, 2000.
7. J. H. Simmons and K. S. Potter, Optical Materials, Academic Press, USA, 2000.
8. M. A. White, Properties of materials, Oxford University Press, 1999.
9. S.W. S. McKeever, Thermoluminscence of solids, Cambridge University Press, 1985.

Chapter 3

Growth and Characterization of Undoped and Doped Lithium Niobate Crystals

3.1 Introduction

Lithium niobate, $LiNbO_3$ (LN) is very important material due to its excellent electro-optic, acousto-optic, ferroelectric and photorefractive properties. Lithium niobate doped with transition metal ions such as Cu, Fe, Mn, Ce etc., shows excellent photorefractive property and is potential material for holographic memories [1]. Defects generated during growth and due to dopant mainly control the photorefractive properties and quality of holography [2, 3]. Lithium niobate ($LiNbO_3$; LN) single crystal is a well studied material for volume holographic memory applications because of its good mass productivity and excellent photorefractive properties such as long storage time and relatively high coupling gain constant [4-7].

3.1.1 Structure of $LiNbO_3$

Lithium niobate has rhombohedral crystal structure, belonging to space group R3c below the Curie temperature. It is more convenient to describe the lattice using hexagonal axes. This triples the volume of unit cell as compared to the rhombohedral unit cell. The unit cell in hexagonal lattice is defined by one of the three equivalent a_H lattice vector and polar c_H lattice vector. Here the angle between a axes and c axis is 90°. The volume is given by $\sqrt{3}/2\ a^2c$ and it contains six formula units [8]. The lattice parameter of LN crystal are a=0.5157 nm and c= 1.3856 nm. The atomic arrangement within the stoichiometric hexagonal unit cell consist of six lithium niobate with Li and Nb ions located on the polar c- axis and the o atoms in general position. $LiNbO_3$ formed by chain of distorted niobium–oxygen octahedra and lithium- oxygen octahedra. Common faces of octahedra are along the polar axis c. In the non-polar centro-symmetric phase at $T > T$c (curie temperature) the Li^{1+} ions are localized within the oxygen planes, whereas the Nb^{5+} ions are in the center of the oxygen octahedra (between the oxygen planes). In the ferroelectric phase at $T < T$c, the Nb^{5+} ion and Li^{1+} ion are displaced from the center of oxygen octahedra. This displacement along the polar axis gives rise to the dipoles and producing spontaneous polarization. If this displacement becomes zero, then polarization becomes zero and crystal is paraelectric. Similarly, equal but opposite displacement reverse the spontaneous polarization. Octahedral interstitial are one-third filled by Li ions, one-third by Nb ions and one-third are empty. Oxygen triangles are arranged layer by layer. The alternation of cation sites may be schematically depicted as a chain Li–Nb–Vacancy Li–Nb–Vacancy (fig. 3.1).

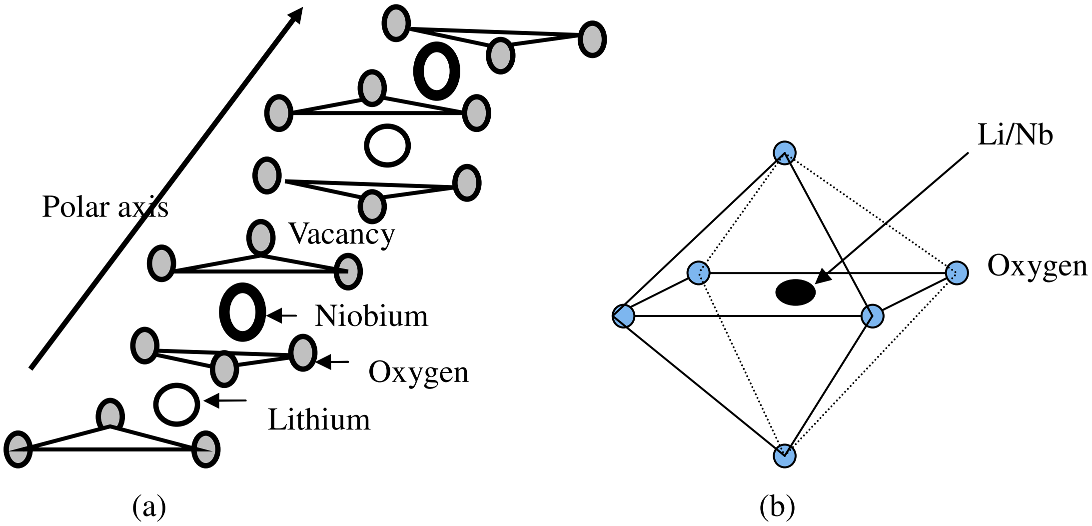

Fig. 3.1 (a) The ideal lithium niobate with the chain Li–Nb– vacancy, Li–Nb–vacancy (b) One single octahedra occupied by Li/Nb

The Li octahedron is larger, than the Nb one, because the distances between a Li ion and the closest oxygen ions are 206.8 and 211.2 pm, whereas those for an Nb ion are 188.9 and 211.2 pm, respectively [9]. Stoichiometric lithium niobate melt incongruently. According to phase diagram the $LiNbO_3$ structure is stable within Li_2O concentrations from 47 to 50 mole %. The congruently melting (Li-deficient) composition corresponds to the oxide concentrations 48.45 mole % Li_2O and 51.55 mole % Nb_2O_5 [10] with the ratio [Li]/[Nb] = 0.94. Correspondingly, the congruent $LiNbO_3$ (denoted often as CLN) contains about 6% empty Li sites in the lattice. X- ray diffraction shows that, in congruent lithium niobate, the Li site contains 94.1% Li and 5.9% Nb whereas the Nb site contains 95.3% Nb and 4.7% vacancies, for the O site containing 100% oxygen [11]. Non stoichiometric lithium niobate may be represented by chemical formula $[Li_{(1-5x)}Nb_{(5x)}]Nb_{1-4x}O_3$, Li site occupancy is given in square bracket. The structure remains stable for x up to 0.02 [10].

3.1.2 Phase diagram of $LiNbO_3$

The lithium niobate shows a solid solubility range from 50 mole % to 45 mole % Li_2O [12, 13]. The phase diagram of the system Li_2O–Nb_2O_5 is shown in fig. 3.2 [11,14]. From the phase diagram it is observed that congruent composition of the crystal is 48.6 mole % Li_2O and crystal melts congruently at 1253°C. Crystals grown with this melt composition have exactly the same cation ratio as the melt and the liquid composition remain unchanged during the growth process and grown crystal become homogeneous throughout the length. The crystals grown from any other composition leads to non homogeneity in composition along the pulling direction.

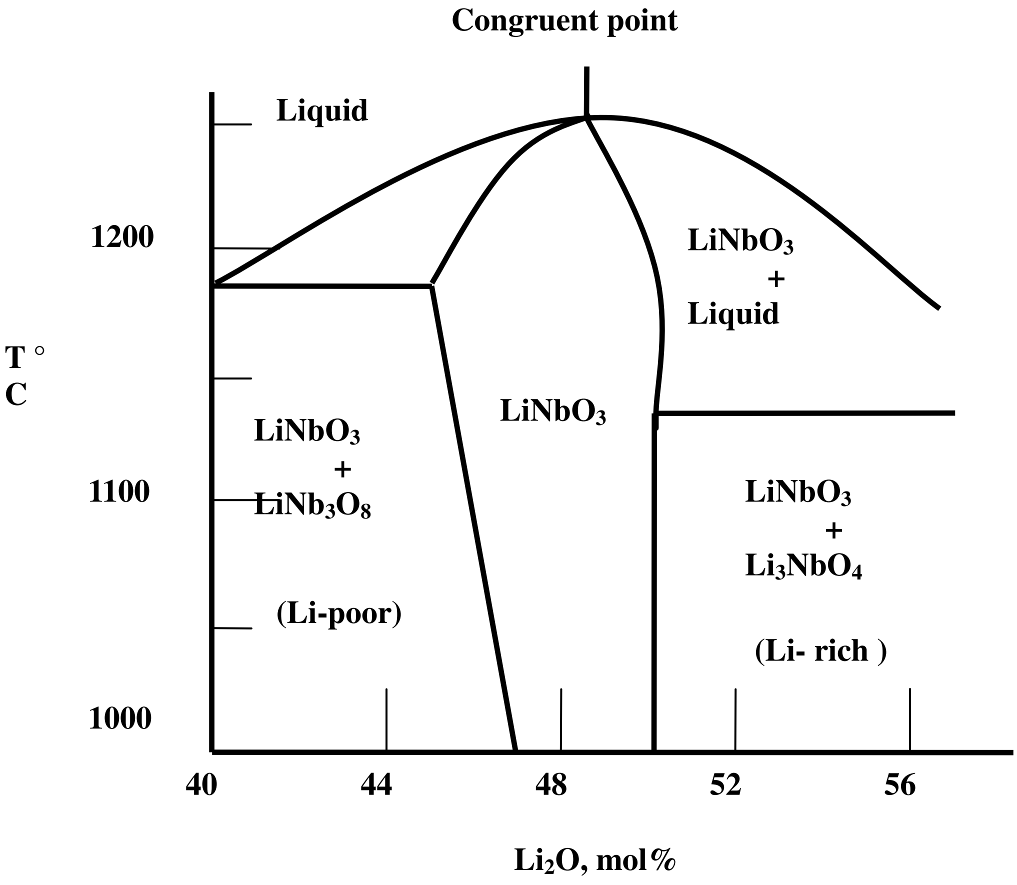

Fig. 3.2 Phase diagram of Li_2O- Nb_2O_5 system

3.1.3 Problems arises during growth of good quality crystal

For device purpose, transparent, good optical quality and uniform diameter crystal are required. To grow device quality crystal it is required to optimize several growth influencing parameters. The main problem in growth of uniform diameter crystal is the unstable property of crystallization front. When the diameter of the crystal reduces, the quantity of heat flow through the crystal also reduces and hence temperature near the melt solid interface increases. As a result crystal diameter reduces. In the same way heat loss through the crystal increases as the crystal diameter is increased. This leads to decrease in temperature near the interface and hence crystal diameter increases further. Therefore optimization of the growth parameters to get good quality, uniform diameter crystal is really a difficult task. In general, constant diameter crystals are more perfect than variable diameter. This is because diameter has dependency on creation as well as propagation of dislocation inside the crystal. It is required to have linear temperature field within the crystal to grow crystal with minimum dislocation density. This is achieved by minimizing the radial and axial temperature gradients. Ideally it is preferred to have flat interface (melt to crystal) during Cz growth. However, in practice, the interface is not stable and tends to be either convex or concave. Out of the two shapes, the convex interface is preferable because the spurious nuclei and defects (dislocations) formed at the periphery of the crystal tend to grow out of the crystal volume, whereas these move towards the crystal volume in case of concave interface [15].

3.1.4 Material potential

Growth of lithium niobate crystal is very difficult. Optimization of various growth parameters such as pulling rate, rotation rate, axial temperature gradient above and below the melt level, crystal to crucible temperature ratio, post growth cooling rate is required to get good optical quality and almost uniform diameter crystal. Undoped, Fe doped and Fe: Mn doped lithium niobate crystals have been grown by optimizing various growth parameters. Iron-doped lithium-niobate crystals are currently under intense investigation for application in holographic storage systems [16–19]. Lithium niobate is a most promising photorefractive material because of its large electro optic coefficient. Sensitivity of lithium niobate can be increased by several orders of magnitudes by optimizing charge transport mechanism. The sensitivity also depends on concentration of two valance states Fe $^{2+}$ and Fe $^{3+}$ inside the crystal [20-24]. The relative concentration of Fe $^{2+}$ and Fe $^{3+}$ ions in a given crystal of Fe doped lithium niobate can be altered by oxidation or reduction treatment [20,21,23]. Fe:Mn doped lithium niobate crystal is also very useful for non volatile holography [25]. In energy band diagram Fe and Mn trap levels resides at different position within the band gap. Position of Fe trap level is slightly higher than that of Mn [26]. The electrons are initially in the deeper traps. Light of short wavelength (with high-energy photons) can transfer some of these electrons to the shallower traps via the conduction band. This makes the recording of the holograms using longer wavelength light feasible. The final hologram records in the deeper traps and, therefore, cannot be erased during the read-out by the recording (long-wavelength) light. Therefore double doped Lithium niobate crystal can be used as non volatile holographic memory. In view of the importance of improving the photo refractive property of Fe doped lithium niobate and Fe: Mn doped lithium niobate for potential use in holographic storage application, photo refractive properties of these crystals have been studied. Illumination of the crystals with a light pattern excites in the bright regions electrons from Fe^{2+} to the conduction band. The generated free charge carriers migrate until they are trapped by Fe^{3+} in darker areas. Space-charge fields build up and these fields modulate the refractive index via the electro-optic effect. It is reported that extra ordinary refractive index increases in proton exchanged LN sample. To utilize this property in holographic application, photorefractive study of proton exchanged samples were studied. Enhancement in diffraction efficiency in proton exchanged Fe doped LN and Fe: Mn doped LN was observed.

3.2 Growth of undoped and doped lithium niobate crystals

3.2.1 Material synthesis

This process involves the following steps

1. Drying of chemicals: Before weighing the chemicals, Li_2CO_3 was dried at 300°C up to 3-5 hr to remove moisture.
2. Weighing: Charges were weighed by electronic balance with accuracy up to 0.0001 gm for congruent composition (48.6 mole % of Li_2O and 51.4 mole % Nb_2O_5).
3. Mixing through Ball miller: Ball miller mixed charges properly. By this process particle

size of the charges were also decreased. When particle size becomes small total surface area for reaction increases. This helps for better solid-state reaction.

4. Pallet preparation: Pallets of diameter 20 mm were made from the above charge by applying pressure 2 kg/m^2 in hydraulic press. This helps in solid-state reaction. Every particle comes in close contact with neighboring particle.

5. Solid state reaction: Pallets were heated at 950 °C for 24 hrs for solid state reaction.

6. Checking of phase through XRD: Phase of polycrystalline powder was confirmed by XRD.

To get doped crystal dopant were mixed initially before solid state reaction. Here 0.03 wt% Fe_2O_3 have been doped for Fe doped LN crystal and 0.03 wt % Fe_2O_3 and 0.01 wt% MnO_2 have been doped for Fe: Mn co doped LN crystal.

3.2.2 Crystal growth

Pallets of poly crystalline powder were placed in a 60 mm diameter and 60 mm height platinum crucible for crystal growth runs in air atmosphere. The charge was melted using induction-heating system. The melt was homogenized for 1-2 hours at a temperature little above the melting point. Temperature of the furnace was controlled by PID controller with R-type thermocouple. Gradient of the furnace is a crucial parameter for the growth of lithium niobate crystal. Crucible has been kept inside the furnace in such a way that sharp temperature gradient starts after the solid-liquid interface. In the present experiments the temperature gradient of 75˚C/cm was maintained above the melt. The crucible was kept in this high temperature gradient region. The fundamental aspect of achieving crystal from melt technique is to provide a path for the steady flow of latent heat of crystallization. Highest achievable growth rate can be obtained from the heat balancing at the solid/melt interface.

Latent heat at the interface + heat flux from the melt of the crystal = heat flux from the crystal surface.

$$Lg\rho A + K_m\left(\frac{dT}{dX_m}\right)A = K_s\left(\frac{dT}{dX_s}\right)A \quad \text{or} \quad g = \frac{1}{L\rho}\left[K_s\frac{dT}{dX_s} - K_m\frac{dT}{dX_m}\right]$$

Where g=growth rate, L= latent heat, ρ = density, A= cross sectional area, K_m= thermal conductivity of melt, K_s = thermal conductivity of solid, dT/dX_m = temperature gradient below the melt level and dT/dX_s = temperature gradient above the melt level. From the above equation it is observed that the growth rate of the crystal is inversely proportional to the latent heat and density. It is linearly proportional to the thermal conductivity and axial temperature gradient within the solid. Keeping in mind the above relations values axial temperature gradients below and above the melt was decided. In crystal growth chamber how heat flows from melt to surrounding via crystal is shown in figure 3.3.

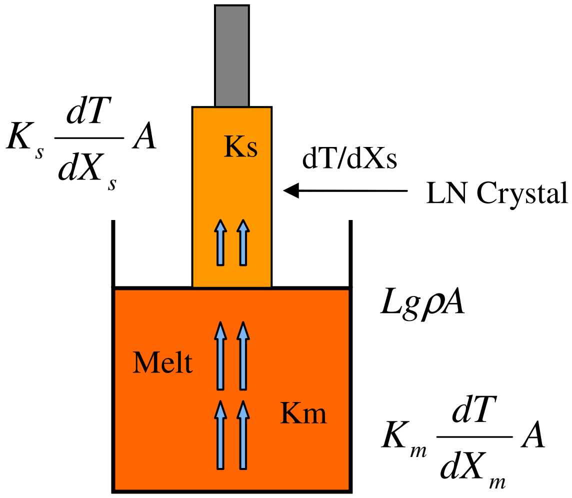

Fig. 3.3 Heat flow mechanism in melt and crystal

To maintain required temperature gradient proper thermal insulation is required. Here zirconia bricks and muffles were used as insulating material. Photograph of zirconia brick and cylinder are shown in figure 3.4.

Fig. 3.4 Zirconia bricks, muffle and crucibles

In our experiment radial gradient was nearly zero. The axial gradient acts as a driving force for crystallization process. The axial gradient should be large to overcome the constitutional super cooling. However, if the gradient is very large, it may results into high thermal stresses inside the crystal. The maximum acceptable axial temperature gradient is given by

$$\left(\frac{dT}{dx}\right)_{\max} \propto \left[\frac{4\varepsilon}{\alpha a^{\frac{3}{2}}}\right] h^{\frac{1}{2}}$$

where, ε =breaking strain of the crystal, α= thermal expansion coefficient, a= radius of the crystal, h= heat loss per unit area per unit time from crystal surface. Therefore, some optimized axial gradient is required to grow good quality crystals. Axial temperature gradient of the furnace above and below the melt level is shown in figure 3.5 (a, b).

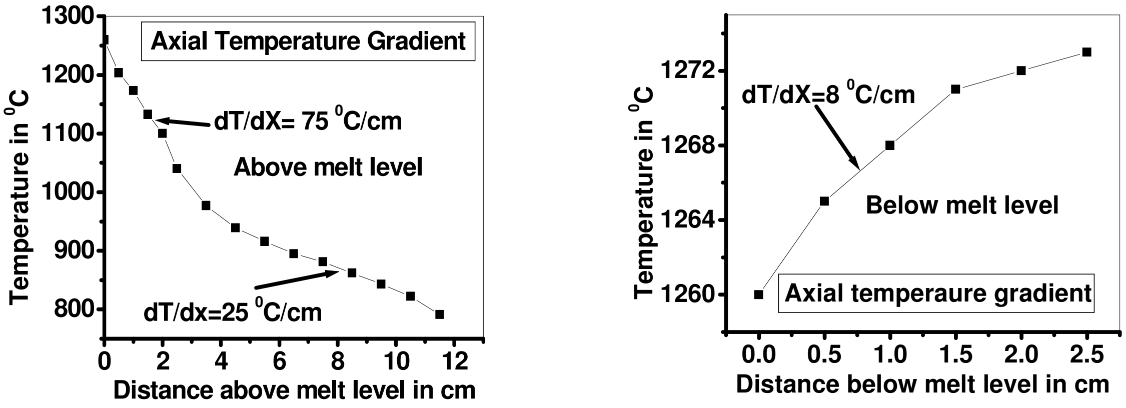

(a) (b)

Fig. 3.5 Axial temperature gradient of the furnace (a) above the melt level and (b) below the melt

A seed crystal in [001] orientation was inserted into the melt at 1-2 degrees above the melting point. This seed direction has smaller thermal expansion coefficient. To avoid cracking this seed direction was chosen. Seed with alumina rod is shown in figure 3.6.

Fig. 3.6 Seed crystal with alumina rod

Initially we start with growth of undoped crystal with following growth parameters

Growth Temperature:	1260 °C
Pulling rate:	4 mm/hr
Rotation rate of the seed:	6 rpm
Axial temperature gradient:	75 °C /cm
Crystal to crucible diameter ratio:	not fixed
Cooling rate after growth:	30/hr
Growth environment:	Air

Specially designed growth chamber was used for the crystal growth. Photograph of crystal growth system is shown in figure 3.7.

Fig. 3.7 Crystal Growth System used for CZ Method

With above growth parameters undoped, Fe doped and Fe: Mn doped crystal have been grown. The grown crystals were transparent, crack free but nonuniform diameter. Photo of some grown crystal are shown in figure 3.8 (a, b, c).

(a) (b) (c)

Fig. 3.8 Photograph of (a) undoped (b) Fe doped and (c) Fe: Mn doped LN crystals

Growth of uniform diameter $LiNbO_3$ crystal is very difficult. However, by optimizing furnace gradient and the growth parameters smaller size crystals with almost uniform diameter can be grown. Pulling rate is also important factor to grow constant diameter crystal. Initially pulling rate was 4 mm/h for first hour and then it had been reduced to 3 mm/h to increase the diameter and kept same throughout the growth run. Ratio of crystal to crucible diameter was also optimized to grow uniform diameter crystal. It was experimentally found that for crystal to crucible diameter ratio about 1:4, results in nearly constant diameter crystal without changing the temperature during growth. In this situation the rate of change of melt level in the crucible is small and therefore the crystal and melt interface stays in nearly same temperature zone. How the melt level goes down with time is shown in figure 3.9.

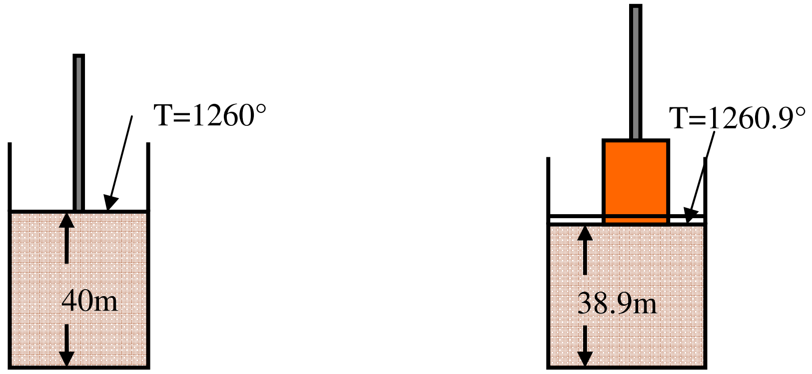

Just after dipping the seed **After six hour**

Fig. 3.9 Position of melt level with time

It has been calculated that when pulling rate is 3 mm/hr, melt level down rate will be 0.18 mm/hr. After six hour melt level goes down by approximately 1.1 mm and corresponding increase of temperature of melt level was only 0.9 °C. During growth of crystal proper rotation rate is also essential. The rotating crystal acts as a centrifugal pump drawing the liquid melts axially, while ejecting it in radial direction. The radially outward flow due to rotating crystal can control a radial inflow of the fluid driven by buoyancy. Here we have kept rotation rate 6 rpm during the growth period. Impurity distribution inside crystal is also an important factor. The distribution of impurity in the solid after solidification depends primarily on convection. The main effect is due to the enrichment of the liquid far from the interface by convection. This is described by an effective distribution coefficient, $k_e = Cs/C_L^*$ which is usually different from the distribution coefficient, $k = Cs/C_L$ obtained from the phase diagram, k_e depends on k, the growth rate, the crucible shape, stirring, etc [27, 28]. To get homogeneously doped crystal segregation coefficient should be 1. In case of smaller diameter crystal (smaller with respect to crucible) doping concentration throughout the crystal will be almost same even if the segregation coefficient is not 1. This is a very important parameter to get a crystal with almost homogeneous dopant concentration. After growth is completed post growth cooling is also an important step. The rate at which the grown crystal must be cooled without developing any cracks depends upon crystal radius (a), thermal expansion coefficient (α) and breaking strain (ε). Maximum post growth cooling rate is given by

$$\left(\frac{dT}{dt}\right)_{\max} \infty \frac{\varepsilon}{\alpha a^2}.$$

Grown crystals were cooled in two step [29]. Up to 1000°C crystal was cooled 30°C/hr and then the crystal was cooled 100°C/hr up to room temperature. We have grown nearly constant diameter crystals with 12-14 mm in diameter and 40-45 mm in height. Photograph of uniform diameter Fe: LN crystal is shown in figure 3.10.

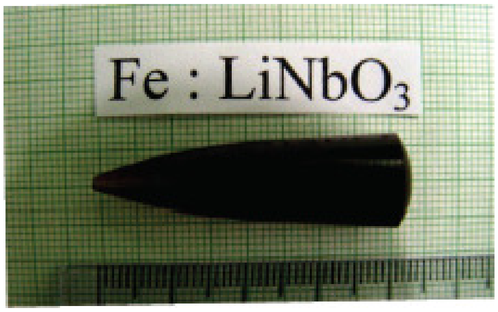

Fig. 3.10 Photograph of uniform diameter Fe: LN crystal

3.3 Characterization of grown crystals

A small portion of the crystal wafer was crushed properly and powder XRD was done for crystalline phase identification. Thin wafers from grown crystal were cut, lapped and polished. These polished wafers were used for UV-VIS transmission studies and birefringence interferrometry analysis. Polished samples are shown in figure 3.11.

(a) (b) (c)

Fig 3.11 Polished sample of (a) undoped LN (b) Fe doped LN (c) Fe: Mn: doped LN

3.3.1 X-ray diffraction study

The X-ray powder diffraction of grown crystal was carried out by GEIGER FLUX diffractometer. A small portion of crystal piece was crushed and fine powder was prepared using morter pestle. Data of powder XRD were taken using Cu Kα radiation at 1.5426 Å. The diffraction patterns were taken from 20 degrees to 70 degrees with a step size of 0.02 degree. Figure 3.12 (a, b, c) shows the powder XRD pattern for undoped LN, Fe doped LN and Fe: Mn doped LN crystal.

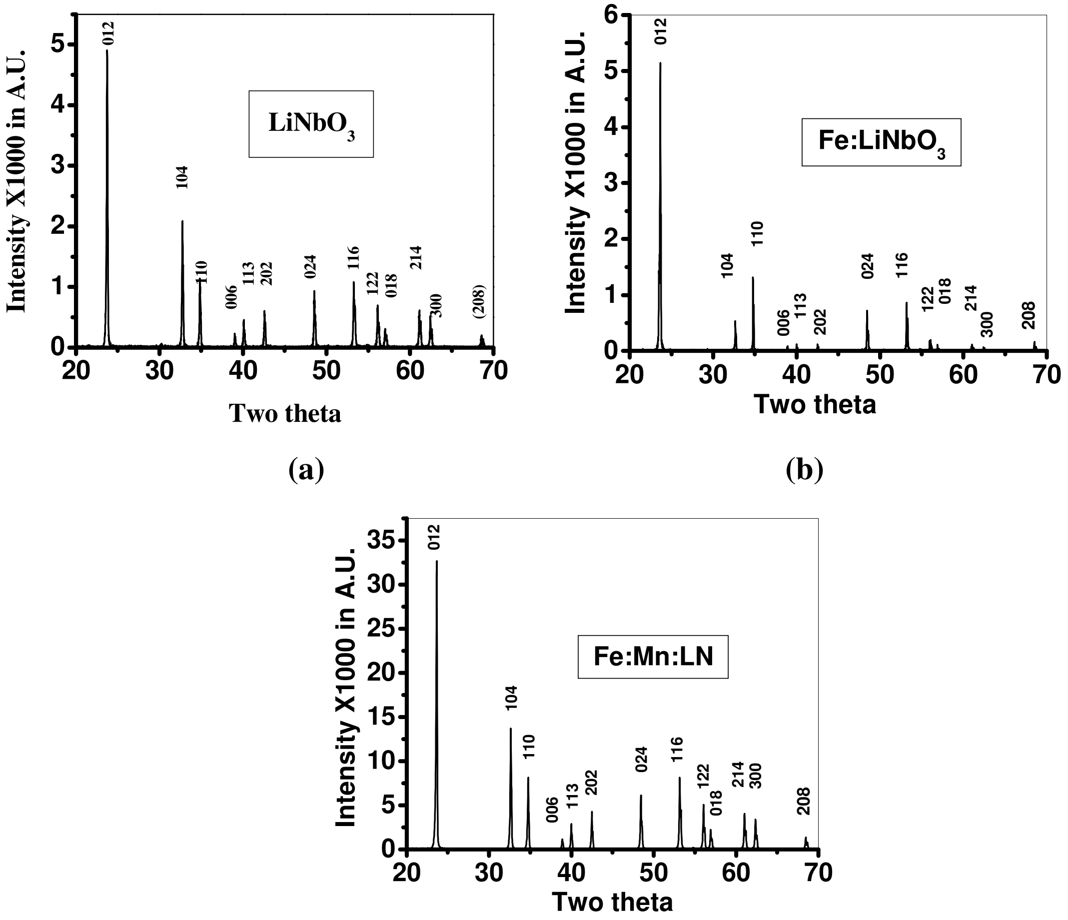

(a) (b)

(c)

Fig. 3.12 Powder XRD pattern for (a) undoped $LiNbO_3$ (b) Fe doped (c) Fe: Mn doped $LiNbO_3$ crystal

The XRD pattern shows single phase. The small dopant does not have any effect on the crystalline phase.

3.3.2 UV-VIS transmission spectra study

Plates of thickness 2 mm were cut from as grown LN crystals. These plates were lapped and polished using alumina powder. Transmission spectra were recorded using UV-VIS- spectrometer (JASCO model). There are two light sources for covering entire wavelength range 190-3200 nm. Deuterium lamp covers the lower wave length region having switching wavelength 190 nm and halogen lamp covers the higher region of wavelength with switching wavelength 900 nm. Minimum step of wavelength scan was 0.1 nm.

Transmission spectra of polished crystal wafers of as grown crystal were taken and analyzed. It was observed that the absorption edge shift towards the higher wavelength compared to congruent $LiNbO_3$. Fig 3.13 (a, b, c) shows the transmission spectra for undoped, Fe doped and Fe: Mn doped $LiNbO_3$ crystal respectively. For transition metal ion surrounded by an octahedron of negative ions, the d- orbital pointing directly towards the oxygen ions, $d_{x^2-y^2}$ and d_z^2, will be strongly repelled and so raised in energy compared to those pointing between the oxygen ions. By this process crystal field splitting generates energy gap between the lower t_{2g} groups and higher e_g group. The absorption band related to ^2e_g and $^2t_{2g}$ transitions has been observed at 488 nm for doped LN crystal. The crystal structure of $LiNbO_3$ consists of alternate layers of oxygen atoms arranged in three-fold fashion and forming oxygen octahedra along c-axis. The two third of these are occupied by cations and rest remains as vacant. Further, $LiNbO_3$ is a typically non stoichiometric materials having high concentration of intrinsic defects (Nb antisites and Li vacancies). The ionic radii of Nb^{5+}, Li^{1+} and Fe^{3+} and Mn^{2+} ions are almost same, Hence, Fe and Mn in principle can replace both the Li and Nb ions, but preferably it replaces Li ions. This is because of its lighter mass and hence high mobility compared to Nb ions. It can be seen in transmission studies that absorption edge is shifting towards higher wavelength. This red shift mechanism can be explained on the basis of decrease in the Li/Nb ratio of the crystal with Fe doped LN crystal and Fe: Mn doped LN crystal. Further, the transmission spectra of different plates along the growth direction of our crystal have been taken to check the axial homogeneity of the grown crystal. No change in UV cut off was observed.

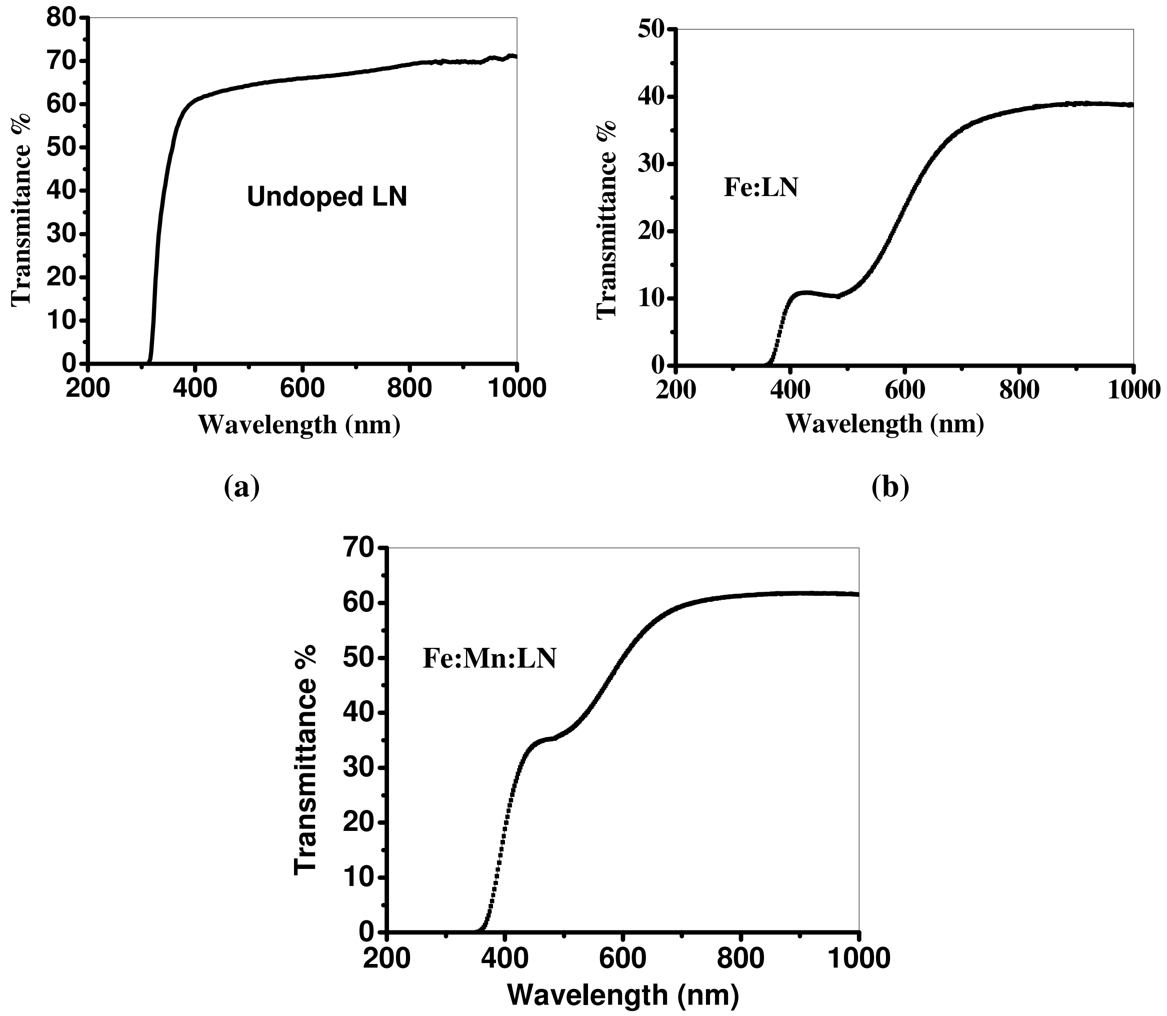

(a) (b)

(c)

Fig. 3.13 UV-VIS Transmission spectra of (a) undoped LN (b) Fe: LN (c) Fe: Mn: LN sample

3.3.3 Birefringence interferometry study

Plates of thickness 2mm were cut from grown crystal and then polished properly for birefringent interferometry study. In birefringence interferometry experiment polarized He-Ne laser beam is made to incident on the polished crystal sample. On passing through the crystal the light ray decomposes in to two ray of different polarization. These two rays of different polarization then pass through the analyzer. Now the component of electric vector parallel to the analyzer will pass through and they will interfere.

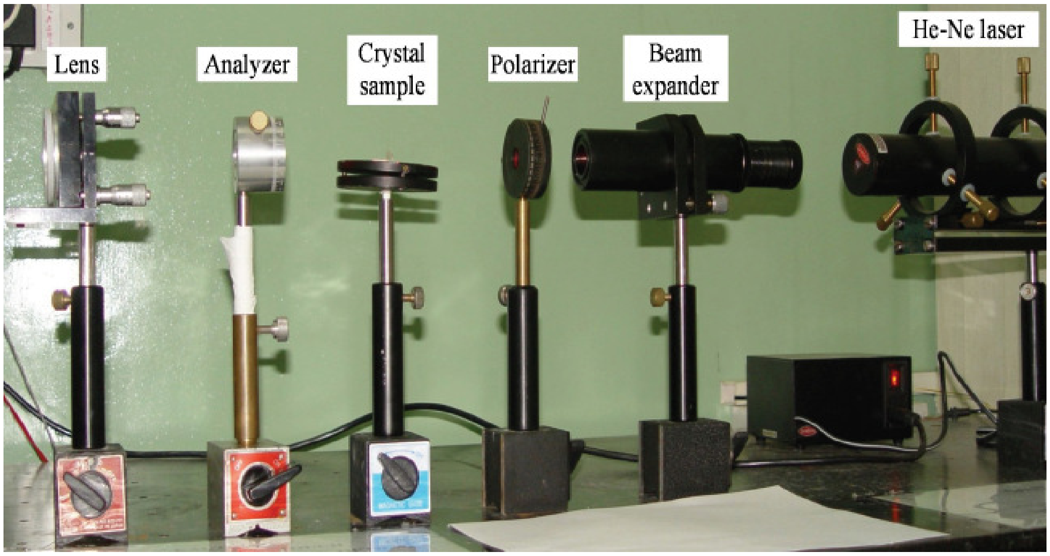

Fig. 3.14 Photograph of birefringence interferometry set up

The photograph of birefringence interferometry setup is shown in fig 3.14. The interferogram of Fe: LN and Fe: Mn: LN crystal is shown in figure 3.15 (a, b). The parallelism and straightness of the fringe indicates the refractive index homogeneity of the crystal.

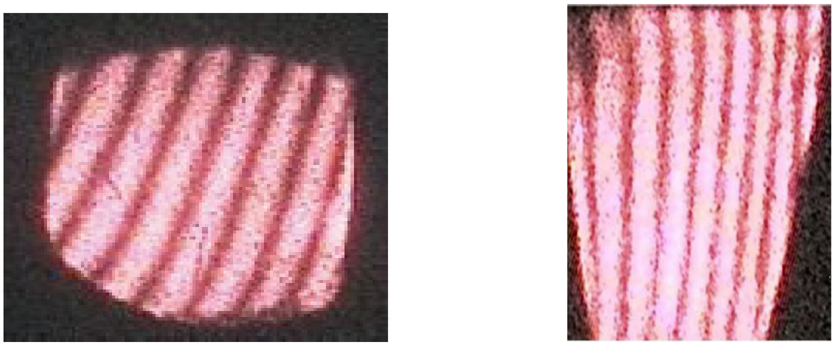

(a) **(b)**

Fig. 3.15 Birefringence interferogram for (a) Fe: $LiNbO_3$ crystal plate and (b) Fe: Mn: LN crystal plate

3.3.4 Conoscopic study

The conoscopic interferometry is performed to get qualitative information about the optical homogeneity of the grown crystal and the direction of the optic axis. Properly polished plate cut perpendicular to C-axis were used for conoscopic study. When a converging beam of white light polarized along a specific direction is passed through the crystal plate, the beam splits into two rays having electric vector vibration perpendicular to each other. When these ray emerge from the crystal plate, they again pass through the analyzer and their components interfere. This gives concentric fringes of interference colors which are called isochromes. These are superimposed by a black cross, called isogyres. The center of the cross is the location of the optic axis, which is called melatope. The interference patterns were captured by polarizing microscope (OLYMPUS). The photo graph of microscope is shown in 3.16. The interference pattern is called the conoscopic pattern.

Fig. 3.16 Photograph of polarizing microscope

Conoscopic pattern of Fe doped LN and Fe: Mn doped LN crystal is shown in figure 3.17.

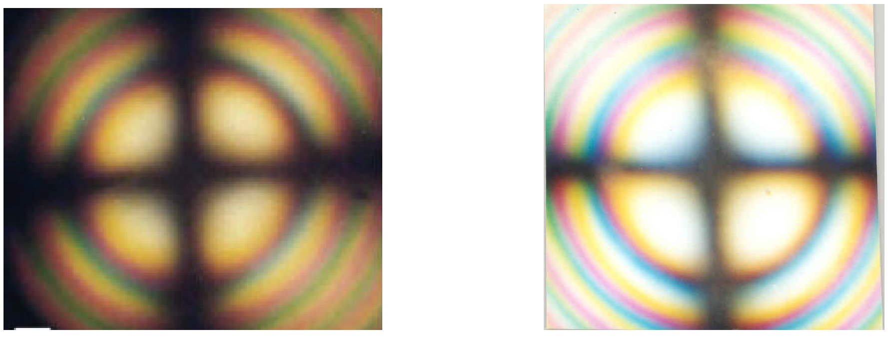

(a) (b)

Fig. 3.17 Conoscopic pattern of (a) Fe doped LN, and (b) Fe: Mn doped LN

Uniform conoscopic pattern shows the radial homogeneity of the crystal and the cross at the center determines that the optic axis of the crystal is perpendicular to the plate.

3.3.5 Etch pit study

Selective chemical etching is very good technique to know the origin and history of the dislocations in the crystals. Dissolution of a crystal takes place when it is placed in an environment which slowly removes atom or molecule from the crystal surface. This is achieved by the action of a solvent, for example, an acid on the crystal surface. The dissolution generally takes place at the local region of the crystal surface. This local selective dissolution is called etching. Etch pit studies were carried out on the grown crystal. The samples were cut in proper direction and polished. The selective etching technique was used to study the etch pits. Etchant used in the present work was one volume part HF and two volume parts HNO_3. The etching was carried out at 110 ^oC for 6-10 minutes. Figure 3.18 (a, b) shows the etch pits of Fe: $LiNbO_3$ and Fe:Mn:$LiNbO_3$ crystal when seen under optical microscope. Triangular shape of the etch pits shows three fold symmetry of the crystal. Measured dislocation density $3x10^3/cm^2$, which indicates that good quality crystals are grown.

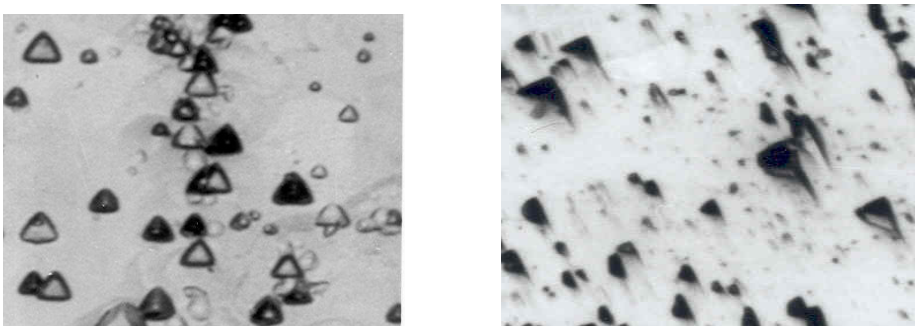

(a) **(b)**

Fig. 3.18 Etch pits of (a) Fe doped LN (b) Fe:Mn doped LN crystal (Magnification =300x)

3.4 Photorefractive study of as grown sample and proton exchanged sample

Photo refractive properties (e,g. Diffraction efficiency, Recording time and Erasing time) of as grown Fe: LN crystal and Fe: Mn: LN and proton exchanged sample were studied.

3.4.1 Preparation of proton exchanged sample

Several wafers of 1 mm thickness were cut along *X*- direction from the as-grown crystal. The wafers were polished using alumina powder. Polished wafers were used for proton exchange. The proton exchange was performed by immersing the wafers in a mixture of hydro fluoric acid (HF) and nitric acid (HNO_3) in the ratio 1:2 at a temp of 110 °C for different time duration (3 and 5 minutes). Hot plate was used to heat the setup. For boiling the mixture of acid, two beakers (one of glass and other of plastic) were used. Proton exchanged setup is shown in figure 3.19.

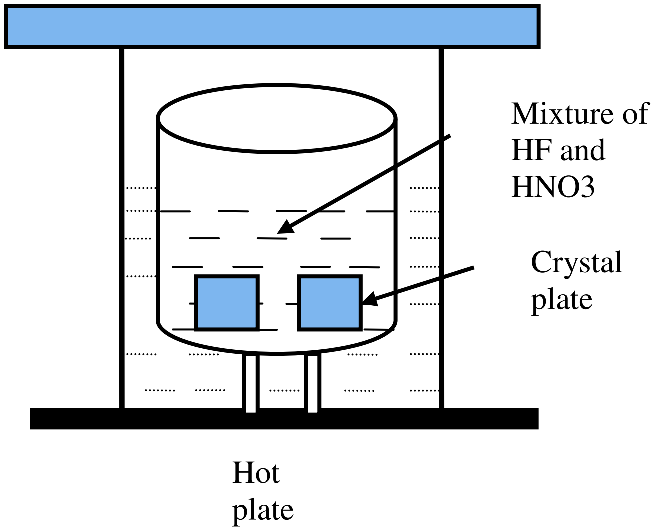

Fig. 3.19 Proton exchanged setup

3.4.2 Measurement of photorefractive properties of LN crystal by two wave coupling

Photorefractive properties of Fe doped LN and Fe: Mn doped LN crystals were measured using two-wave coupling phenomena. A He-Ne laser of power 25mW was used in the present study. The diameter of laser beam was approximately 1 mm. The photorefractive study is very sensitive to mechanical vibrations and fluctuations in the environmental parameters. In order to avoid variations in the measured properties due to the above factors, the experimental set up was placed on an optical table having pneumatic vibration isolation system. The optical set up is shown in figure 3.20. The X- cut sample was mounted in such a way that its *C*- axis was perpendicular to the angle bisector of the interfering beams and parallel to refractive index grating vector. This ensured utilization of the largest electro-optic coefficient i.e. r_{33} of the $LiNbO_3$ crystal.

The grating period can be calculated by using Bragg's law

$$2d \sin \theta = m\lambda.$$

Here λ is the wavelength of laser light, θ is the half angle of intersection between recording beams, m is an integer representing diffraction order and d is grating period or fringe spacing.

Due to interference pattern charge migration occurs from the brighter regions to nearby darker regions which form the refractive index grating. The grating so formed starts diffracting the incident signal beam, and the intensity of the diffracted beam increases, and finally saturates. The diffracted beam intensity is recorded at regular time intervals of 25 sec by blocking the reference beam for a fraction of a second. Once the saturation is achieved, the reference beam is blocked permanently, allowing only the signal beam to fall on the sample. Since no interference is possible now, the signal beam starts erasing the refractive index grating due to reverse migration of the charge carriers. As a result the intensity of the diffracted signal decreases gradually. The time taken for the diffracted light intensity to reach 1/e of its maximum is defined as the erasure time. The ray diagram of experimental set up for two-wave coupling experiment is shown in figure 3.21.

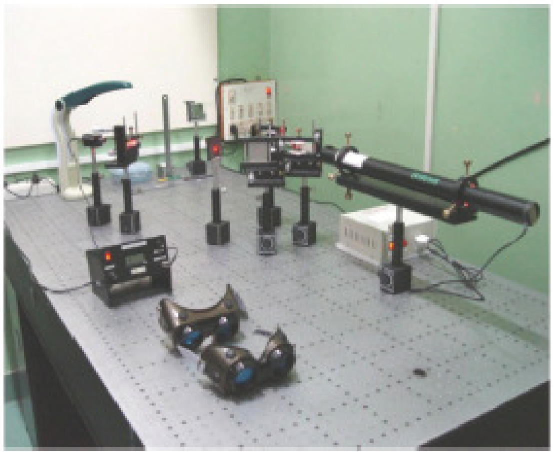

Fig. 3.20 Optical set up for photorefractive experiment

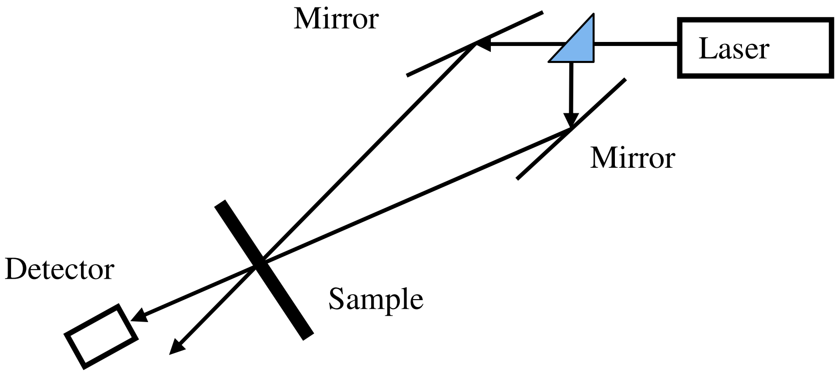

Fig. 3.21 Ray diagram for two wave coupling

Diffraction efficiency Vs time curve for Fe doped LN and Fe: Mn doped LN crystal is shown in figure 3.22 (a, b).

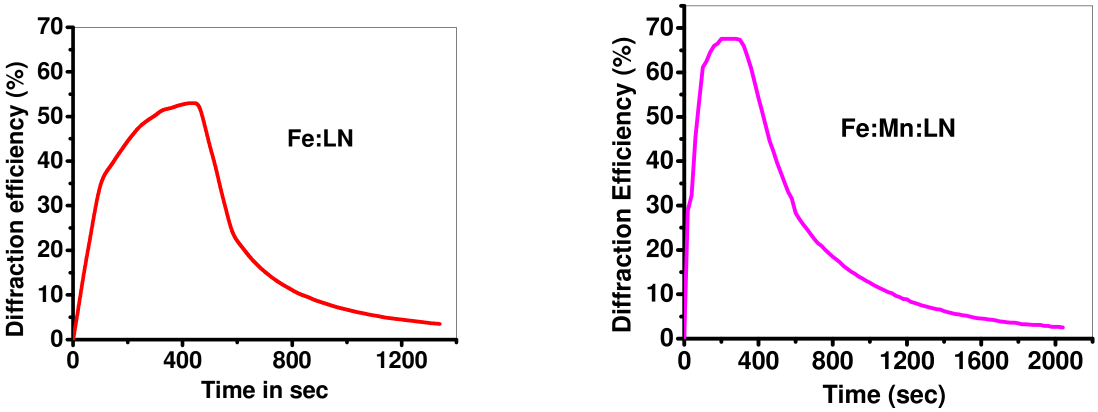

(a) **(b)**

Fig. 3.22 Diffraction efficiency for an as-grown (a) Fe: LN sample (b) Fe: Mn: LN sample

The proton exchange process in lithium niobate can be described broadly as depletion of lithium and the replacement of hydrogen in the crystal. This occurs when the crystal is immersed in a proton source, i.e. an acid. The proton exchange process can be represented as

$$LiNbO_3 + xH^+ \rightarrow Li_{1-x}\, H_xNbO_3 + xLi^+.$$

It results in an increase of extraordinary refractive index of the sample [30], which manifests itself in the formation of a strong refractive index grating. Strong refractive index grating may be due to increase of electro optic coefficient r_{33} of lithium niobate. When an electric field is applied to a crystal, the ionic constituents move to new locations determined by the field strength, the charge on the ions and the restoring force. The unequal restoring forces along three mutually perpendicular axes in the crystal lead to anisotropy in the optical properties of the medium. When an electric field is applied to such a crystal, in general, it causes a change in the anisotropy. These changes can be described in terms of the modification of the indicatrix by the field both in terms of the principle refractive indices of the medium and in the orientation of the indicatrix. In case of proton exchanged sample distortion increases for same field, hence electro optic coefficient increases. As a result, the diffraction efficiency (DE) of the proton exchanged samples increases as compared to the as-grown sample. Diffraction efficiency of Fe: LN sample before and after proton exchanged is shown in figure 3.23(a). Photorefractive properties were also studied for proton exchanged Fe: Mn: LN sample and compared with as grown sample. Diffraction efficiency of Fe: Mn: LN sample before and after proton exchanged is shown in figure 3.23(b).

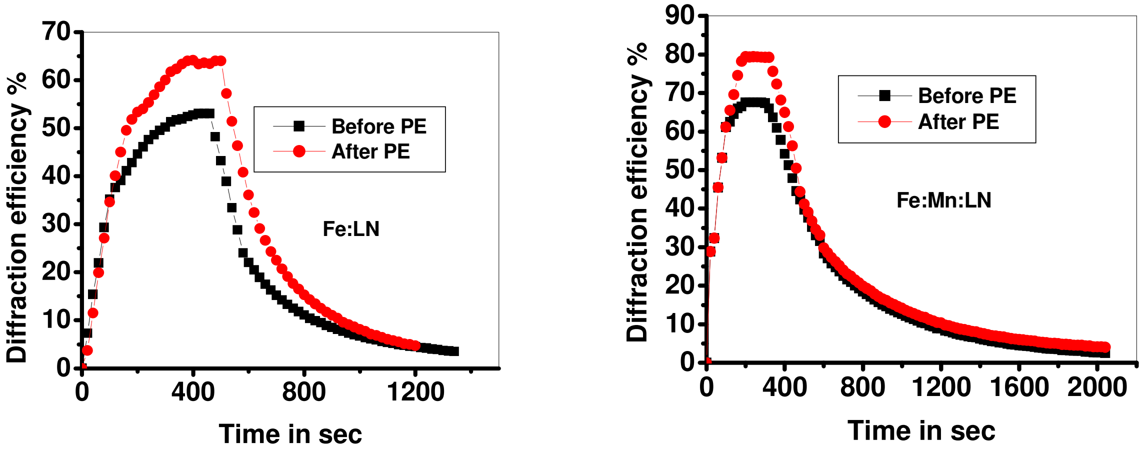

(a) (b)

Fig. 3.23 Diffraction efficiency of (a) Fe: LN sample (b) Fe: Mn: LN sample after and before proton exchange

From the figure 3.23 (a, b) recording time, erasing time and diffraction efficiency were calculated for crystal sample before and after proton exchange and given in table 3.1.

Table 3.1 Recording time, erasing time, and diffraction efficiency of crystal sample before and after proton exchange

		Recording time	Erasing time	Diffraction efficiency
Fe: LN	Before PE	96 sec	178 sec	54%
	After PE	126 sec	197 sec	66%
Fe: Mn: LN	Before PE	53 sec	300 sec	68%
	After PE	54 sec	310 sec	79%

Therefore proton exchange technique is useful for enhancing photorefractive properties of the crystal.

References:

1. T. Tsuboi, M. Grinberg, S. M. Kaczmarek, J. Alloys. Compd. 341 (2002) 333.

2. Y. Kurz, E. Krätzig, W. Kenne, H. Engelmann, U. Gonser, B. Dischler, A. Ränber Appl. Phys. 12 (1977) 355.

3. K. Buse, F. Jermann, E. Krätzig, Appl. Phys. A. 58 (1994)191.

4. J. F. Heanue, M. C. Bashaw, and L. Hesselink, Science 265 (1994) 749.

5. G. A. Rakuljic, V. Leyva, and A. Yariv, Opt. Lett. 17 (1992) 1471.

6. F. H. Mok, Opt. Lett. 18 (1993) 915.

7. Y. Furukawa, M. Sato, M. C. Bashaw, M. M. Fejer, N. Iyi, and K. Kitamura, Jpn. J. Appl. Phys. 35 (1995) 2740.

8. K. K. Wong (editor), Properties of Lithium Niobate, INSPEC publication, London, 2002 .

9. T. Volk, M. Wohlecke, Lithium niobate, Defects, Photo refraction and ferroelectric switching, Springer, 2009.

10. H. M. O' Bryan, P. K.Gallagher, C. D. Brandle, J. Am. Ceram. Soc. (USA) 68 (1985) 493.

11. S. C. Abrahams, P. Marsh, Acta Crystallogr. B (Denmark) 42 (1986) 61.

12. L. O. Savaasand, M. Eriksurd, G. Nakken and A. P. Grande, J. Cryst. Growth 22 (1974) 230.

13. L. Arizmendi, Phys. Stat. Sol.(a) 201 (2004) 253.

14. G. Malvichko, V. Grachev, E Kokanyam, Ferroelectrics 258 (2001) 131.

15. G. Müller, Cryst. Res. Technol. 42 (2007) 1150.

16. D. Psaltis and F. Mok, Sci. Am. 273 (1995)70.

17. I. McMichael, W. Christian, D. Pletcher, T. Y. Chang, and J. H. Hong, Appl. Opt. 35, (1996) 2375.

18. R. M. Shelby, J. A. Hoffnagle, G. W. Burr, C. M. Jefferson, M. P. Bernal, H. Coufal, R. K. Grygier, H. Gu¨nther, R. M. Macfarlane, and G. T. Sincerbox, Opt. Lett. 22 (1997)1509.

19. J. J. P. Drolet, E. Chuang, G. Barbastathis, and D. Psaltis, Opt. Lett. 22 (1997) 552.

20. G. E. Peterson, A. M. Glass and T. J. Negran, Appl.Phys.Lett. 19 (1971)130.

21. G. E. Peterson, A. M. Glass, A. Carnevale and P. M. Bridenbaugh, J.Am.Ceramic

Soc., 56 (1973) 278.

22. P. L. Shah, T. A. Rabson, F. K. Tittel and T. K. Gaylord, Appl. Phys. Lett. 24 (1974)130.

23. W. Phillips and D. L. Steabler, J. Elec. Mat. 3 (1974) 601.

24. D. L. Staebler and W. Phillips, Appl. Opt. 13 (1974) 788.

25. K. Buse, A. Adibi, D. Psaltis, Nature 393(1998) 665.

26. A. Adibi, K. Buse, D. Psaltis, J. Opt. A: Pure Appl. Opt. **1** (1999) 237–238.

27. K. A. Jackson, Progress in Solid State Chemistry 4 (1967) 53.

28. D. T. J. Hurle, G. C. Joyce, M. Ghassempoory, A.B. Chrowley, E.J. Stern, J. Cryst. Growth 100 (1990)11.

29. R. V. A. Murthy, K. S. Bartwal, K. Lal, Mat. Sci. & Engg. B 1993, 18, L4-L6.

30. J. L. Jackel**,** C. E. Rice and J. J. Veselka, Appl. Phys. Lett. 41 (1982) 607.

Chapter 4

Growth and Characterization of Doped and Undoped Lithium Tetraborate Crystals

4.1 Introduction

The lithium tetraborate, $Li_2B_4O_7$ (LTB) is an important material for generation of 4th and 5th harmonics of Nd: YAG laser and frequency conversion devices for high power UV solid-state laser [1]. It is transparent up to 165 nm in UV region. This is very attractive material for surface acoustic wave substrate due to its high electro mechanical coupling coefficient factor k^2 and low temperature coefficient of frequency [2]. The physical, chemical and structural properties of lithium tetraborate (LTB), play a major role on its potential as a thermoluminescence (TL) dosimeter. In current days investigation on lithium tetraborate single crystals has been greatly increased due to its potential application in radiation dosimetry. Tissue equivalence is a much desired property for thermoluminescent dosimeters for estimation of absorbed dose in tissues. Lithium tetraborate based TL dosimeters are best with an effective atomic number of 7.3 which is very close to that of soft biological tissue (Z_{eff}= 7.42) [3, 4, 5]. In thermoluminescence dosimetry, LTB is an ideal material when it is doped, to enhance the thermoluminescent characteristics. Further, in addition to X-ray and gamma-ray radiation, LTB based dosimeters are also sensitive to neutron radiation.

4.1.1 Structure of lithium tetraborate (LTB)

LTB crystal belongs to tetragonal system having 4mm point group symmetry and space group $I4_1cd$ with lattice parameters a = b = 9.479 Å, c = 10.286 Å. One unit cell of LTB contains 8 formula units. The main crystal motif of LTB are boron oxygen complexes (B_4O_9) consisting of two planer trigonal BO_3 and two planer tetrahedral BO_4 (fig. 4.1). The lithium atoms are localized at interstices [6]. The space group $I4_1cd$ generates total of 104 atoms [7] in one unit cell. All B1 belong to triangles (coordinated by O1, O2 and O3) and all B2 are tetrahedrally coordinated with oxygen atoms.

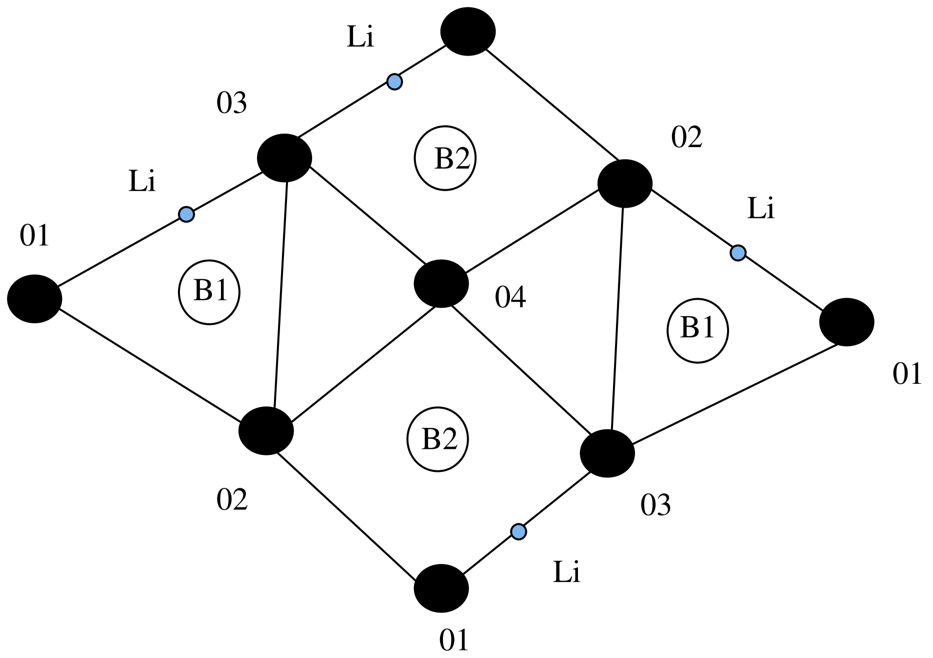

Fig. 4.1 Main crystal motif of lithium tetraborate consisting of two basic elements

There are two identical planar triangular (B1+O1+O2+O3) and two identical tetrahedral (B2+O1+O2+O3+O4) groups [8]. It is known that crystal generally possesses imperfection in their structure and that is responsible for unusual property of the material. In the case of LTB, the interaction of lithium oxide and boron oxide causes attachment of an additional oxygen atom to the boron–oxygen triangle to produce boron-oxygen tetrahedron. This boron-oxygen tetrahedron has excessive negative charge compensated by lithium cation located in the vicinity of the tetrahedron. In the absence of the lithium atom, this complex acts as a negative point defect forming hole traps that balance the negative charge in the normal condition [9, 10]. Oxygen vacancies in the structure produce positively charged point defect which may trap electron. The lithium ions stabilize the boron-oxygen framework by distributing in helicoidal voids along the z-axis. Li sites and space in helicoidal voids are regarded usually as the only possible places to be occupied by various impurities in $Li_2B_4O_7$. This comes from the comparison of ionic radii of different impurities with the sizes of possible sites in $Li_2B_4O_7$ lattice.

4.1.2 Material potential

Lithium tetraborate possesses a combination of physical properties which are important for different scientific and technological application. It is an important material for nonlinear optics. Mn and Cu activated lithium tetraborate crystals are widely used as personnel dosimeter. This material has different advantages compare to the other thermoluminescence dosimeters. LTB has wide transparency range, high radiation hardness and high mechanical strength. As the effective atomic number of lithium tetraborate ($Z_{eff} = 7.42$) is very close to that of soft biological tissue, so this material can be used as a tissue equivalent material. LTB is also used as an substrate of surface acoustic wave (SAW) and bulk acoustic wave (BAW) devices [11]. LTB single crystal has high transparency from vacuum ultraviolet (VUV) to far infrared (IR) region. It has appropriate nonlinear optical properties and they are promising acousto electronic material [12]. It has high neutron capturing capacity due to large neutron capture cross section of ^{6}Li and ^{10}B (Lithium - 960 barn and Boron – 3840 barn) [13] and is a potential material for neutron detector.

Single crystals are essential requirement for some special application where presences of grain boundaries are not desirable. In case of TLD, polycrystalline powder pallets are being used for measuring radiation dose. During reading the TLD in analyzer, light emitting from inner part of the TLD pallet gets scattered at grain boundaries. Amount of light coming out from the sample is very less and hence detected light intensity by PMT is also less. To avoid this problem undoped and doped LTB single crystals were grown. Growth of a good quality crystal is not an easy job. During crystal growth crystal may cracks and core or twinning may form. Post growth cooling is also very crucial parameter for LTB crystal. To avoid cracking proper cooling rate is required. Various growth parameters such as pulling rate, rotation rate, axial temperature gradient, post growth cooling rate, etc. were optimized to get transparent, appreciable size, crack free crystal.

4.2 Growth of undoped and doped lithium tetraborate crystal

4.2.1 Material synthesis

High purity oxides in the ratio 67.9 mole % of B_2O_3 and 32.1 mole% Li_2CO_3 were taken for the preparation of charge. Chemicals were then mixed initially through mortar pestle by hand and finally mixed through ball milling for 5 hr. The excess amount of B_2O_3 over stoichiometric composition was taken because of its high vapor pressure [14]. Special care has been taken during weighing of charge because the chemicals are hygroscopic in nature. Homogeneously mixed powder was filled in the platinum crucible and was kept in the furnace at 400 °C for 10 hrs. Next the charge from crucible was taken out and was remixed through mortar pestle. In next step the powders were heated up to 750°C from room temperature at the heating rate of 100 °C per hour. Dwell time was 10 hr. Step wise heating is applied to avoid frothing. To grow Mn and Cu doped crystal accurate amount of dopant added during charge synthesis. Here 0.2 mole % MnO_2 and 0.2 mole % CuO was added for the growth of doped crystal. Finally the phase of solid state reacted powder was checked through XRD.

4.2.2 Crystal growth experiment

Crystal growth was carried out using the Platinum crucible of 50 mm diameter and 50 mm height. Initially solid state reacted powder was taken in platinum crucible and melted. Temperature of the crucible increased to 30-40°C higher than the melting point and kept for 1 hr for homogenizing the melt. Then the melt is cooled slowly up to melting point. During cooling the melt, the rate of cooling should not be very fast to avoid glass formation. Major difficulties come during the growth of lithium tetraborate crystals are cracks, formation of core, defect region consisting largely of opaque inclusions and twinning [15, 16]. Crystals generally cracks during post growth cooling due to anisotropy of thermal expansion coefficient. The coexistence of BO_4 tetrahedral and BO_3 triangles in the framework structure of $Li_2B_4O_7$ makes the crystal prone to cracking [17].

In our experiment we have kept post growth cooling rate 40°C/hr. Seed crystal of dimension 2 X 2 X 10 mm^3 was used for seeding. Seed was properly tied in ceramic rod with platinum wire and slowly dipped into the melt to avoid thermal shock. The small portion of the seed was then slightly pulled out manually to get inclusion free crystal. Initial rotation rate of the seed rod was 8 rpm and was reduced to 6 rpm afterward. Small rotation rate reduces thermal convection and hence reduces temperature fluctuation. Pulling rate for this crystal is very less ~0.3 mm/hr. Resistive heating furnace with suitable axial temperature gradient was used for growth. Eurotherm temperature controller was used to control the temperature of the furnace. Crystal growth set up is shown in figure 4.2.

Fig. 4.2 The Czochralski growth system used for LTB growth

Crystals were grown with different temperature gradient near the melt and solid interface. First run was performed in low axial temperature gradient and second run was performed in high axial temperature gradient. Axial temperature gradient of the furnace is shown in figure 4.3, here upward distance taken in cm.

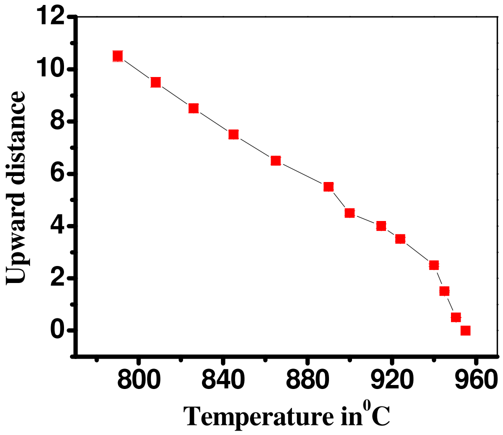

Fig. 4.3 Axial temperature gradient of the furnace

Crystals grown in low temperature gradients are shown in figure 4.4

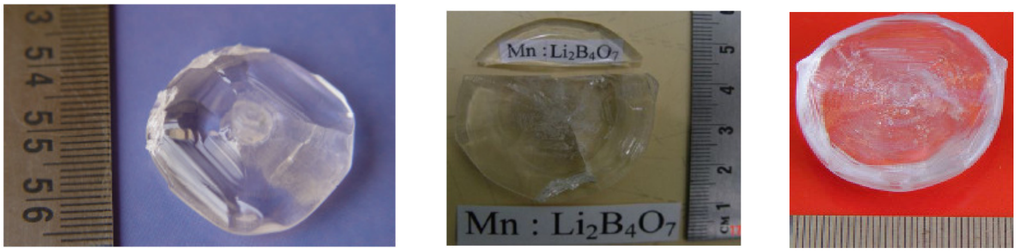

(a) (b) c)

Fig. 4.4 Photograph of grown crystals (a) undoped LTB (b) Mn doped LTB (c) Cu doped LTB

It has been observed that in low axial temperature gradient (16°C/cm), grown crystals were thin. It was difficult to increase the length of the crystal. To increase the length of the crystal axial temperature gradient was increased to 20 °C/cm by changing the crucible position. In modified gradient good quality crack free crystals with larger length obtained. Grown crystals with modified axial gradient are shown in figure 4.5.

Fig. 4.5 Photographs of grown LTB crystals with modified gradient

4.3 Characterizations of grown crystals

4.3.1 XRD and HRXRD study

Crystalline powder obtained by crushing a piece of grown crystal was tested by powder X-ray diffraction (XRD) for phase identification. Figure 4.6 (a, b, c) shows the powder XRD pattern of the undoped, Mn doped and Cu doped grown crystal. It was observed that XRD peaks are matching well with the known single phase for LTB.

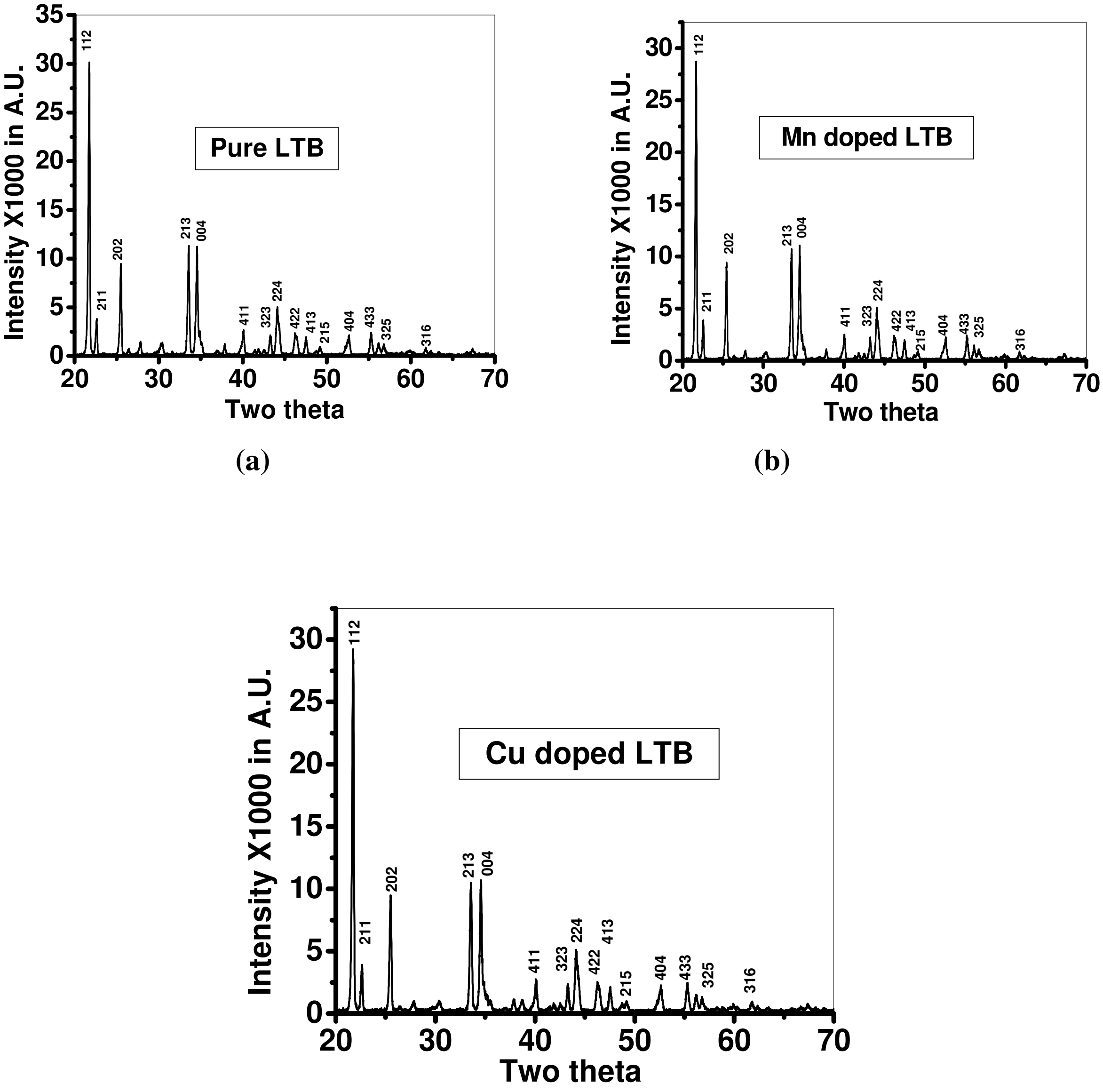

(a)

(b)

(c)

Fig. 4.6 XRD pattern of (a) undoped LTB, (b) Mn doped LTB and (c) Cu doped LTB

Crystalline perfection of those as grown crystals were examined by diffraction curves (DCs) or rocking curves. Figure 4.7 shows the HRXRD of LTB crystal plate along 004 planes. A well-collimated Mo Kα_1 beam diffracted from a third plane monochromator crystal of Si (111) in the dispersive symmetrical Bragg geometry (+, -, -) configuration is used for this experiment. This arrangement particularly improves the spectral purity of the Kα_1 beam. The specimen crystal is aligned in the (+, -, -, +) symmetrical Bragg geometry. The rotation given by the main turntable to the specimen around a vertical axis (which changes the glancing angle θ) is produced with the help of a micrometer, which moves a long radial arm of the diffractometer. The micrometer is driven by a stepper motor, which is controlled by a microprocessor control unit (Philips, PW 1710). The specimen can be rotated in steps of 0.5" The diffracted X-ray intensity is measured by a scintillation counter. Its output is measured by the counting system incorporated in the microprocessor control unit. The detector is mounted with its axis along a radial arm of the turntable. The measured tilt angle is 66-arc sec. The deconvolution of the DC curve in figure 4.7 indicates that the experimental DC consists of two curves (dotted line) with an angular separation of 8-10 arc sec. The FWHM recorded of the main peak is found to be 38 arc sec while the peak intensity is 130 c/sec, whereas for the secondary peak the FWHM is about 28 arc sec. This indicates the presence of grain boundary in the crystals with the tilt orientation of about 8-10 arc sec. The overall FWHM can be calculated as 66 arc sec. This value for FWHM suggests that the overall crystalline perfection of the grown crystals is quite good for many applications.

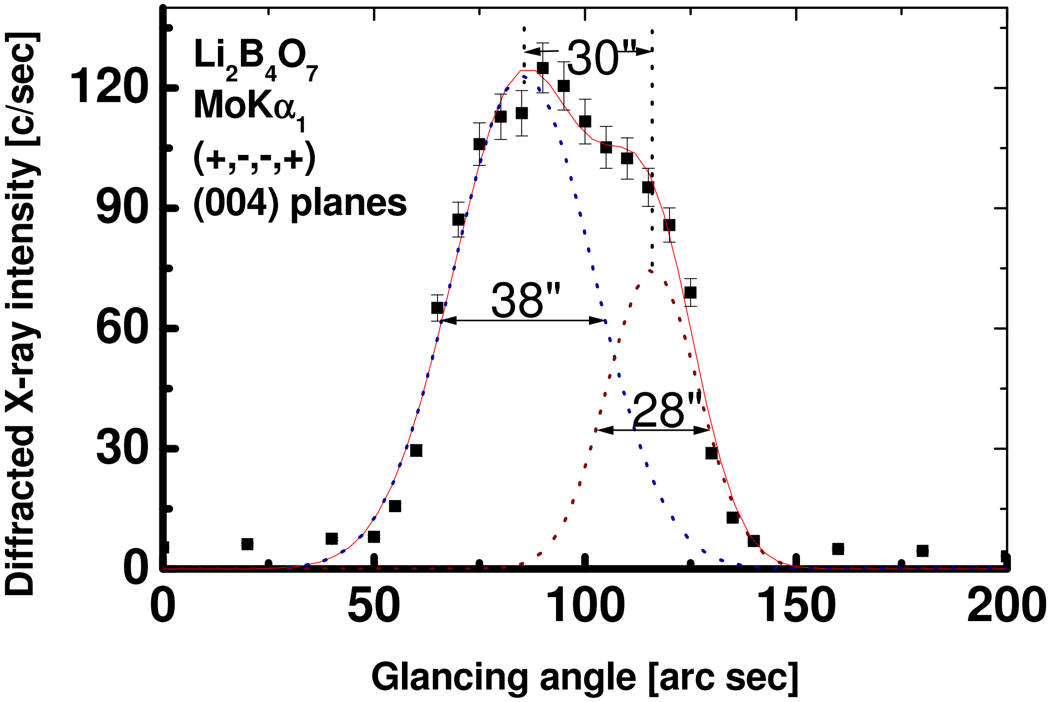

Fig. 4.7 High Resolution X-ray diffraction curves recorded for (004) planes of $Li_2B_4O_7$ crystal

4.3.2 Etching study

In borates primary mechanism for generating dislocation is nucleation at inclusions. The distribution of inclusion in crystal depends on the growth condition (convection, shape of growth interface etc). Due to the high viscosity of melt in borates, bubbles and voids are usually most heavily concentrated at the central part of the crystal boules. In this region scattering and absorption of laser beam occur, which limits the device performance and decreases the damage threshold of the crystal. Sample of dimension 10×10×1 mm^3 was cut and polished properly from an as grown crystal for etching study. Concentrated hydrofluoric acid (HF) was used as etchant. The etching was performed at room temperature with varying time. The etch pits on the sample was observed by optical microscope. Fig. 4.8 (a, b, c) shows the typical pyramidal etch pit patterns on LTB plate for different etching time. The etch pit density is direct measure of the dislocation density in the crystals. We have measured the dislocation density from these patterns. The measured dislocation density was 3×10^3 /cm^2. This value of the dislocation density is reasonably low, indicating that the grown crystals are of good quality.

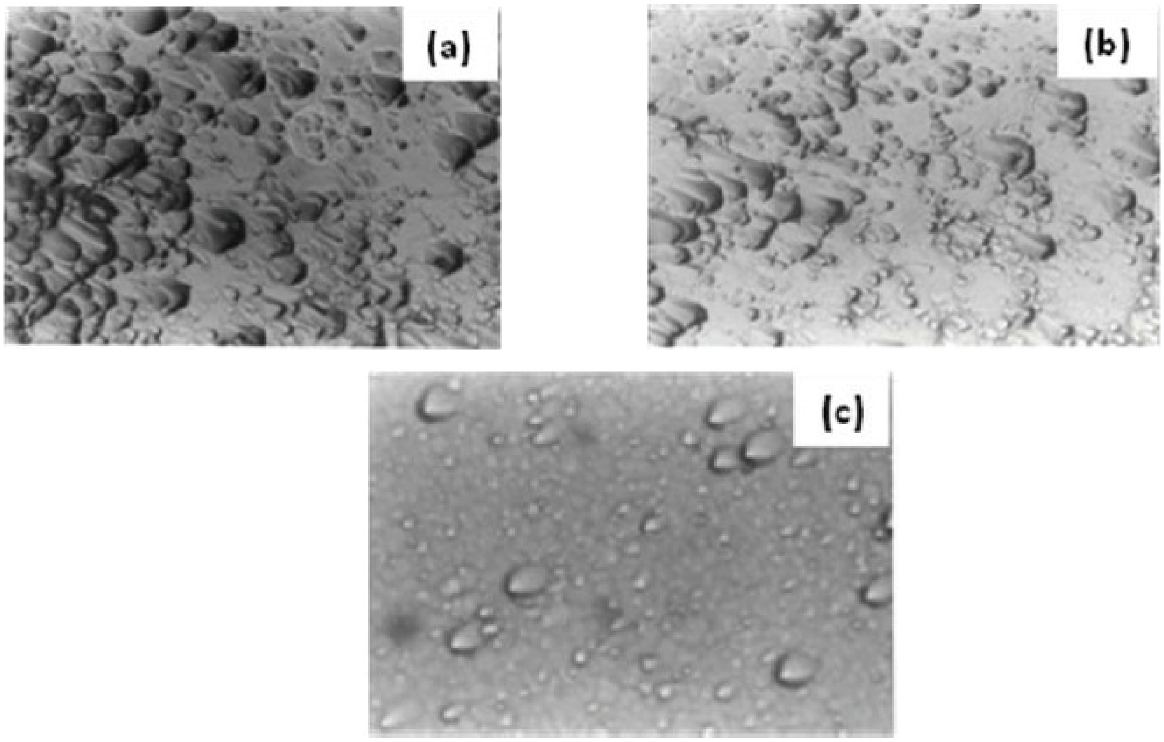

Fig. 4.8 Etch pits on LTB plate (a) etched for 1 min., (b) etched for 40 sec, and (c) etched for 20 sec. Magnification for all (300x)

4.3.3 UV-VIS transmission spectra study

Transmission spectra of the crystal wafers were recorded using UV-VIS spectro-photometer (Cary-50). The transmission of the crystal was observed more than 80 % over its transparent spectral range. Figure 4.9 (a, b, c) shows the transmission spectra of the undoped LTB crystals, Mn doped LTB crystal and Cu doped LTB crystal. Crystal plates cut at various point along the axis shows no variation in transmission spectra. This proves that there is no axial variation of homogeneity in the crystal. Transmission was also taken at various points in a straight line on a plate, which shows no variation in transmission. This indicates that there is no radial variation of homogeneity in the crystal.

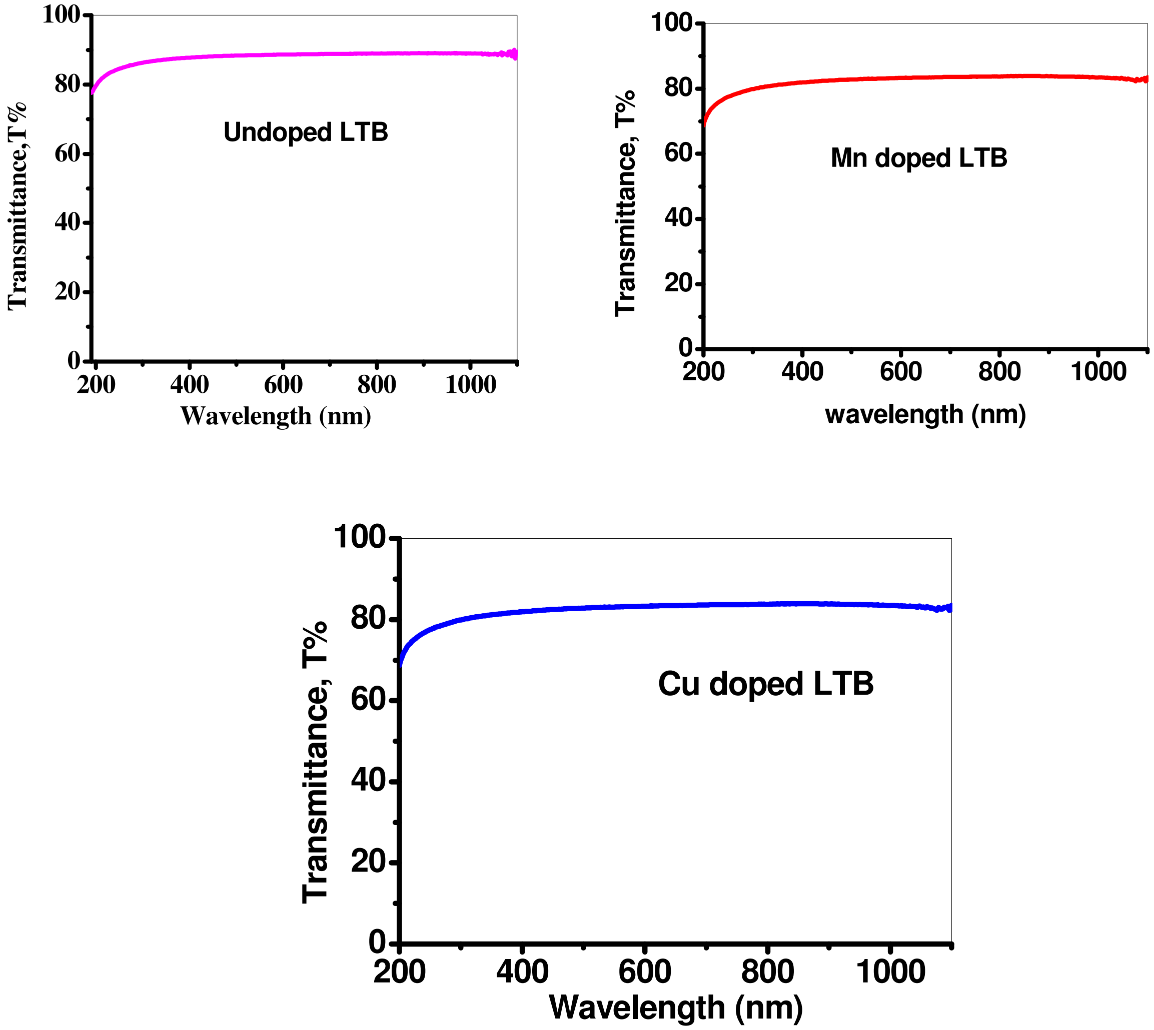

Fig. 4.9 Transmission spectra of (a) undoped LTB crystal (b) Mn doped LTB crystal (c) Cu doped LTB crystal

4.3.4 Birefringence interferometry

Birefringence is the decomposition of a ray of light in to two rays when passes through the anisotropic material. In birefringence interferometry polarized He-Ne laser beam is made to incident on the polished crystal sample. On passing through the crystal the light ray decomposes in to two ray of different polarization (mutually perpendicular). These two rays of different polarization then pass through the analyzer. Now the component of electric vector parallel to the analyzer will pass through and they will interfere. The birefringence interferometry set up is discussed in chapter 3. The interferogram of undoped LTB is shown in figure 4.10. The parallelism and straightness of the fringe indicates the refractive index homogeneity of the crystal.

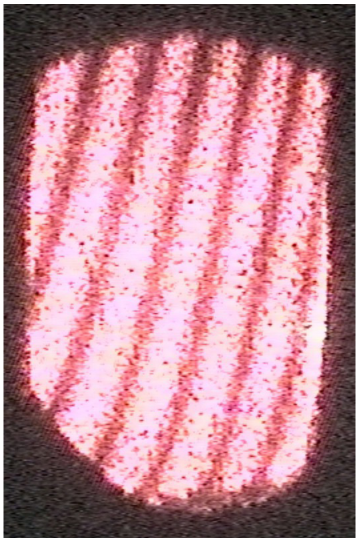

Fig. 4.10 Birefringence interferogram for Undoped LTB crystal

4.3.5 Conoscopic study

In order to determine optic axis and study optical homogeneity of the grown crystals conoscopic study was performed. Details mechanism of conoscopic pattern is discussed in chapter 3. Olympus polarizing microscope was used for the study. Sample of dimension 10×10×2 mm^3 were cut and polished properly by alumina powder of particle size 0.03 micron for the study. Figure 4.11 shows the conoscopy pattern of LTB crystal.

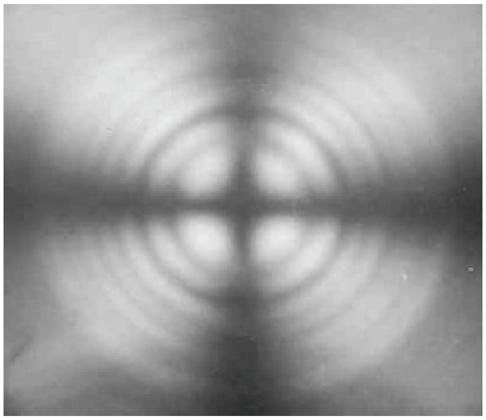

(a)

Fig. 4.11 Conoscopy pattern of undoped LTB crystal

The symmetrical fringe pattern is direct measure of good optical homogeneity of the crystal. From the picture it has been confirmed that optic axis is perpendicular to the crystal plate.

4.3.6 Hardness measurement

Crystal hardness is defined as the resistance offered by it to external mechanical action. In general hardness depends on the plastic deformation, which is related to the creation and motion of dislocation. The Vickers hardness test method consists of indenting the test material with a diamond indenter in the form of right pyramid with a square base with an angle of 136° between opposite faces subjected to a load. In static indentation test, pyramid is forced into the crystal surface and load per unit area of impression is taken as the measure of hardness. The full load is normally applied for 10 to 15 seconds. The two diagonals of the indentation imprinted on the surface of the material after removal of the load are measured using a microscope and there average is calculated. Fig. 4.12 shows the indentation mark on the crystal face at load of 50g (0.49 N) for 10 seconds. The area of the slopping surface of indentation is calculated. The Vickers hardness is the quotient obtained by dividing the Kgf load by the area of indentation:

$$HV = 2F \sin 68^\circ / d^2$$

Measured value of HV of our crystal was found about ~764 HV. This value is quite high and suggests that the surface and structural quality of grown crystal is very good.

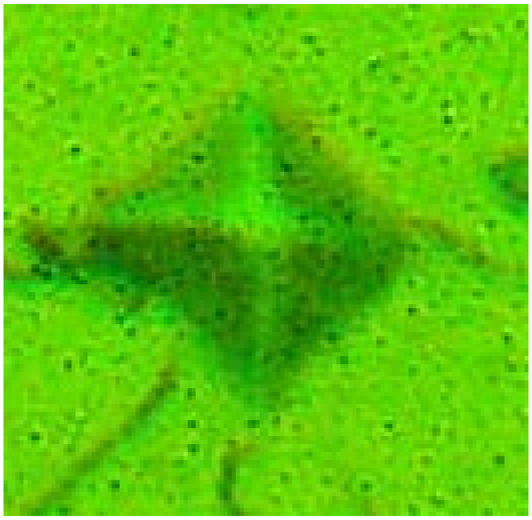

Fig. 4.12 Indentation mark on face of the LTB crystal plate

References:

1. T. Sugawara, R. Komatsu, S. Uda, J. Cryst. Growth 193 (1998) 364.

2. R. W. Whatmore, N. M. Shorrocks, C. O`Hara, F. W. Anger and I. W. Young, Electron. lett. 17 (1981)11.

3. A. S. Pradhan, Radiat. Prot. Dosim.1 (1981)153.

4. C. Furetta, M. Prokic, R. Salamon, V. Prokic, and G. Kitis, Nucl. Instrum. Methods, 456 (2000) 411.

5. A. T. Ege, E. Ekdal, T. Karali, N. Can, and N. Prokic, Meas. Sci. Technol.18 (2007) 889.

6. V. S. Gorelik, A. V. Vdovin, and V. N. Moiseenko, J. Russ. Laser. Res. 24 (2003) 553.

7. A. Yu. Kuznetsov, A. V. Kruzhalov, I. N. Ogorodnikov, A. B. Sobolev, L. I. Isaenko, Physics of the solid 41 (1) (1999) 48.

8. M. Kerikmae, M. Danilkin, A. Lust, V. Nagirnyi, L. Pung, A. Ratas, I. Romet, V. Seeman, Radiat. Meas. 56 (2013)147.

9. E. Pekpak, A. Yilmaz, and G. Ozbayoglu, The Open Mineral Processing Journal, 3 (2010) 14.

10. M. S. Rasheedy, Thermochim. Acta, 429 (2005) 143.

11. N. Tsutsui, Y. Ino, K. Imai, N. Senguttuvan, M. Ishii, J. Cryst. Growth, 211 (2000) 271.

12. B. V. Padlyak, V. T. Adamiv, Ya. V. Burak, M. Kolcun, Physica B 412 (2013) 79.

13. K. Sangeeta, K. Chennakesavulu, D. G. Desai, S. C. Sabharawal, M. Alex,

D. Ghodgaonkar, Nucl. Instrum. Methods in physics research A 571 (2007) 699.

14. D. Podgorska, S. M. Kaczamarek, W. Drozdowski, M. Brekowski and A. Worsztynowicz, Acta Physica A, Vol 107 (2005) 507.

15. D. S. Robertson, I. M. Young, J. Mat Sci. 17 (1982) 1729.

16. Ya. V. Burak, J. Cryst. Growth 186 (1998) 302.

17. J. Xu, S. Fan, B. Lu, J. Cryst. Growth 264 (2004) 260.

Chapter 5

Thermoluminescence Studies on Irradiated Doped and Undoped Lithium Tetraborate Single crystals, Polycrystals and Glass

5.1 Introduction

Thermally stimulated luminescence (TSL) is the phenomenon of light emission during heating a previously irradiated material with uniform heating rate. When a material is exposed to ionizing radiation like; alpha, beta, gamma and X-rays or UV-rays, a certain percentage of the liberated charge carriers (electron and holes) may be trapped at certain imperfections in the lattice, which are called traps. If these traps are deep enough, the charge carriers remain trapped for a long time before they are released by sufficient stimulation. This stimulation can be achieved by thermal energy. These trapped charge carriers excited to the conduction band and then recombine with the recombination center located just above the valence band. This recombination is associated with the emission of light. This form of emission of light is called thermoluminescence (TL). The luminescence from the material depends on

i) The amount and nature of impurity,
ii) Thermal history,
iii) Amount of radiation absorbed and
iv) Defect pattern present in the material.

5.1.1 Mathematical description

There are two delocalized bands, conduction band (CB), and valence band (VB). Between these two bands, two localized levels are present, one behaves as a recombination center, and the other behave as a trap center. The activation energy or trap depth (E) was defined as the difference between the trap level and the bottom of the CB. After absorbing sufficient energy ($h\nu > E_g$), electron get excited from valance band to conduction band. The free carriers may either recombine with each other, become trapped or remain free in their respective delocalized bands. During heating, when the trapped electron absorbs enough energy, it is released back into the conduction band, from where recombination takes place.

During recombination emission of light occurs. Depending on the trapping and re-trapping mechanism there are two types of kinetics in TL material, first order kinetics and second order kinetics.

A. First order kinetics

The most simplified mathematical model which describes the above process was first given by Randall and Wilkins. Consider a material containing defects which give rise to a single electron trap level, having trap depth or activation energy E containing n electrons at time t and at temperature T (in Kelvin). The energy distribution of electrons within the trap will be described by Boltzmann distribution, and hence the probability p of release of an electron from the trap is given by the Arrhenius equation,

$$P = s\exp\left(\frac{-E}{kT}\right) \qquad \text{--------------------------------5.1.}$$

Where, k is Boltzmann's constant and **s** is a frequency factor or attempt to escape factor having value in the order of the lattice vibration frequency, namely 10^{12}-$10^{14}s^{-1}$. The rate of release of electrons from the trap is

$$-\left(\frac{dn}{dt}\right) = ns\exp\left(\frac{-E}{kT}\right) \text{--------------------------------5.2.}$$

Randall and Wilkins assumed that all electrons released from traps undergo TSL transitions, i.e., there is no re-trapping. This gives us the concept that the rate of release is proportional to the trapped charge concentration, and thus termed as first-order kinetics. The intensity of the TSL glow, I (t) depends on the rate of release of electrons from traps and their rate of arrival at luminescence centers:

$$I(t) = -C\left(\frac{dn}{dt}\right) = Cns\exp\left(\frac{-E}{kT}\right) \qquad \text{-------------------5.3.}$$

Where C is a constant related to luminescence efficiency.

Equation (5.2) becomes,

$$\left(\frac{dn}{dT}\right) = -\left(\frac{1}{\beta}\right)ns\exp\left(\frac{-E}{kT}\right) \qquad \text{----------------------------5.4.}$$

Here, $\beta = \left(\frac{dT}{dt}\right)$.

On integration, we get

$$\ln\left(\frac{n}{n_0}\right)=-\int\left(\frac{1}{\beta}\right)s\exp\left(\frac{-E}{kT}\right)dT\text{ , --------------------------------5.5.}$$

Here n_0 is the number of electrons present in the trap at time t_0 and temperature T_0.

Finally, substituting for n in equation (5.3),

$$I(T)=\frac{n_0 s}{\beta}\exp\left(\frac{-E}{kT}\right)\exp\left\{\left(\frac{-s}{\beta}\right)\int_{T_0}^{T}\exp\left(\frac{-E}{kT}\right)dT\right\}\text{----------5.6.}$$

This is the expression for the glow intensity I for electrons trap at a single trapping level E. It is a Randall and Wilkins expression for first order kinetics. The plot of I against T is termed as glow curve. The glow curve has a characteristics asymmetric shape being wider on the low temperature side than on the high temperature side.

B. Second order kinetics

A modification of this view was presented by Garlick and Gibson, who used this same one-trap, one-recombination center model but who included the concept of significant retraping of the released charges. This gives us the concept that the rate of release is proportional to the square of the trapped charge concentration, and hence it is called second-order kinetics. Here we have

$$-\left(\frac{dn}{dt}\right)=-n^2 s'\exp\left(\frac{-E}{kT}\right)\text{-----------------------------------5.7.}$$

Here, s’ = s/N, and N is the total concentration of available electron traps. This leads to the Garlick-Gibson equation for TSL under second-order kinetics,

$$I(T)=\frac{n_0^2 s'\exp\left(\frac{-E}{kT}\right)}{\left[1+\frac{n_0 s'}{\beta}\int_{T_0}^{T}\exp\left(\frac{-E}{kT}\right)dT\right]^2}\text{----------------------------5.8.}$$

The main feature of this equations is that the glow curve is nearly symmetric, with the high temperature half of the curve slightly broader than the low temperature half. This can be understood from the consideration of the fact that in the second order reaction, significant concentrations of released electrons are retrapped before they recombine.

5.1.2 Kinetic parameters of TL material

There are three kinetic parameters for a given TL material. These are order of kinetics, activation energy and frequency factor.

A. Order of kinetics

Order of kinetic implies how the rate of change of charge carrier from trap center depends on the number of trapped electron. If the rate of change of charge carrier is proportional to square of the trapped electron than it is second order and if it is linearly proportional to the trapped electron then it is first order. From the glow curve order of kinetics can be determined by observing the shape of glow curve. A general TL glow curve is shown in figure 5.1.

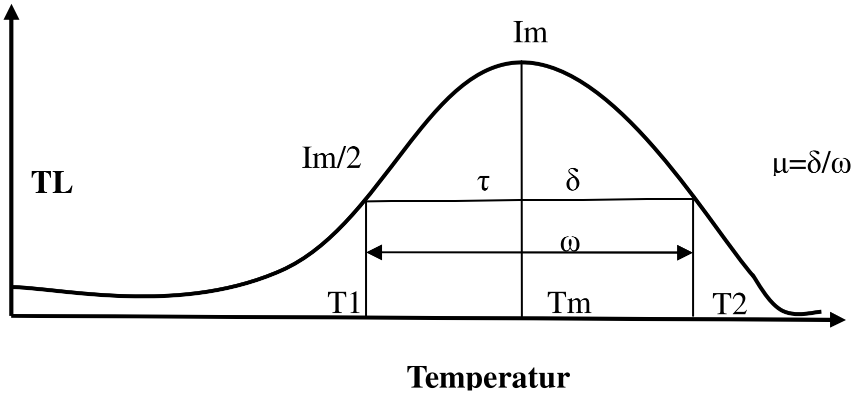

Fig. 5.1 General TL glow curve

Here, T_m is the peak temperature at the maximum. T_1 and T_2 are temperatures on either side of T_m corresponding to half intensity.

$\tau = T_m - T_1$ is the half-width at the low temperature side of the peak.

$\delta = T_2 - T_m$ is the half-width at the high temperature side of the peak.

$\omega = T_2 - T_1$ is the total half – width.

$\mu = \delta / \omega$ is so-called geometrical shape of symmetry factor.

A first order peak exhibits a geometrical factor $\mu=0.42$. The position of maximum TL intensity does not change for different radiation doses. A second order peak exhibits a geometrical factor $\mu=0.52$. The position of TL intensity shifts towards higher temperature values for low doses.

B. Activation energy

Activation energy is the energy required to excite an electron from trap center to conduction band. The half life of a trap at constant temperature is defined as the time for which the number of trapped electron falls to half of their initial value. The half life for first order process is expressed by

$$t_{1/2} = \ln 2/s \exp(-E/kT) = 0.693/ s \exp(-E/kT).$$

The half life at a constant temperature and given value of frequency factor increases as the activation energy increases. This is a logical consequence of the fact that the higher the activation energy, the higher the stability of the trap.

C. Frequency factor

It is the attempt to escape frequency. Considering a trap as a potential well, the frequency factor represents the product of the number of time an electron hits the wall and the wall reflection coefficient. The order of magnitude of the frequency factor should be similar to the vibrational frequency of the lattice. Its value is around 10^8 to 10^{12} per sec. In some cases frequency factor depends on temperature. All these kinetic parameters can be calculated from the glow curve.

5.1.3 Lithium tetraborate as a thermoluminescent material

The luminescence characteristic of materials has attracted attention of human beings since very long times [1, 2]. A number of thermoluminescent materials are available for the use in radiation dosimetry (clinical, radiotherapy, personnel) [3]. Among these materials, some particular properties are very interesting for lithium tetraborate which make it an attractive candidate for personnel dosimetry. These properties are its effective atomic number, linear dose response up to high doses, low fading, simple annealing procedure, simple glow curve, etc. Lithium tetraborate is a best tissue equivalent material. It is desirable that material use to measure human exposure to radiation should have similar atomic properties with human tissue. The effective atomic number of lithium tetraborate is 7.42, which is almost the same as that of the biological tissue [4]. The photoelectric absorption is most important for photons below 0.1 MeV, if the absorbing medium is water or a biological tissue. The photoelectric interaction is predominant in this energy range and depends on the third power of the atomic number (Z). Therefore, the effective atomic number of a dosimetric material should match as close as possible to that of the biological tissue. As the effective atomic number of LTB is very close to human tissue hence it is an important material to be used as personnel dosimeter. In contrast to commonly used TL materials, lithium tetraborate possesses perfect dose linearity up to 10^3 Gy. Generally dose linearity is not observed over 10 Gy. This high dose linearity makes lithium tetraborate rather distinct among other dosimeters [2, 5, 6]. The practicality of annealing is important when successive readouts is required. Annealing is a heating procedure applied to erase the previous radiations dose from the material and to prevent interference of its effect on the glow curve measurement. The annealing procedure is quite simple for the case of lithium tetraborate [2, 7, 8]. Simple glow curve is another important property for the production of dosimeters. The glow curves are particularly important because it indicates that whether a material can be used for TL dosimetry purposes or not. Many researchers investigated the TL properties of LTB doped materials with different activators such as: Mn, Cu, Ag, and Mg [9–15]. The first thermoluminescent material based on LTB activated by Mn is commercialized by Harshaw make under the name TLD-800.

The large band gap of lithium tetraborate provides a wide transparent energy window range to dopants [16]. Luminescence studies on LTB doped with different dopants (Ce, In, Ni, Cu and Ti ions) have been reported by many researchers in polycrystalline and glassy samples [17–20]. However, single crystals are more preferable due to their uniform dopant distribution, uniform crystal-field, absence of grain boundaries and very less scattering to visible light. These properties make single crystal highly transparent to visible light and very effective to collect the emitted light from the bulk of the samples. In addition, the resistance to humidity due to its stoichiometric composition, small surface area, simple annealing process, simplicity of glow curves, high sensitivity and easy handling compared with powder samples make the LTB single crystals a potential candidate for applications in the TLD [5]. Initially, LTB doped with Mn was reported to be a good TL dosimeter. Many researcher have studied thermoluminescence properties of Mn doped LTB single crystal. Mn doped LTB has problem of low TL sensitivity and light emission in the range of 600 nm, which is very far from the response region of most of the photo-multipliers. Some researcher [21] suggested copper doped LTB is a good TL phosphor as its TL emission is in the response region of photo multiplier tube (PMT). In the present work TL properties of irradiated undoped, Mn doped and Cu doped LTB single crystals, poly crystal and glass were studied and their kinetic parameters such as order of kinetics, activation energy and frequency factor were calculated and compared.

5.2 TL Studies on gamma irradiated Mn:LTB single crystal

Czochralski grown Mn doped $Li_2B_4O_7$ crystals were cut in the form of wafer and were irradiated with different γ-dose using Co^{60} source. Polished pieces of samples are shown in figure 5.2.

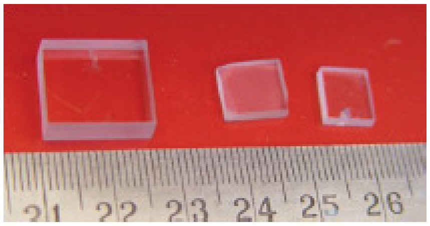

Fig. 5.2 Polished crystal pieces

Thermoluminescence glow curve of γ-irradiated Mn:LTB sample was taken by thermoluminescence dose reader analyzer (model- RA04). Thermoluminscence reader analyzer is shown in figure 5.3.

Fig. 5.3 Thermoluminescece reader analyzer (model-RA 04)

The TL glow curve of Mn LTB crystal is shown in figure 5.4. Generally for an ideal crystalline semiconductor or insulator Z(E) = 0 when $E_c > E > E_v$. Here E_c is the bottom of the conduction band and E_v is the top of the valance band. However, when the structural defects occurs in crystal, or if there is impurities within the crystal lattice, there is a breakdown in the periodicity of the crystalline structure and it become possible for the electrons to posses energies which are forbidden in the perfect crystal. Whenever we heat the sample the trapped electrons go to the conduction band and recombine with available hole and the luminescence occurs during this process.

5.2.1 Determination of kinetic parameters

The order of kinetics is also determined from the glow curve from the shape of the curve. First-order luminescence peak is asymmetric in nature with most of the peak area being on the low temperature side of the maximum at T_m. The second order luminescence peak is more symmetric in nature [22].

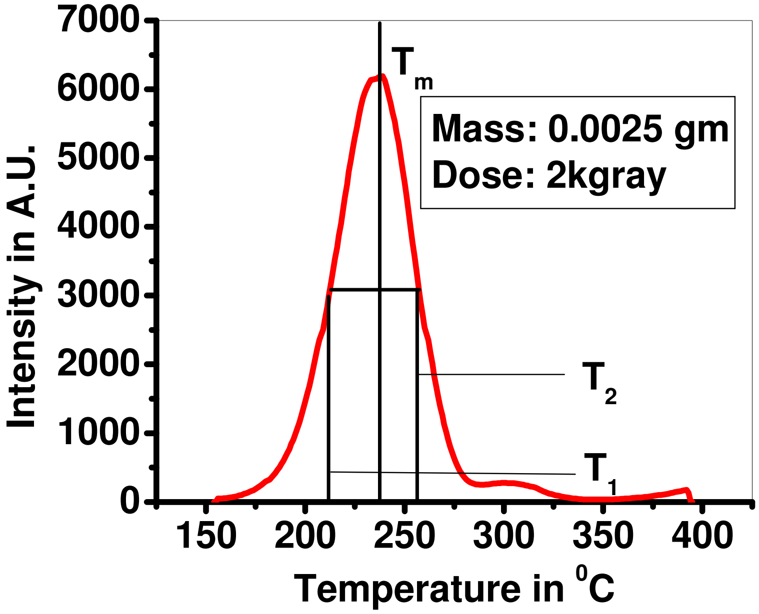

Fig. 5.4 Thermoluminescence spectra of gamma irradiated Mn: LTB single crystal

It can be seen from the figure 5.4 that the order of kinetics of the glow curve is First- Order. Here T_1= 212.87 °C, T_2=255.54 °C and T_m=237.76 °C. Therefore $\delta = T_2 - T_m = 17.78$, $\omega = T_2 - T_1 = 42.46$. Finally geometrical factor $\mu = \delta/\omega = 0.418$. That means once released from a trap the electron will undergo recombination rather than re-trapping. Occurrence of thermoluminescence peak maximum is related to the electron trap depth. The intensity of luminescence emission is proportional to the rate of release of trapped electron. The equation for first order glow peak is given by

$$I = (n_0 s/\beta)\exp(-E/kT)\exp\left[-(s/\beta)\int_{T_0}^{T}\exp(-E/kT)dT\right].$$

Here n_0 is the number of trapped electron at temperature T_0, E is the trap depth, s is the frequency factor and β is the heating rate. TL glow curve with various heating rate is shown in figure 5.5.

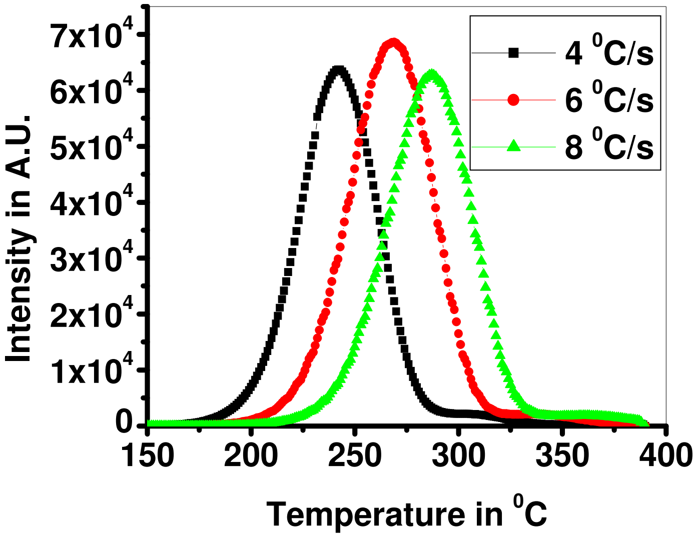

Fig. 5.5 TL curves with various heating rate

Trap depth and frequency factor is calculated from TL curve taken at various heating rates with the help of above equation. It is observed that the peak temperature shifted towards higher temperature as we increase the heating rate. The peak temperature is heating rate dependent because before saturation, the interaction time with electron is different for different heating rates. However, at high heating rate, the peak temperature gets saturated as maximum trapped electron goes to the conduction band independent of the interaction time. Differentiating the above equation for first order glow peak with respect to temperature and equating the derivative to zero gives [23] $\beta E/KT^2_m = s\exp(-E/KT_m)$, where T_m is the temperature at the maximum. Fig. 5.6 shows the plot of ln (T_m^2/β) versus $1/T_m$. From the slope E/k, activation energy E is calculated. The calculated trap depth is E = 1.08 eV.

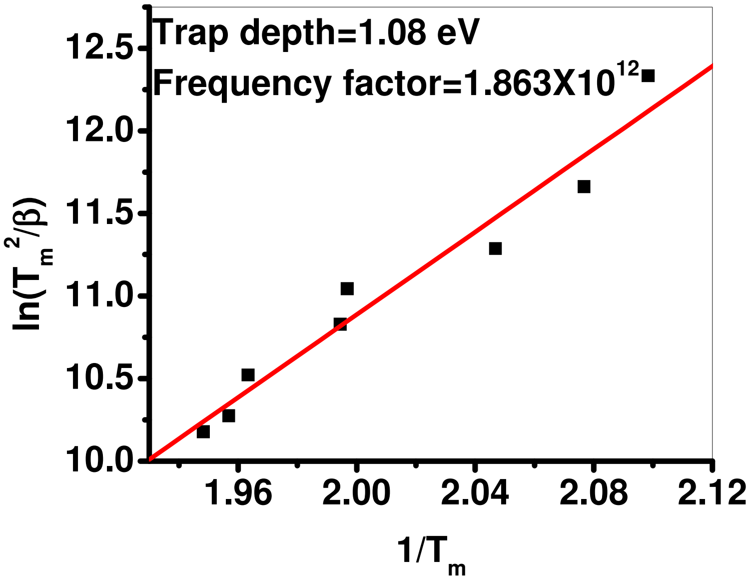

Fig. 5.6 Plot of ln (T_m^2/β) vs $1/T_m$ (at 2 kgray)

5.2.2 Calculation of activation energy from UV-VIS transmission spectra

Transmission spectra of the crystal wafer irradiated with different γ- dose were recorded using UV-Vis spectro photometer (cary-50). It has been observed that the transmittance of the crystal decreases with increasing dose level (Fig.5.7), which can be attributed to the generation of more crystalline defects on irradiation.

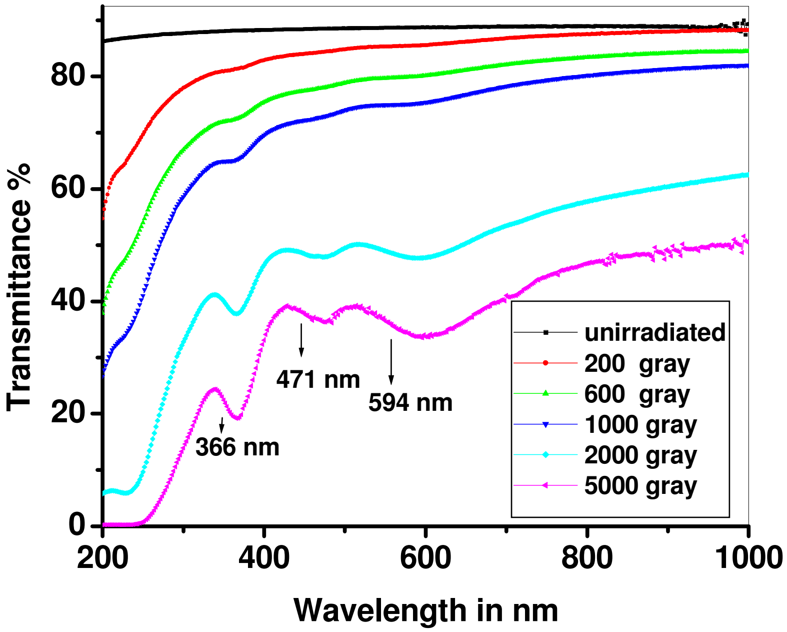

Fig. 5.7 Transmittance of Mn: LTB before and after γ-irradiation

As can be seen from the figure 5.7, the cut-off wavelength shifted to 230 nm and 250 nm respectively for the samples irradiated with 2 kgray and 5 kgray, which is much higher compared to the un-irradiated Mn doped LTB (~180 nm) [24]. Several absorption peaks were observed in the transmission spectra. Main peaks are observed at 366 nm, 471 nm and 594 nm. It has also been observed that the cut of wavelength and the depth of the absorption peak increases with increasing dose. These absorption peaks corresponds to the respective crystalline defect levels generated during the irradiation. The concentration of these defect levels increases with higher dose, resulting in more electrons to trap and hence the increase in the depth of the absorption peak. The overall transmittance becomes low in the irradiated samples due to increased defect density.

It is observed that the first absorption peak is more intense and the corresponding trap level(s) is/are responsible for thermoluminescence of the material. The cutoff wavelength represents the band gap of the material. Therefore, the separation between the band gap energy and the energy corresponding to the first absorption peak should represent the activation energy of the material. Band gap of irradiated crystals were calculated by plotting $(\alpha h\nu)^2$ versus $h\nu$. Figure 5.8 shows the representative plot of $(\alpha h\nu)^2$ versus $h\nu$ for samples irradiated with 2 kgray dose.

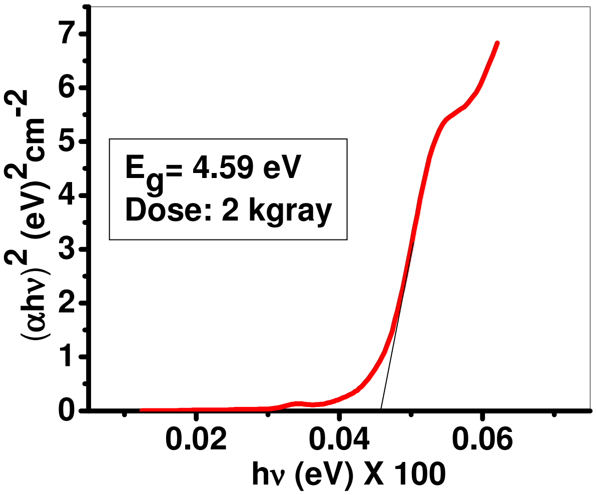

Fig. 5.8 Plot of $(\alpha h\nu)^2$ vs $h\nu$

Calculated band gap value was 4.59 eV for sample irradiated with 2 kgray. It has been observed from the transmission curve of the irradiated sample that the absorption peak at highest energy is at wavelength 366 nm and in lower wavelength range absorption starts from 339 nm. Corresponding to this wavelength the energy is 3.66eV. This 3.66 eV is the energy difference between valance band and highest trap level. Therefore, activation energy or trap depth is (4.59-3.66) eV= 0.93 eV. The calculated trap depth from heating rate method is E = 1.08eV for sample irradiated with 2 kgray. Whereas, activation energy or trap depth is 0.93eV from transmission data. Therefore, it has been found that the calculated trap depth is quite close from the two different methods.

5.2.3 Mass dependency of TL glow curve

Mass dependency of the irradiated sample with TL intensity is observed here. Mn: LTB is very much mass sensitive, TL intensity changes very much even with small change in crystal mass (1 or 2 mg). In figure 5.9, maximum TL intensity with various mass is plotted.

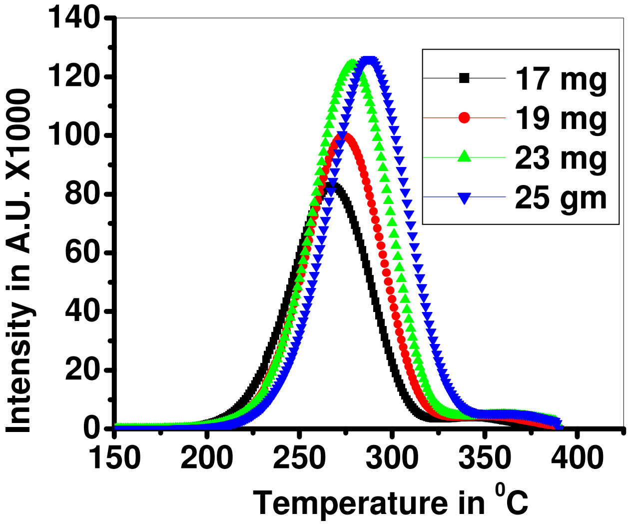

Fig. 5.9 Mass dependence of TL intensity

TL curves are recorded with constant heating rate (rate 2 ºC/s). The TL sensitivity of the material is also measured from these curves. As expected the shift in peak position of TL curves was found towards high temperature. The sensitivity of TL intensity due to the small change in mass at the same dose, as can be seen from the figure 5.9, is an important feature of this material. Therefore, the accuracy in mass of the material is very crucial for making highly reliable TLD badge.

5.2.4 Study of dose dependency and sensitivity

Crystal samples were irradiated with various dose to study the dose dependency. Dose dependency of Mn LTB single crystal is shown in figure 5.10.

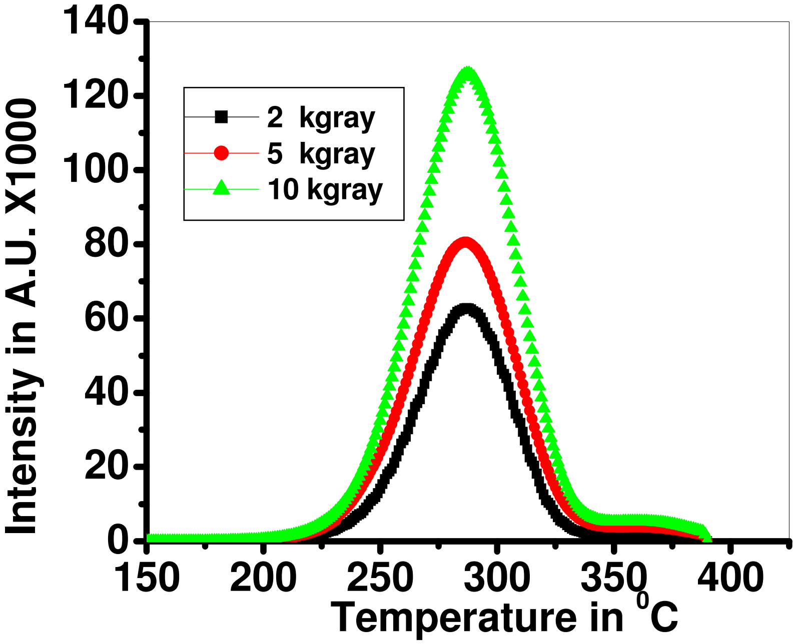

Fig. 5.10 Dose dependency of TL intensity of Mn: LTB single crystal

It has been observed that TL intensity increases with dose. Number trapped electron increases with dose. The sensitivity of particular TLD material is defined as TL intensity integrated over a certain temperature region per unit mass per unit absorbed dose [1]. Here the sensitivity becomes =19,33,718/.0091gm/2000 gray = 1, 06,248 unit per gm/gray.

5.2.5 Fading Study

The loss of TL signal, known as Fading, must be low in a good dosimetry material. In some cases, when the read-outs cannot be performed quickly after each exposure, the fading become an important parameter. Fading is designated by a decrease in the intensity of a peak in glow curve over a time span. We kept our sample covered with black paper inside a box. After six month glow curve was taken. Fading is shown in figure 5.11. In these samples of Mn: LTB , only 5-6% fading is observed in six months when the sample is kept closed inside the sample box.

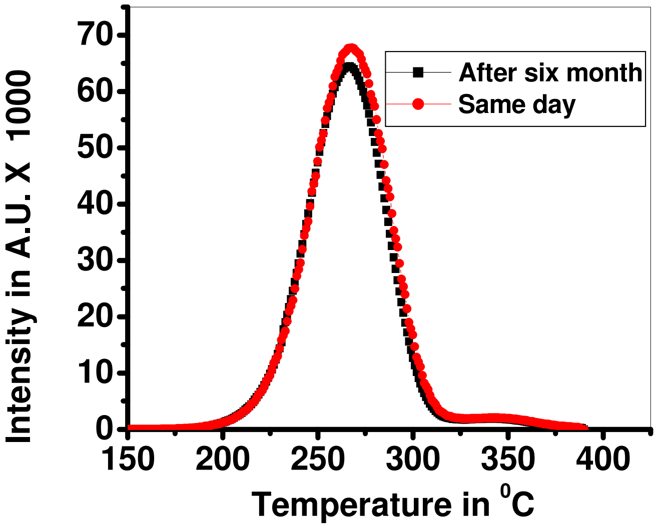

Fig. 5.11 Fading studies of irradiated Mn: LTB single crystal

5.3 TL studies of X-ray irradiated doped and undoped LTB glass

5.3.1 Sample preparation

Stoichiometric composition of Li_2CO_3 and B_2O_3 were used to prepare $Li_2B_4O_7$ powder. Two chemicals were grinded for 1h in agate mortar. The mixture was then milled for 1h at the rate of 300 rpm in a high energy ball mill. Ball milling also helps in reducing the particle sizes as well. Homogeneously mixed powder was filled in a platinum crucible and was kept in the furnace and heated up to 400 °C at the heating rate of 100 °C per hour and kept for 3h. This powder was removed from the crucible and again mixed in an agate mortar for 1h. This mixture was kept in a platinum crucible again and annealed at 750 °C for 10h. In this process the single phase LTB polycrystalline powder was obtained. With a similar method, 0.2 mole% Mn doped and 0.2 mole% Cu doped LTB powders were also synthesized. The synthesized powder was then melted in box furnace at 920^{o}C. The temperature of the melt is then raised to 980°C and kept for two hours for homogenization of the melt. Then the melt is poured in a preheated metallic plate and immediately pressed with another metallic plate to make glass. Here nucleation and growth were bypassed by sufficiently rapid cooling. Transparent crack free glasses were obtained. Transparent glasses are shown in figure 5.12.

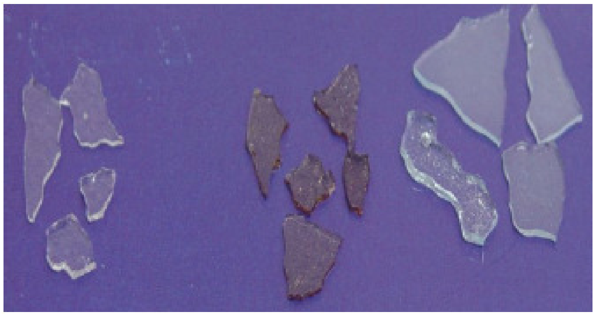

Fig. 5.12 Photograph of undoped and doped glass plate

5.3.2 Sample Irradiation

These undoped, Mn doped and Cu doped LTB glass were irradiated with X-rays at beam line (BL- 07) on the Indian synchrotron radiation source, Indus-2. This beam line has versatility to expose the various samples to soft and hard X-ray energies tuned using two X-ray mirrors. The X-ray spectral energy band of 3-10 keV was used for irradiation in the present studies. In a synchrotron radiation source, the flux (dose) falling on the samples is directly proportional to current stored inside in the storage ring (Indus-2) and expressed in the units of (mA.s). The samples were scanned in the path of the X-ray beam for a given time. Different doses were given to the sample by varying the number of pass keeping scanning speed constant at almost same beam current. In our case beam current was 66.2 mA, integrated flux was around 3.46 X10^{12} photons per sec and scanning speed was 6 mm/s.

5.3.3 TL glow curve of X-ray irradiated undoped, Mn doped and Cu doped glass

The irradiated samples were read by a TL reader analyzer (RA 04 model). TL glow curves of doped and undoped LTB glasses are shown in fig 5.13. It has been observed that for glassy sample only one peak occurs. The intensity of TL peaks for glass are less than that of crystalline sample because of nonradiative recombination. This may be caused by the poor energy storage of the irradiation in the glasses, i.e., poor trapping efficiency. Differences in the structure and shape of the TL glow curves of the glassy and corresponding single crystals can be explained by the differences in the characteristics of the charge traps. TL count per pass per mg per mA is 7, 15, and 31 for undoped, Mn doped and Cu doped LTB glass respectively.

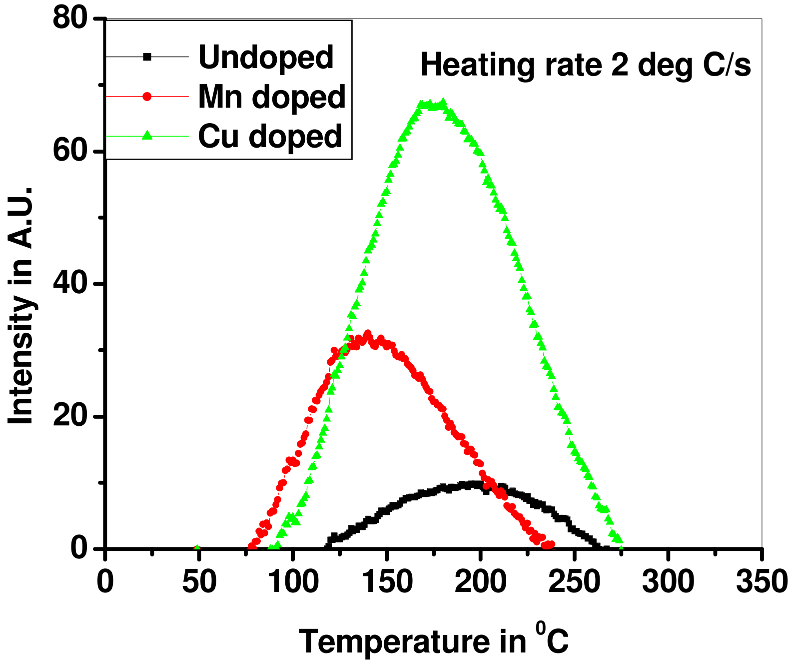

Fig. 5.13 TL glow curve of undoped, Mn doped and Cu doped glass

Glasses have no long range order and are thermodynamically unstable compared to crystal. During rapid cooling it remain disordered and become a super cooled liquid. As temperature decreases viscosity of the liquid will rise and rearrangement of atoms ceases, which produces amorphous solid. The chemical bonding in glasses is very similar to that one in crystal of same composition. This is why position and structure of main absorption band are very similar in crystalline and amorphous material. The most important difference in glasses is significantly lower mobility of charge carrier. This difference is caused by number of localized level in the range of bottom of conduction band in glass. Band gap exist in glass because of finite energy required to excite an electron in a bonding state into an anti bonding state. An anti boding orbital is a form of molecular orbital that is located outside the region of two distinct nuclei. The overlap of the constituent atomic orbital is said to be out of phase, and as such the electron present in each anti bonding orbital are repulsive and act to destabilize the molecule as a whole. Anti bonding molecular orbital are normally higher in energy than bonding molecular orbital. In glass trap center is generated due to co-ordination defect, i.e., the number of atoms surrounding a particular atom is not same.

A. Determination of Order of Kinetics from Glow Curve

Glow curve with T_1, T_2 and T_m are shown in fig.5.14 (a), (b), (c) for undoped, Mn doped and Cu doped LTB glass respectively.

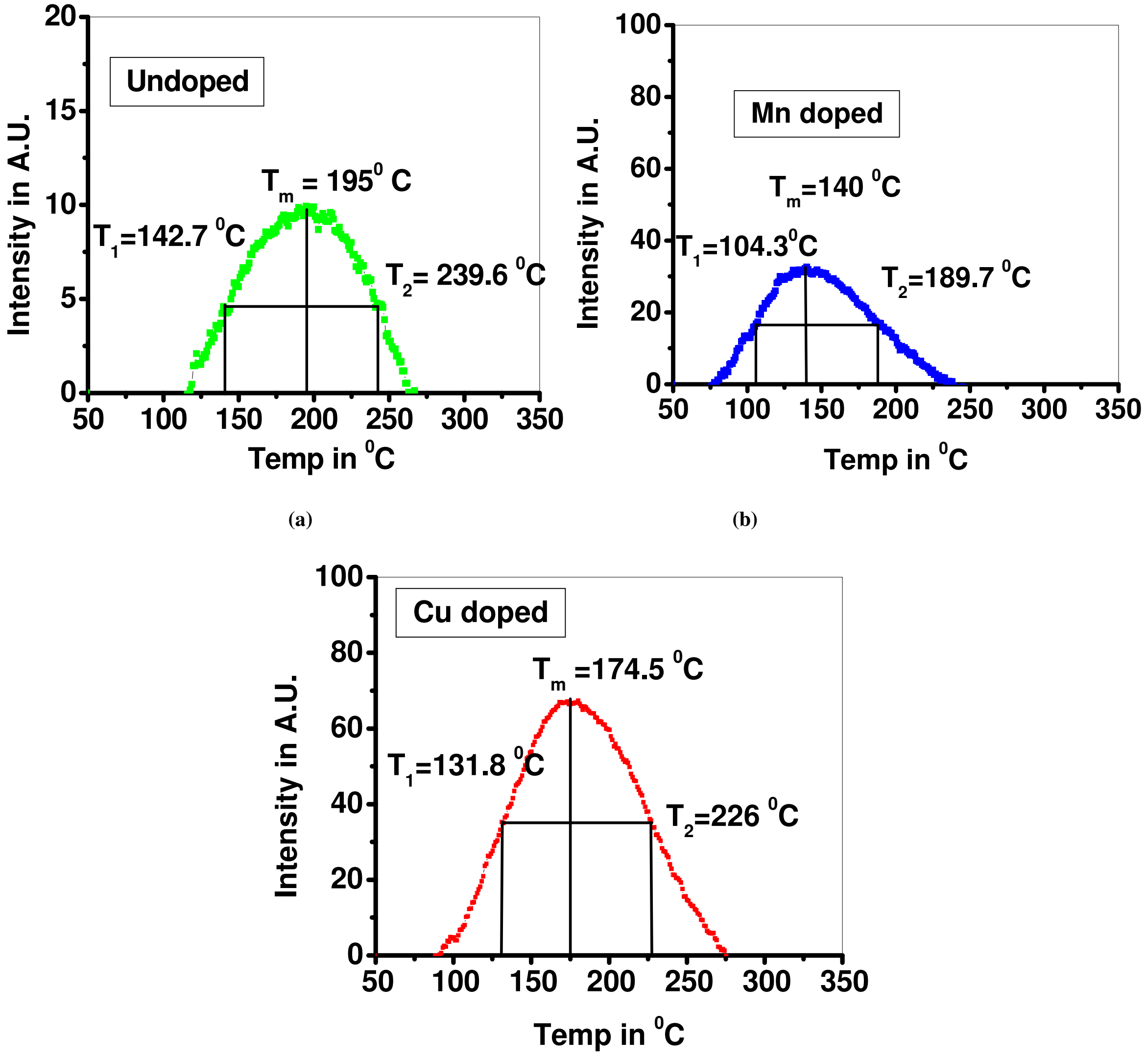

(a) **(b)**

(c)

Fig. 5.14 Glow curve of (a) undoped (b) Mn doped (c) Cu doped LTB glass with T_1, T_2 and T_m

From the symmetry factors of glow curve the order parameters were determined. If the shape of the glow curve is asymmetric, that is wider on the low temperature side than on the high temperature side then the curve is first order. This means all electrons released from the trap undergo transition, i.e. there is no retraping. This leads to concept that the rate of release of electron is proportional to the trapped charge concentration. In Second-order peaks the rate of change of the population is proportional to n^2. From glow curve, temperature T_1 for half maxima at low temperature side, temperature T_2 for half maxima at high temperature side and Peak temperature T_m is determined. Symmetry factors of the glow curves were calculated and given in table 5.1.

Table 5.1 Calculation of symmetry factor of undoped, Mn doped and Cu doped glass

	Undoped glass	**Mn doped glass**	**Cu doped glass**
T_1 (in °C)	**142.7 +/- 0.1**	**104.3 +/- 0.1**	**131.8 +/- 0.1**
T_2 (in °C)	**239.6 +/- 0.1**	**189.7 +/- 0.1**	**226 +/- 0.1**
T_m (in °C)	**195 +/- 0.1**	**140 +/- 0.1**	**174.5 +/- 0.1**
$\tau = T_m - T_1$ (in °C)	**52.3 +/- 0.2**	**35.7 +/- 0.2**	**42.7 +/- 0.2**
$\delta = T_2 - T_m$ (in °C)	**44.6 +/- 0.2**	**49.7 +/- 0.2**	**51.5 +/- 0.2**
$\omega = T_2 - T_1$ (in °C)	**96.9 +/- 0.2**	**85.4 +/- 0.2**	**94.2 +/- 0.2**
$\mu = \delta/\omega$	**0.46 +/-0.003**	**0.581 +/-0.003**	**0.546 +/-0.003**

Here peaks are very broad compare to single crystal and poly crystalline sample, which implies that the trapping states are not sharp. These broad trap centers are due to co-ordination defect. Amorphous sample follows second order kinetics, which means possibility of retraping is more. Multiple trap centers are present here.

B. Determination of activation energy and frequency factor from glow curve

Plot of ln(I) Vs 1/T for undoped, Mn doped and Cu doped LTB glass are shown in figure 5.15(a), (b), (c) respectively. From the slope of the graph activation energies were calculated. Calculated activation energy and frequency factors are shown in table 5.2. Activation energy increases in the order undoped, Cu doped and Mn doped LTB glass.

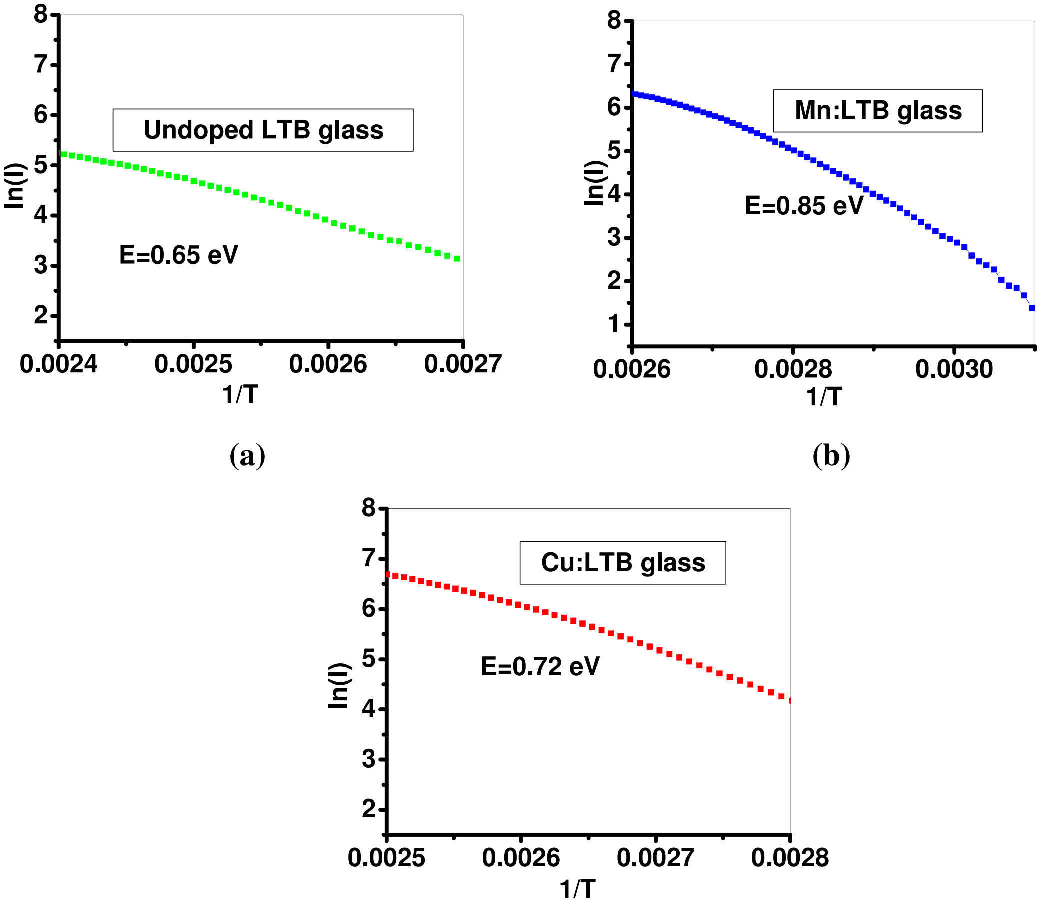

(a) (b)

(c)

Fig. 5.15 Plot of ln(I) vs 1/T for (a) undoped LTB glass (b) Mn doped LTB glass and (c) Cu doped LTB glass

From the slope of the graph activation energies were calculated.

Table 5.2 Activation energy and frequency factor of undoped, Cu doped and Mn doped LTB glass.

	Undoped LTB glass	**Mn doped LTB glass**	**Cu doped LTB glass**
E (eV)	**0.65 +/- 0.01**	**0.85 +/- 0.01**	**0.72 +/- 0.01**
S (per sec)	**6.9 X 10^7**	**2.7 X10^9**	**1.08 X10^7**

In case of glass observed frequency factor is very less due to high viscosity of glass which slowed down the movement of electrons.

5.3.4 Transmission Spectra of Irradiated Mn doped LTB Glass

Glass samples were polished properly through alumina powder. Polished samples were irradiated. Transmission spectra of irradiated Mn doped LTB glass and unirradiated LTB glass samples were shown in figure 5.16. It has been observed that transmittance decreases in the irradiated sample. This is due to generation of defect induced by radiation.

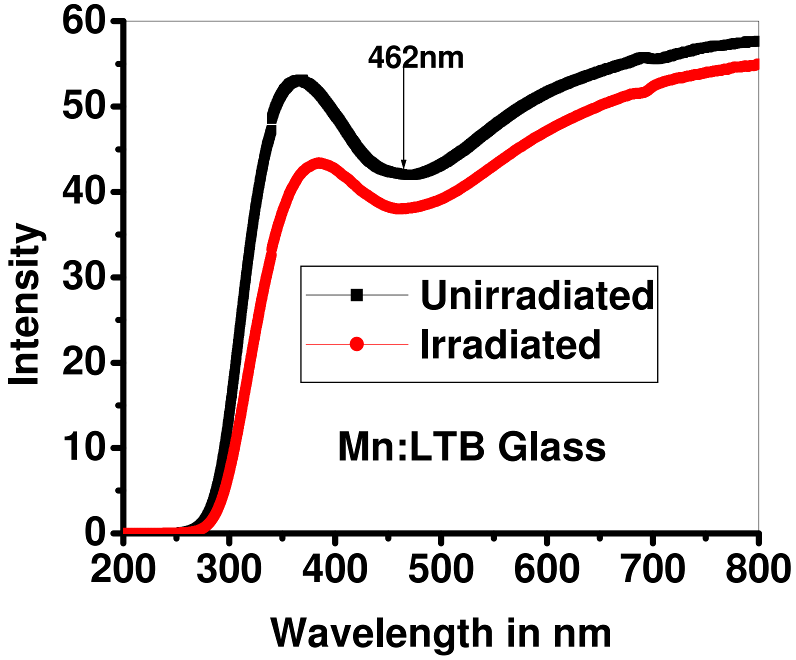

Fig. 5.16 Transmission spectra of irradiated Mn doped LTB glass

5.3.5 Fading study of irradiated LTB glass sample

Decrease of TL intensity with time has been studied for irradiated LTB glass sample. Samples were covered with black paper and kept inside box. After one month TL glow curves were taken through TLD reader. Fig. 5.17 (a) and (b) shows fading studies of Mn LTB glass and Cu LTB glass. It has been observed that after one month area under curve decreased significantly. Percentage of decrease is more in case of Mn doped glass. It has also been observed that peak temperature shifts toward higher temperature in fading studies. In low temperature region TL intensity become zero when we read the sample after one month. This is because of the recombination of some trapped electron with hole at room temperature.

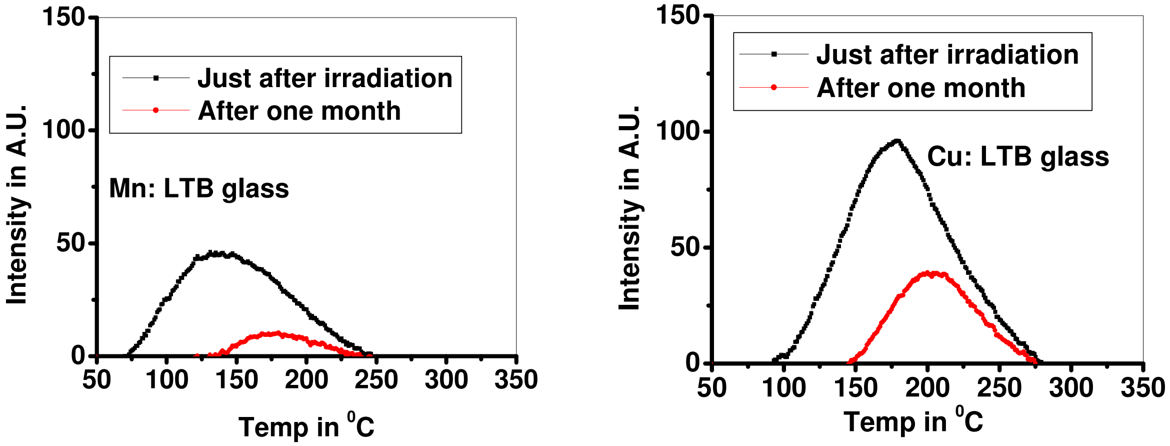

(a) **(b)**

Fig. 5.17 Fading study of irradiated (a) Mn doped LTB glass sample and (b) Cu doped LTB glass sample

5.4. TL studies of X-ray irradiated doped and undoped LTB polycrystal

5.4.1. Sample preparation

Stoichiometric compositions of Li_2CO_3 and B_2O_3 were used to prepare $Li_2B_4O_7$ powder. The two chemicals were grinded for 1h in agate mortar. The mixture was then milled for 1h at the rate of 300 rpm in a high energy ball mill. A platinum crucible was filled with the homogeneously mixed powder, and then heated in a furnace at a rate of 100 °C/hr to 400 °C/hr, where it was kept for 3h. This powder was removed from the crucible and again mixed in an agate mortar for 1h. This mixture was kept in a platinum crucible again and annealed at 750 °C for 10h. By this process, the single phase LTB polycrystalline powder was obtained. With a similar method, 0.2 mole % Mn doped and 0.2 mole % Cu doped LTB powders were also synthesized. The pallets were made from the above compositions of undoped, Mn doped and Cu doped LTB using 20 mg powder each. The pallets were made of 6 mm diameter and 1mm thickness using pallet press machine with 3.5 ton pressure. Prepared pallets are shown in figure 5.18. These pallets were annealed at 400 °C for 2 hr to release strain present during preparation.

Fig. 5.18 Photograph of undoped, Mn doped and Cu doped LTB polycrystalline pallet

5.4.2 Sample irradiation

These undoped, Mn doped and Cu doped LTB pallets were irradiated with X-rays at beam line (BL- 07) on the Indian synchrotron radiation source, Indus-2. The X-ray spectral energy band of 3-10 keV was used for irradiation in the present studies. The samples were scanned in the path of the X-ray beam for a given time. Different doses were given to the sample by varying the number of pass keeping scanning speed constant at almost same beam current. In our case beam current was 66.2 mA, integrated flux was around 3.46 X10^{12} photons per sec and scanning speed was 6 mm/s.

5.4.3 TL glow curve of X-ray irradiated undoped, Mn doped and Cu doped pallet

The irradiated samples were read by a TL reader analyzer (RA 04 model). Two peaks were observed in the glow curve. It has been observed that for the same dose, TL intensity was highest for Cu doped LTB sample and lowest for undoped LTB sample, while the value for Mn doped sample lies in-between. Thermoluminescence glow curves of these samples irradiated with same dose are shown in figure 5.19.

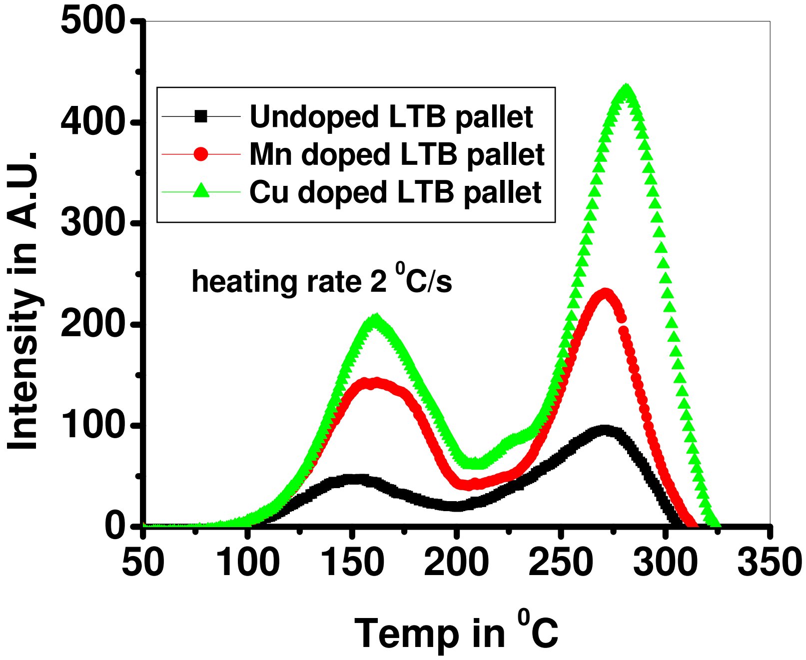

Fig. 5.19 TL spectra of undoped, Mn doped and Cu doped LTB pallets (per mg)

The heating rate was 2 °C/s for each sample. It was observed that TL also occurs for undoped LTB sample but with less intensity. It confirms that there are some intrinsic defects and trap centers present undoped samples also. However, doping enhances the defect density and, as a result, the intensity of glow curve increases. It had been reported recently that Mn: LTB and Cu: LTB have emission around 608 nm and 370 nm respectively [25]. It is understood that on irradiation, Cu^{+} and Mn^{2+} ions are converted to Cu^{2+} and Mn^{3+} by the release of electrons. From the glow curve, TL counts for unit mass per mA beam current per scan of X-ray beam were calculated. The calculated values are 14, 32, 44 counts for undoped, Mn doped and Cu doped LTB pallets respectively. In LTB sample two well separated peaks were observed. These two peaks correspond to two different trap centers. It has been observed that TL intensity is very less for undoped LTB polycrystalline pallet. Earlier it was reported by some researcher that undoped LTB does not give TL but we observed significant TL intensity for undoped sample also. This is due to some very less amount of impurity which is already present in parent material.

A. Determination of order of kinetics from glow curves

From the shape of the glow curve geometric factor μ for two different peaks of undoped, Mn doped and Cu doped pallets were calculated and are shown in table 5.3, table 5.4 and table 5.5 respectively.

Table 5.3 Calculation of geometric factor for undoped LTB pallet

Undoped pallet	**1st peak**	**2nd peak**
T_1 (in °C)	**122.9 +/- 0.1**	**233.9 +/- 0.1**
T_2 (in °C)	**186.9 +/- 0.1**	**291.8 +/- 0.1**
T_m (in °C)	**151.3 +/- 0.1**	**271.6 +/- 0.1**
$\tau = T_m - T_1$ (in °C)	**28.4 +/- 0.2**	**37.7 +/- 0.2**
$\delta = T_2 - T_m$ (in °C)	**35.6 +/- 0.2**	**20.2 +/- 0.2**
$\omega = T_2 - T_1$ (in °C)	**64 +/- 0.2**	**57.9 +/- 0.2**
$\mu = \delta/\omega$	**0.556 +/-0.005**	**0.349+/-0.004**

Table 5.4 Calculation of geometric factor for Mn doped LTB pallet

Mn doped pallet	**1st peak**	**2nd peak**
T_1 (in °C)	**132.2 +/- 0.1**	**246 +/- 0.1**
T_2 (in °C)	**190.9 +/- 0.1**	**290 +/- 0.1**
T_m (in °C)	**161.6 +/- 0.1**	**271 +/- 0.1**
$\tau = T_m - T_1$ (in °C)	**29.4 +/- 0.2**	**25 +/- 0.2**
$\delta = T_2 - T_m$ (in °C)	**29.3 +/- 0.2**	**19 +/- 0.2**
$\omega = T_2 - T_1$ (in °C)	**58.7 +/- 0.2**	**44 +/- 0.2**
$\mu = \delta/\omega$	**0.499+/-0.005**	**0.432+/-0.006**

Table 5.5 Calculation of geometric factor for Cu doped LTB pallet

Cu doped LTB pallet	**1st peak**	**2nd peak**
T_1 (in °C)	**137.5 +/- 0.1**	**255.5 +/- 0.1**
T_2 (in °C)	**191.7 +/- 0.1**	**302.5 +/- 0.1**
T_m (in °C)	**160.6 +/- 0.1**	**281.7 +/- 0.1**
$\tau = T_m - T_1$ (in °C)	**23.1 +/- 0.2**	**26.2 +/- 0.2**
$\delta = T_2 - T_m$ (in °C)	**35.6 +/- 0.2**	**20.8 +/- 0.2**
$\omega = T_2 - T_1$ (in °C)	**59.4 +/- 0.2**	**47 +/- 0.2**
$\mu = \delta/\omega$	**0.6+/-0.005**	**0.442+/-0.006**

Where,

T_1= Temperature of half maxima at the low temperature side of the peak.

T_2= Temperature of half maxima at the high temperature side of the peak.

T_m = Temperature of peak maxima.

$\tau = T_m - T_1$ is the half-width at the low temperature side of the peak.

$\delta = T_2 - T_m$ is the half-width at the high temperature side of the peak.

$\omega = T_2 - T_1$ is the total half – width.

$\mu = \delta / \omega$ is so-called geometrical shape of symmetry factor.

From three tables it has been observed that first peaks are obeying second order kinetics and second peaks are obeying first order kinetics.

B. Determination of activation energy and frequency factor from glow curves

Activation energies were calculated through initial rise method by plotting 1/T vs ln(I). Fig.5.20 (a) and (b) shows graph of 1/T vs ln(I) of undoped, Mn doped and Cu doped LTB poly crystalline sample for first peak and second peak respectively.

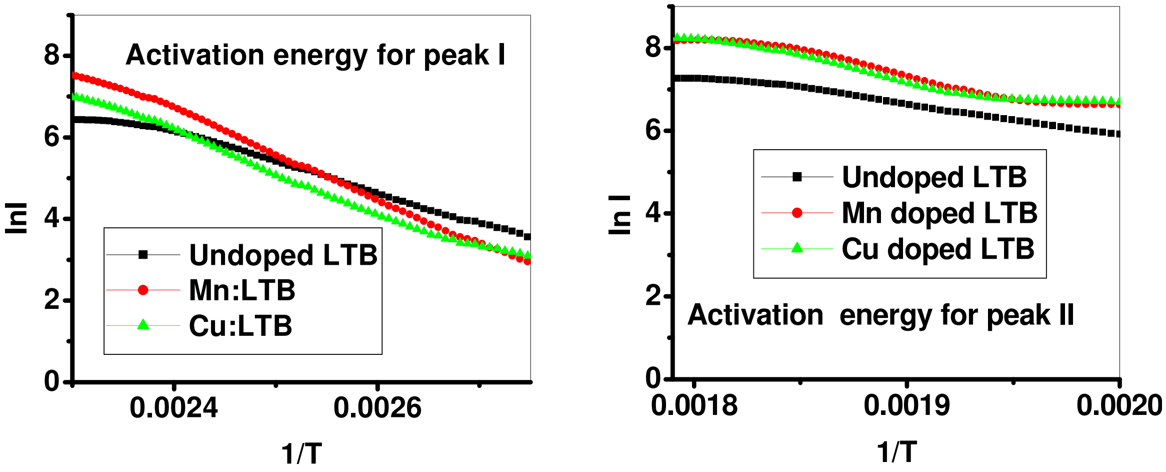

(a) (b)

Fig. 5.20 Plot of 1/T vs ln(I) for (a) first peak (b) second peak of polycrystalline undoped, Mn doped and Cu doped pallet

By calculating activation energy frequency factors were calculated from the equation $\beta E/KT^2_m = s \exp(-E/KT_m)$. The values of activation energies and frequency factors are shown in table 5.6.

Table 5.6 Activation energy and frequency factor of undoped, Cu doped and Mn doped LTB pallet

	E_1 (eV)	**S_1 (per sec)**	**E_2 (eV)**	**S_2 (per sec)**
Undoped LTB	**0.72 +/- 0.01**	**$3.3X10^7$**	**0.95 +/- 0.01**	**$4.6X10^7$**
Mn doped LTB	**1.10 +/- 0.01**	**$7.9X10^{11}$**	**1.26 +/- 0.01**	**$4.7X10^{10}$**
Cu doped LTB	**0.98 +/- 0.01**	**$3X10^{10}$**	**1.16 +/- 0.01**	**$2.8X10^9$**

5.4.4 TL glow curve of Mn doped LTB polycrystalline pallet at different heating rate

The TL curves for Mn doped LTB pallets at different heating rates are shown in Fig. 5.21. It can be seen from these curves that the TL peaks shift towards a higher temperature for higher heating rate.

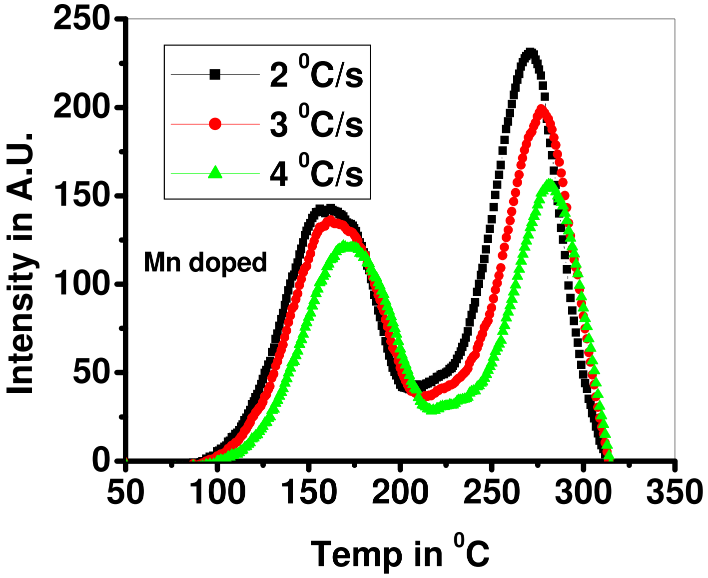

Fig. 5.21 TL glow curve of Mn doped LTB pallets at various heating rates

TL peak shifts towards higher temperature with increasing heating rate, as electrons do not get sufficient time to come out from the trap center at faster rate and hence peak intensity comes at higher temperature. It is also observed that the thermoluminescence intensity decreases with the increase of heating rate because of thermal quenching effect. Thermal quenching effect is competition between radiative transition (which is almost temperature independent) and non radiative transition which increases with temperature [26].

5.4.5 Dual Reading of Irradiated Undoped and Doped LTB Pallets

Generally, the TLD is read once to get the dose information stored in it. If the data is lost due to some reason, then there is no option to retrieve the data. In the TL glow curves observed for undoped and doped polycrystalline pallets, two well separated peaks are present. The first peak is from 50°C to 210°C and the second peak is from 210 °C to 320°C. The area under the first and second peaks was measured separately. The ratios of the area under the peaks follow a particular trend for each material. The ratio have been calculated for each sample and approximately found as: 30:70 for undoped LTB, 41:59 for Mn:LTB, and 33:67 for Cu: LTB. The idea of using the first peak to get the dose information immediately after irradiation has not been reported previously. A scheme is proposed here which uses the presence of these two peaks separated by sufficient temperature span to read the TL dosimeter twice. In this scheme, by heating the sample up to 210°C, the full dose information may be obtained immediately. Again, the same information can be obtained second time from the TLD data if the sample is heated up to 320°C. The area under the two peaks and under the whole glow curve has been calculated for each sample. The fractional area under peak-I and peak-II for undoped, Mn doped and Cu doped pallets are shown in Table 5.7.

Table 5.7 Fractional area under peak-I and peak-II for undoped, Mn doped and Cu doped LTB pallets

Sample	**Heating rate (°C/s)**	**Area under peak I**	**Area under peak II**	**Fractional area under peak I**	**Fractional area under peak II**
LTB	**2**	**75085**	**170416**	**0.305**	**0.695**
Mn: LTB	**2**	**153480**	**219992**	**0.410**	**0.590**
Cu: LTB	**2**	**194654**	**404667**	**0.330**	**0.670**

As a proof of concept, two Mn doped LTB pallets were irradiated with the same dose. Fig. 5.22 shows the TL glow curves taken for dual reading of dosimeter. A TL curve was obtained by heating the first sample from 50 – 320 °C. For the second sample, a TL glow curve was taken in two steps. In the first step, the temperature was between 50 – 210 °C and in second step it was from 210 to 320 °C. In this case, the fractional area under peak-I is 0.41 and for peak-II, the value is 0.59. The same measurements were performed for undoped and Cu doped pallets. The values were found matching when the samples were read step wise.

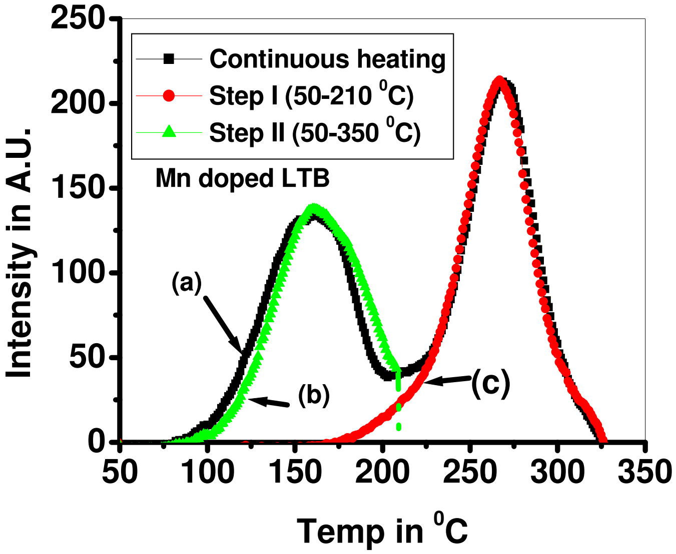

Fig. 5.22 Dual reading of dosimeter; TL curve in whole temperature range (a) , TL curve for temperature range 50-210 °C (b), TL curve for second time reading of same sample from 50-320 °C (c)

5.4.6. Fading Studies

To study fading, two pallets of each material were irradiated with same dose. TL glow curves were taken at the same day irradiation using one pallet. Second number pallet of each material were covered with black paper and kept inside a box to protect from light induced fading. Second pallets of each material were read by TLD reader after 36 days of irradiation. TL glow curve of undoped LTB, Mn:LTB and Cu:LTB pallets just after irradiation and after 36 days of irradiation are shown in fig 5.23 (a), (b), (c) respectively. The activation energy of the first peak is less than the second peak, hence the first peak fades quickly even at room temperature. During fading the trapped electrons of first peak which resides very close to the conduction band can jump to conduction band very easily and remaining deep lying electron reside in the trap. After 36 days when the sample was heated and glow curves were taken, the electron has to jump some extra barrier because they are lying in deeper level; as a result the activation energy increases for first peak. It is also observed that the fading of the second peak is significant in the case of undoped sample, as the number of trapped electron is much less compared to the doped sample. For undoped LTB, the first peak shift from 154°C to 174 °C; i.e. ΔT = 20 °C, for Mn: LTB pallet the peak shift from 174.4 °C to 177.5 °C ; i.e. ΔT = 3 °C, for Cu: LTB pallet the peak shift from 175 °C to 183 °C ; i.e. ΔT = 8°C. The temperature shift is maximum for undoped

LTB and minimum for Mn: LTB. For the second peak no shifting was observed which indicates that fading rate is negligible. After 36 days when the sample was heated and glow curves were taken, the electron has to jump some extra barrier because they are lying in deeper level; as a result the activation energy increases for first peak.

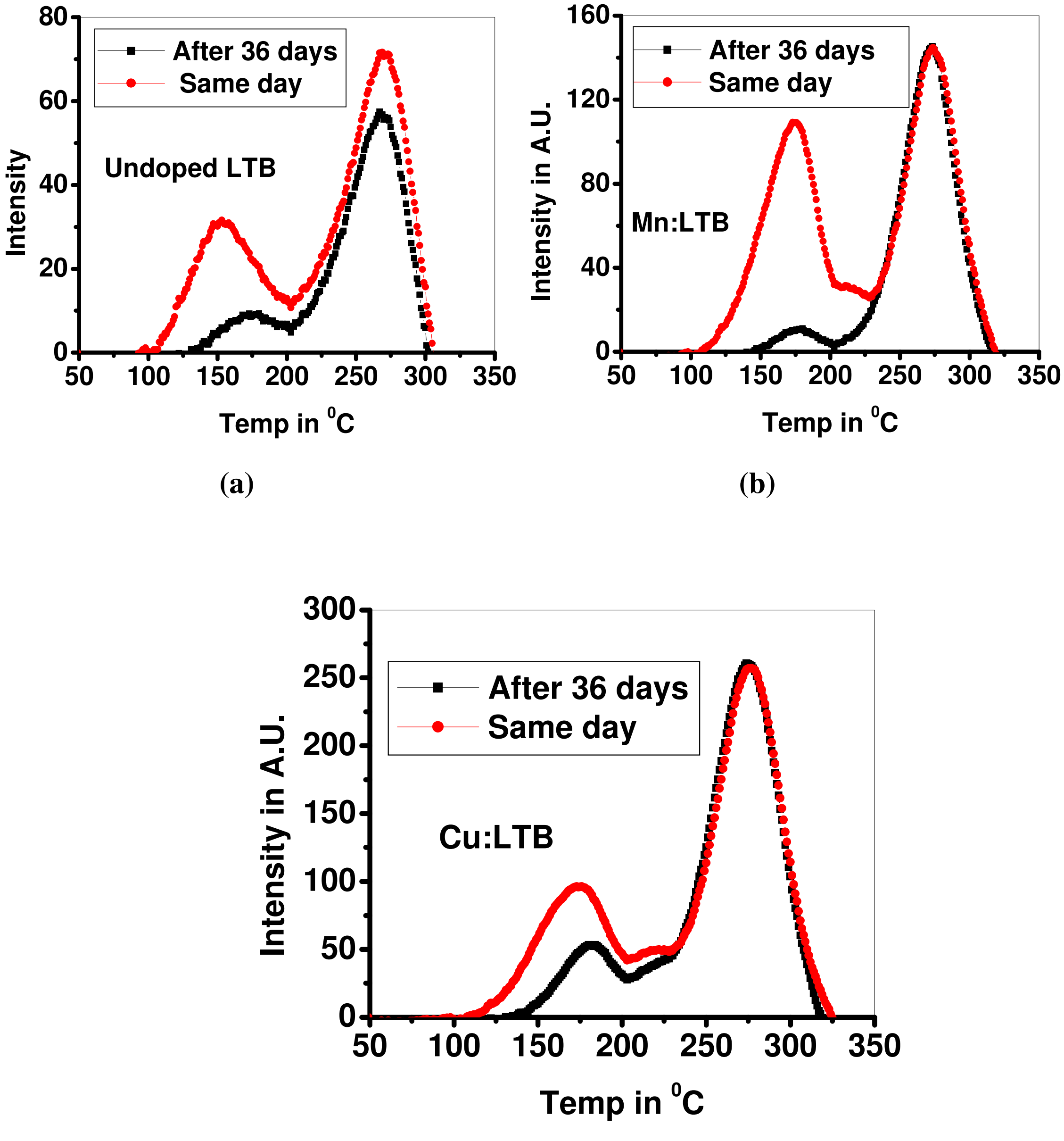

(a) (b)

(c)

Fig. 5.23 TL glow curves for (a) undoped LTB pallets (b) Mn doped LTB pallet (c) Copper doped LTB pallet on same day and after 36 days of irradiation

5.5 TL studies of X-ray irradiated undoped and doped LTB single crystals

5.5.1 Sample preparation

Stoichiometric composition of Li_2CO_3 and B_2O_3 were used to prepare $Li_2B_4O_7$ powder. Two chemicals were grinded for 1h in agate mortar. The mixture was then milled for 1h at the rate of 300 rpm in a high energy ball mill. Ball milling also helps in reducing the particle sizes as well. Homogeneously mixed powder was filled in a platinum crucible and was kept in the furnace and heated up to 400 °C at the heating rate of 100 °C per hour and kept for 3h. This powder was removed from the crucible and again mixed in an agate mortar for 1h. This mixture was kept in a platinum crucible again and annealed at 750 °C for 10h. In this process the single phase LTB polycrystalline powder was obtained. With a similar method, 0.2 mole% Mn doped and 0.2 mole% Cu doped LTB powders were also synthesized. The synthesized powder was then melted in box furnace at 920°C. The temperature of the melt is then raised to 980°C and kept for two hours for homogenization of the melt. To grow single crystal Cz technique was used. The prepared charge is melted at 920°C in a platinum crucible in a cylindrical furnace and a seed crystal is dipped into the melt to grow crystal. Grown crystals were cut into small pieces and polished for thermoluminescence studies.

5.5.2 Sample irradiation

These undoped, Mn doped and Cu doped LTB single crystals were irradiated with X-rays at beam line (BL- 07) on the Indian synchrotron radiation source, Indus-2. The X-ray spectral energy band of 3-10 keV was used for irradiation in the present studies. The samples were scanned in the path of the X-ray beam for a given time. Different doses were given to the sample by varying the number of pass keeping scanning speed constant at almost same beam current. In our case beam current was 66.2 mA, integrated flux was around 3.46×10^{12} photons per sec and scanning speed was 6 mm/s.

5.5.3 Studies of TL glow curve of irradiated sample

Irradiated undoped and doped single crystals were read through TLD reader. Glow curves are shown in fig. 5.24(a), (b), (c) for undoped, Mn doped and Cu doped single crystal respectively.

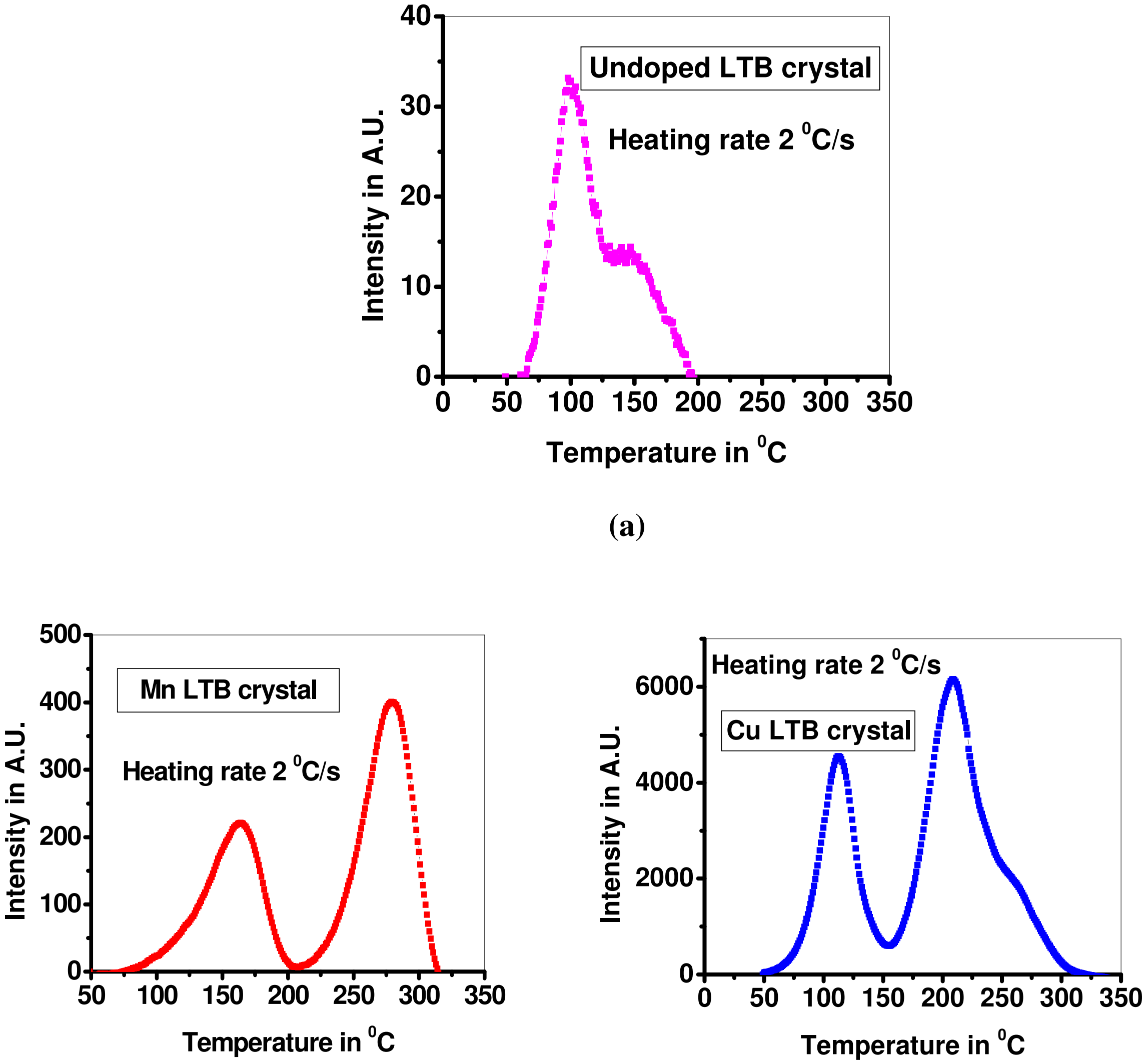

(a)

(b)

(c)

Fig. 5.24 TL glow curve of X-ray irradiated (a) Undoped, (b) Mn doped and (c) Cu doped LTB single crystal

In case of undoped LTB single crystal only one peak comes but second peak is absent. For undoped single crystal sample thermoluminscence comes due to intrinsic defects inside the crystal (oxygen or lithium vacancies). During growth of single crystal material tries to reject the impurity so single crystal material is more pure than the poly crystalline pallet. So we can say that the first peak comes due to intrinsic defect (oxygen or lithium vacancies) and second peak is coming due to dopant. From the TL glow curve it is observed that the TL intensity is highest for Cu doped LTB single crystal. TL counts per pass per mg per mA were calculated and it has been observed that TL count is highest for copper doped LTB single crystal. Calculated count values are 12.5,138, 2215 respectively for undoped, Mn doped and Cu doped LTB single crystal.

A. Determination of order of kinetics

Symmetry factors of the glow curve of different samples were calculated from the formula $\mu = \delta/\omega$, where $\delta = T_2 - T_m$ (upper temperature half width) and $\omega = T_2 - T_1$ (peak width at half maxima). T_1, T_2 and T_m were taken from each peak of glow curve of different samples and symmetry factors were determined. Values are tabulated in table 5.8 and table 5.9.

Table 5.8 Calculated symmetry factor for Mn doped LTB single crystal from glow curve

Mn: LTB	**1st peak**	**2nd peak**
T_1 (in °C)	**135 +/- 0.1**	**254.8 +/- 0.1**
T_2 (in °C)	**183 +/- 0.1**	**298.3 +/- 0.1**
T_m (in °C)	**163.5 +/- 0.1**	**279.7 +/- 0.1**
$\tau = T_m - T_1$ (in °C)	**28.5 +/- 0.2**	**24.9 +/- 0.2**
$\delta = T_2 - T_m$ (in °C)	**19.5 +/- 0.2**	**18.6 +/- 0.2**
$\omega = T_2 - T_1$ (in °C)	**48 +/- 0.2**	**43.5 +/- 0.2**
$\mu = \delta/\omega$	**0.406+/-0.005**	**0.427 +/-0.005**

Table 5.9 Calculated symmetry factor for Cu doped LTB single crystal from glow curve

Cu: LTB	**1st peak**	**2nd peak**
T_1 (in °C)	**94.9 +/- 0.1**	**185.2 +/- 0.1**
T_2 (in °C)	**129.1 +/- 0.1**	**235.5 +/- 0.1**
T_m (in °C)	**112.5 +/- 0.1**	**208.6 +/- 0.1**
$\tau = T_m - T_1$ (in °C)	**17.6 +/- 0.2**	**23.4 +/- 0.2**
$\delta = T_2 - T_m$ (in °C)	**16.6 +/- 0.2**	**26.9 +/- 0.2**
$\omega = T_2 - T_1$ (in °C)	**34.2 +/- 0.2**	**50.3 +/- 0.2**
$\mu = \delta/\omega$	**0.485+/-0.008**	**0.535+/-0.006**

Here Mn: LTB single crystal following first order kinetics and Cu:LTB following second order kinetics. Therefore we can say that the retraping is there in case of Cu doped LTB single crystal, which confirms the presence of multiple trap centers.

B. Determination of activation energy and frequency factor

Activation energies were calculated from initial rise method. In graph, ln(I) Vs 1/T were plotted for different samples. Fig 5.25 shows the plot of ln (I) Vs 1/T for peak I of undoped LTB single crystal. Fig 5.26(a) and 5.26(b) shows plot of ln (I) Vs 1/T for peak I and peak II of Mn doped LTB single crystal. Fig. 3.27(a) and 3.27(b) shows plot of ln(I) Vs 1/T for peak I and peak II of Cu doped LTB single crystal. Calculated activation energy and frequency factor are given in table 5.10. It has been observed that activation energy is highest for Mn doped LTB single crystal and lowest for undoped LTB single crystal.

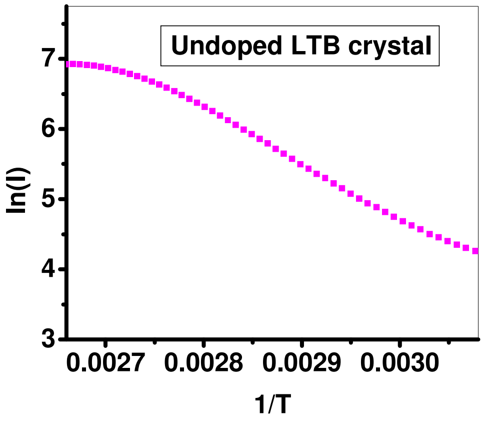

Fig. 5.25 Plot of ln(I) Vs 1/T for undoped LTB single crystal for peak I

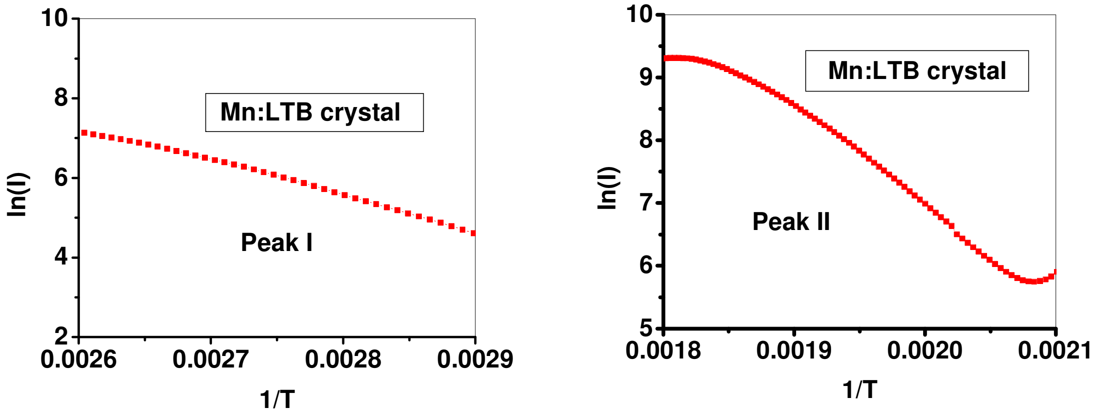

(a) (b)

Fig. 5.26 Plot of ln(I) Vs 1/T for Mn doped LTB single crystal of (a) peak I and (b) peak II

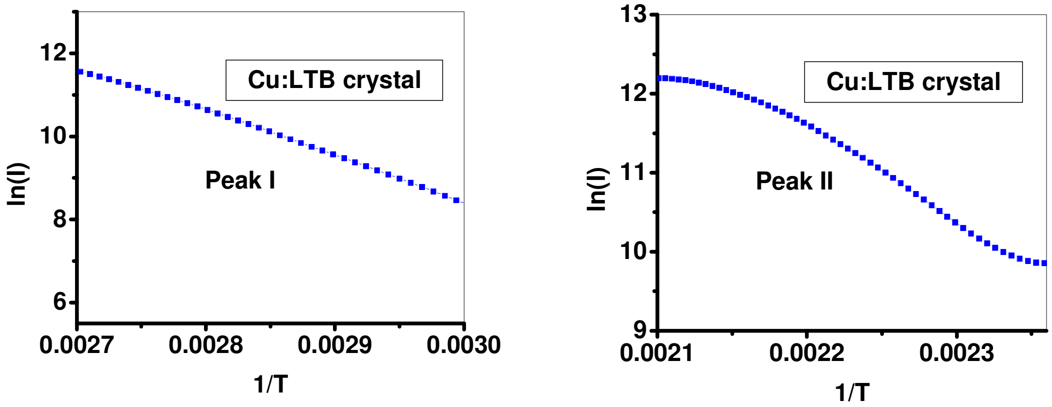

(a) (b)

Fig. 5.27 Plot of ln(I)Vs 1/T for Cu doped LTB single crystal for (a) peak I and (b) peak II

Table 5.10 Activation energy and frequency factor of undoped, Mn doped and Cu doped single crystal

	E_1 (eV)	S_1 (per sec)	E_2 (eV)	S_2 (per sec)
Undoped LTB	**0.72 +/-0.01**	**7.2 X10^8**	**-----------**	**------------**
Mn doped LTB	**1.0 eV +/-0.01**	**4.4 X10^{11}**	**1.28 +/-0.01**	**4.6X10^{10}**
Cu doped LTB	**0.92 eV +/-0.01**	**1.6 X10^{11}**	**1.16 +/-0.01**	**1.6 X10^{11}**

5.6 Comparison of TL intensity of undoped LTB, Mn doped LTB and Cu doped LTB single crystal, poly crystal and glass samples

TL characteristics of X-ray irradiated undoped, Mn doped and Cu doped LTB samples were studied and compared in different form (single crystal, poly crystal and glass). It has been observed that Cu doped LTB single crystal is giving highest TL count. TL counts of doped and undoped LTB glass, polycrystalline pallet and single crystals per pass per mg per mA are given in table 5.11.

Table 5.11 TL counts of doped and undoped LTB glass, polycrystalline pallet and single crystals per pass per mg per mA

Sample	**TL counts per pass per mg per mA**
Undoped LTB glass	**7**
Mn LTB glass	**15**
Cu LTB glass	**31**
Undoped LTB polycrystal	**12.5**
Mn LTB polycrystal	**38**
Cu LTB polycrystal	**50**
Undoped LTB single crystal	**12.5**
Mn doped LTB single crystal	**138**
Cu LTB single crystal	**2215**

References:

1. K. Mahesh, P. S. Weng, C. Furetta, Thermoluminescence in Solids and Its Applications, Nuclear Technology Publishing, Ashford, Kent, England, 1989.

2. C. P. Furetta, Nucl. Instrum. Methods in Phys. Res. 411 (2000) 417.

3. T. D. Cuong, Proceedings of the Ninth Asia Pacific Physics Conference, Hanoi,Vietnam, 2004.

4. E. Pekpak, A. Yılmaz, G. Özbayo˘glu, J. Alloys Compd. 509 (2011) 2466.

5. M. Prokic, Radiat. Prot. Dosim. 100(1-4) (2002) 265.

6. Z. Xiong, Z. Q. Tang, Chinese Science Bulletin (2007) 1776.

7. M. Prokic, Radiat. Meas. 33(4) (2001) 393.

8. H. G. Giesber, Information Sciences (2003) 61.

9. M. Ishii, Y. Kuwano, S. Asaba, T. Asai, M. Kawamura, N. Senguttuvan, T. Hayashi, M. Koboyashi, M. Nikl, S. Hosoya, K. Sakai, T. Adachi, T. Oku, H. M. Shimizu, Radiat. Meas. 38 (2004) 571.

10. J. Krogh-Moe, Acta Crystallographica 15 (1962) 190.

11. G. Corradi, V. Nagirnyi, A. Kotlov, A. Watterich, M. Kirm, K. Polgár, A. Hofstaetter, M. Meyer, J. Phys: Condensed Matter 20 (2008) 025216 (9 pp).

12. G. Herzberg, Infrared and Raman Spectra of Polyatomic Molecules, Van Nostrand, New York, 1945.

13. A. F. Murray, D. J. Lockwood, J. Phys. C: Solid State Physics 9 (1976) 3691.

14. G. L. Paul, W. Taylor, J. Phys. C: Solid State Physics 15 (1982) 1753.

15. G. Kitis, C. Furetta, M. Prokic, V. Prokic, J. Phys. D: Appl. Phys. 33 (2000) 1252.

16. D. Podgo´rska, S. M. Kaczmarek, W. Drozdowski, M. Berkowski, A.Worsztynowicz, Acta Phys. Pol. A 107 (2005) 507.

17. N. Senguttuvan, M. Ishii, M. Shimoyama, M. Kobayashi, N. Tsutsui, M.Nikl, M. Dusek, H. M. Shimizu, T. Oku, T. Adachi, K. Sakai, J. Suzuki, Nucl. Instrum. Methods .Phys. Res. A 486 (2002) 264.

18. M. Ishii, Y. Kuwano, T. Asai, N.Senguttuvan, T. Hayashi, M. Kobayashi, T.Oku, K. Sakai, T. Adachi, H. M.Shimizu, J. Suzuki, J. Cryst. Growth 257 (2003) 169.

19. M. Ignatovich, V. Holovey, A.Watterich, T. Vidoczy, P. Baranyai, A. Kelemen, V.

Ogenko, O. Chuiko, Radiat. Meas. 38 (2004) 567.

20. M. Kayhan, A. Yilmaz, J.Alloys Compd. 509 (2011) 7819.

21. E . Pekpak, A. Yilmaz, G. Ozbayoglu, J.Alloys. Compd. 509 (2011) 2466.

22. M. Prokic, Radiat. Prot. Dosim.100 (2002) 265.

23. M.Takenaga, O.Yamamato, T. Yamashita, Preparation and characteristics of $Li_2B_4O_7$:Cu phosphor, Nucl. Instru. Methods 175 (1980) 77.

24. S. W. S. Mc Keever, Thermoluminescence of Solids (Cambridge University Press) 1985.

25. R. Chen, and S. A. A . Winer, J. Appl. Phys. 41**,** 5227 (1970).

26. R. Komatsu, T. Sugawara, K. Sassa, N. Sarukura, Z. Liu, S. Izumida, Y. Segwa, and K. Yamanouchi, Appl. Phys. Lett.**70,** 3492 (1997).

27. I. Magdalyna, F. Mauro, K. Andras, Rad. Phys. and Chem. 81 (2012) 1528-1532.

28. R. Chen, S. W. S. Mckeever, "Theory of thermoluminescence and related phenomena" World Scientific, 1997.

Chapter 6

Synthesis and Characterization of Lithium Niobate and Lithium Tetraborate Nanoparticles

6.1 Introduction

In last decade, researcher has focused on the synthesis of nanomaterials due to their important properties, which comes from the dimensional confinement. Nano material has great potential for device applications. It is reported that pyroelectric coefficient of ferroelectric increases with decrease in particle size. By using pyroelectric properties, waste heat can be converted into electrical signal to power tiny devices [1]. Pyroelectric nano generators are extremely useful for powering specific task in the biological application. Lithium niobate nano composite can also be used for piezoelectric power generation. It is possible to transfer the beneficial properties of small NLO crystal to hybrid material by embedding them in easily processable polymers [2]. It is also possible to increase both non linear optical and photo refractive properties using a nanocomposite material. Lithium niobate nanocrystal can be incorporated in to glass or polymer to achieve large interaction length for frequency conversion. Photorefractive properties can be enhanced by embedding the nano crystal into a host material with large effective electro optic coefficient. Many researchers reported that the photo-conductivity of poly N vinyle carbazole doped with lithium niobate nanoparticles increases remarkably with the nanoparticles content. The reason for this enhancement is an increase in the effective photo hole lifetime due to trapping of electrons on the nanoparticles and creation of recombination barrier at the polymer nanoparticle interface [3]. Nanocrystalline particles embedded into a suitable host matrix leads to modify optical or mechanical properties [4, 5]. It has been reported that the oxide nanoparticles are promising for photonics applications [6, 7]. LN nanoparticles are also useful in biological application. Lithium niobate nanoparticles doped with iron can be used for killing cancer cell by using photo induced voltage due to photovoltaic effect [8]. Lithium niobate nanocrystals have ability to label cancer cells and other functional cell lines due to their unique double-frequency property and it is recently reported that LN nanocrystals can be used as SHG labels for imaging stem cells [9]. It has been proved that LN nanocrystals can be used as a cytocompatible, near-infrared (NIR) light driven cell label for long-term imaging. This will enhance the use of LN nanocrystals in different biological application like deep-tissue tracking, remote drug delivery and stem cell therapy. On the other hand, lithium tetraborate is a very good tissue equivalent TLD material. In recent years, intensive research focuses on the synthesis of nano-sized phosphors due to better radiation resistance, wide range linearity [10], less fading and detection of high energy ionizing radiations [11] which cannot be obtained with conventional macroscopic materials. In view of the importance of these two materials in nano form it was thought to synthesis lithium niobate and lithium tetraborate nanoparticles and characterize.

6.2 Synthesis and characterization of lithium niobate nanoparticles

6.2.1 Synthesis of lithium niobate nanoparticles by high energy ball milling

Lithium niobate is generally synthesized from lithium carbonate and niobium penta-oxide. To synthesize lithium niobate, stoichiometric amount of both chemicals were taken as per chemical reaction given below.

$$\mathbf{Li_2CO_3 + Nb_2O_5 = 2\ LiNbO_3 + CO_2}$$

According to chemical reaction required amount of Li_2CO_3 and Nb_2O_5 were mixed properly in an agate mortar for an hour. After proper mixing, the mixture was placed in platinum crucible inside a resistive heating furnace and calcined for 24 hours at 950 ^{0}C. Then the chemical was taken out from the furnace and it was mixed again and placed inside the furnace again at same temperature for same time duration. This is done for the purpose of uniformity in reaction. In this process we obtain lithium niobate and carbon dioxide is released to the atmosphere. The material, prepared by solid state reaction is divided into two parts to put it into containers. These containers are then kept inside the high energy ball milling machine (Fritsch make pulverisette 7). Photograph of machine is shown in figure 6.1. For wet grinding, ethyl alcohol is used as a grinding medium and oleic acid is used to prevent agglomeration of nanoparticles. We have taken different ball to powder mass ratio to prepare nanoparticles. For 20 gm of lithium niobate powder, different amount of zirconia balls were taken to vary the ball to powder mass ratio. 12 ml alcohol along with 2 ml oleic acid was put in each container. Oleic acid is added to prevent agglomeration.

Fig. 6.1 Photograph of high energy ball milling machine

Milling was done for different time with same rpm. Several run were performed to get nano size particles. As the speed of machine is very high during rotation, temperature of the bowl may increase very much. To avoid this, pause time is required in between two rotation cycle. Pause time was set as 5 min for every cycle. Speed (rpm) of machine and total time of milling for different run are given in the table 6.1.

Table 6.1 Milling parameters for preparation of lithium niobate nanoparticles

S. No.	Speed (in rpm)	Total time (hr)	BPMR	Pause time	Milling media
1.	500	4	1:1	5 min	Ethanol and oleic acid
2.	500	8	2:1	5 min	Ethanol and oleic acid
3.	700	4	2:1	5 min	Ethanol and oleic acid
4.	700	8	2:1	5 min	Ethanol and oleic acid
5.	700	12	2:1	5 min	Ethanol and oleic acid
6.	700	20	2:1	5 min	Ethanol and oleic acid

6.2.3 Characterizations of lithium niobate nanoparticles

A. X-ray diffraction study

The crystalline phase of the ball milled lithium niobate powder was determined by powder X-ray diffraction (XRD). X-ray diffraction of ball milled powder is shown in figure

6.2. It has been observed that the peak is broadening as we increase the milling time. The average crystallite size was calculated from (012) diffraction peak using Scherrer's equation:D = 0.9λ / (β cos θ), where D is average crystallite size in mm, λ is the wavelength of X-ray source (0.15418 nm), β (in radian) is full width at half maximum of the peak. Here β is measured after subtracting the instrumental broadening. The calculated average crystallite size were approximately 30 nm, 25 nm, 22 and 21 nm for the samples milled at 700 rpm, for 4 h, 8 h, 12 h and 20 h respectively. It has been observed that crystallite size going to saturate as we increase the milling time. This is because the grain size reduction is controlled by minimum distance between dislocations, Dc. When grain size is in the Dc range, dislocation become unstable and it come out from the grains. This phenomenon inhibits any further grain size reduction.

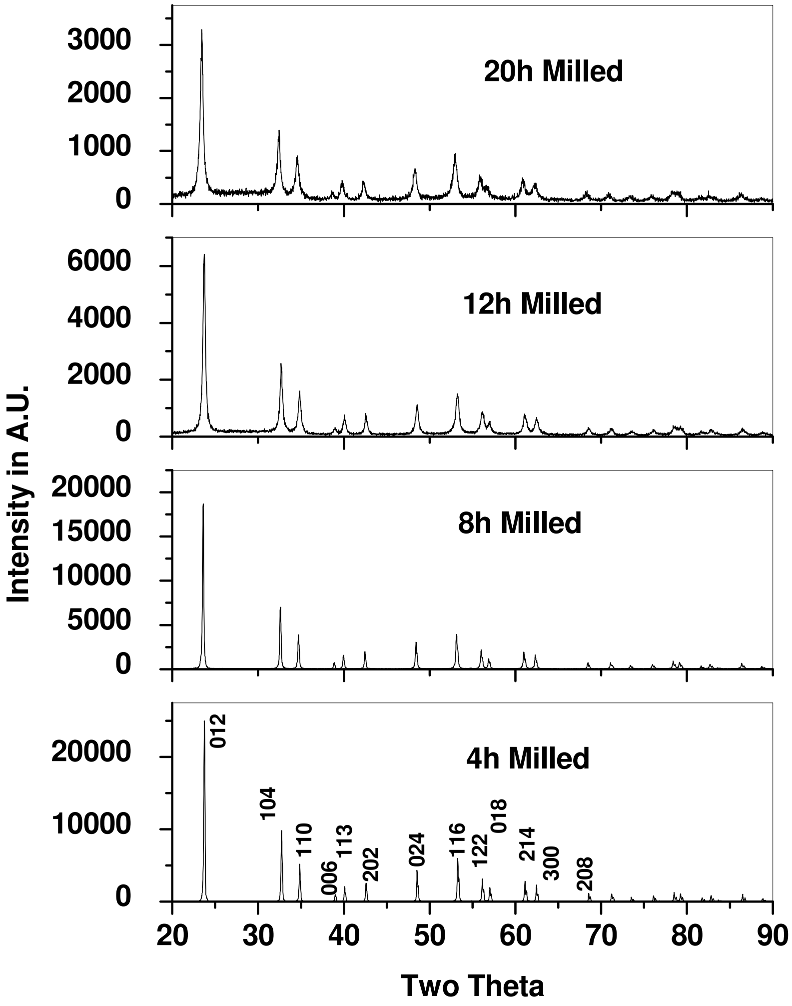

Fig. 6.2 XRD pattern of high energy ball milling at different milling time

B. Dynamic light scattering study

The synthesized LN nanoparticles were examined in Zetasizer nanoseries to study particle size distribution by dynamic light scattering technique. LN nanoparticles were suspended in water and ultrasonication was done for uniform dispersion. The representative particle size distribution for the LN samples ball milled at 700 rpm for 8 h is shown in figure 6.3. Particle size of lithium niobate powder ball milled at 700 rpm and 8 h is around 57 nm. Distribution shows that size of 95% particles lies in this range.

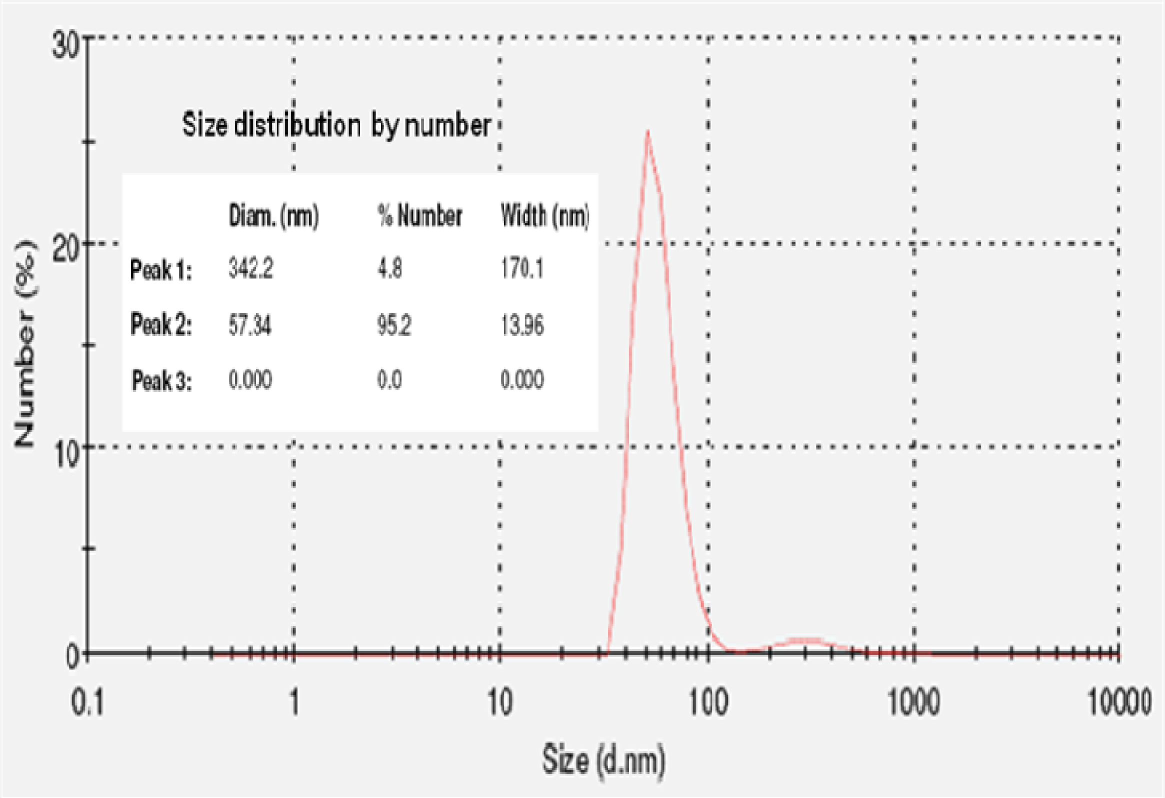

	Diam. (nm)	% Number	Width (nm)
Peak 1:	342.2	4.8	170.1
Peak 2:	57.34	95.2	13.96
Peak 3:	0.000	0.0	0.000

Fig. 6.3 DLS study of lithium niobate nanoparticles

C. Scanning electron microscopy study

Scanning electron microscopy (SEM) was used to study the morphology and textural properties of the ball milled powders. SEM micrograph taken for $LiNbO_3$ nanoparticles ball milled at 700 rpm for 8 hour is shown in figure 6.4.

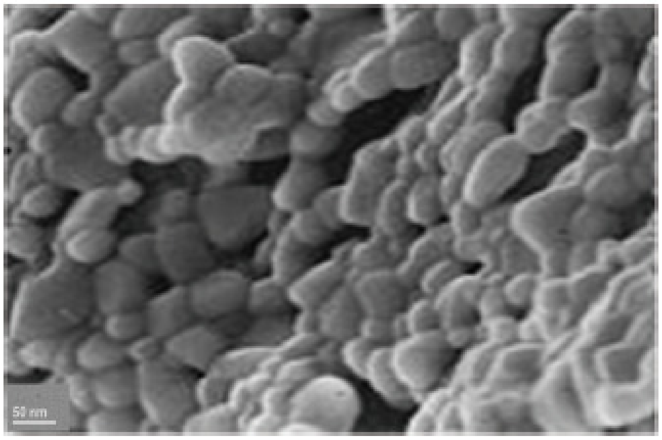

Fig. 6.4 SEM images of $LiNbO_3$ nanocrystals ball milled at 700 rpm for 8h

This SEM image shows highly agglomerated particles having some voids. Image also shows that the particles are irregular in shape, with a variation in morphology and the sizes.

D. Transmission electron microscopy study

Figure 6.5 (a, b) shows the TEM micrographs taken for the samples of $LiNbO_3$ nanoparticles ball milled at 700 rpm for 8 h in normal image and high-resolution mode. The corresponding selected area diffraction (SAED) patterns are inserted into the micrograph. The TEM micrograph showed in figure 6.5 (a) reveals the formation of nanoparticles with varying sizes.

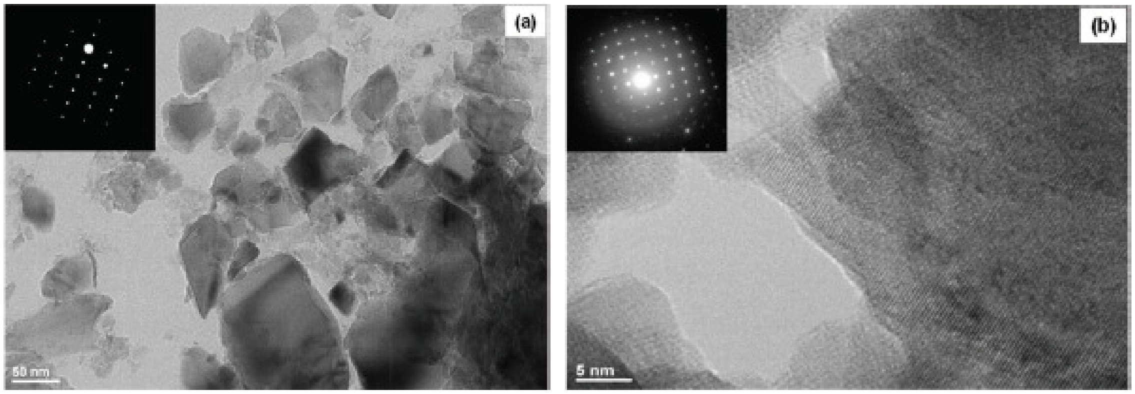

Fig. 6.5 TEM images of $LiNbO_3$ nanocrystals ball milled at 700 rpm for 8 h in (a) normal image and (b) high resolution mode. The corresponding SAED patterns are inserted into the micrographs

The particle sizes are mostly in ~30-60 nm range, and very few are above 100 nm. These sizes of the particles are sufficient to diffract and produce SAED pattern. The sharpness of the spots suggests formation of pure LN phase, there is no secondary phase in the sample. The high-resolution electron micrograph (HRTEM) for the same sample is shown in figure 6.5 (b). The clear lattice fringes in the HRTEM micrograph shows that the highly ordered and defect free single phase particles are formed. The lattice fringes further suggests that there are negligible crystalline defects at micro-structure level. This is further supported by the SAED pattern inserted into the HRTEM micrograph in figure 6.5 (b). The above TEM results in diffraction and high-resolution image mode suggest the successful preparation of LN nanoparticles with the particle sizes ranging ~30-60 nm.

E. UV-VIS transmission spectra study

To measure transmission spectra LN nanoparticles milled for 8hr at 700 rpm were suspended in de-ionized water and ultra sonication was done for uniform dispersion. Both transmission spectra of lithium niobate nanoparticles and bulk are shown in figure 6.6 (a) and 6.6 (b).

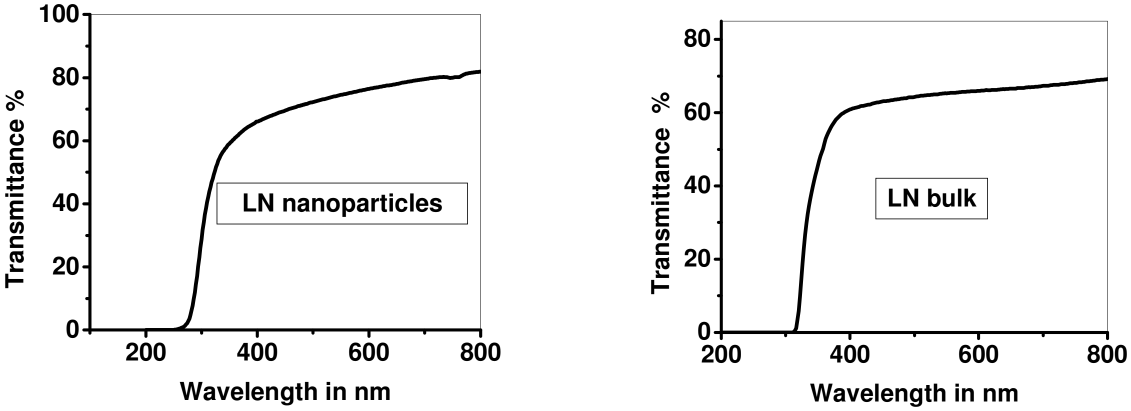

(a) **(b)**

Fig. 6.6 Transmission spectra of (a) LN nanoparticles (b) bulk crystal

It was observed that the UV cutoff of the nanoparticles of $LiNbO_3$ was shifted towards the lower wavelength (blue-shift) with compare to bulk. This implies that the band gap increases for nano size lithium niobate, which is due to quantum confinement.

F. Second harmonic generation study of lithium niobate nanoparticles dispersed in glass

Lithium niobate nanoparticles were dispersed in lithium tetraborate glass for SHG study. LTB glass with different nano particle concentration was prepared. Glass was prepared by melt quenching technique. The photograph of nanoparticles dispersed glass with different concentration (0.1wt%and 0.2 wt %) are shown in figure 6.7.

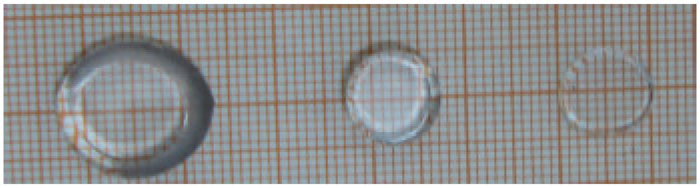

Fig. 6.7 LN nanoparticles dispersed LTB glass

Transmission spectra of nanoparticle dispersed LTB glass are shown in figure 6.8. It has been observed that transmittance decreases as we increase the LN nanoparticles concentration.

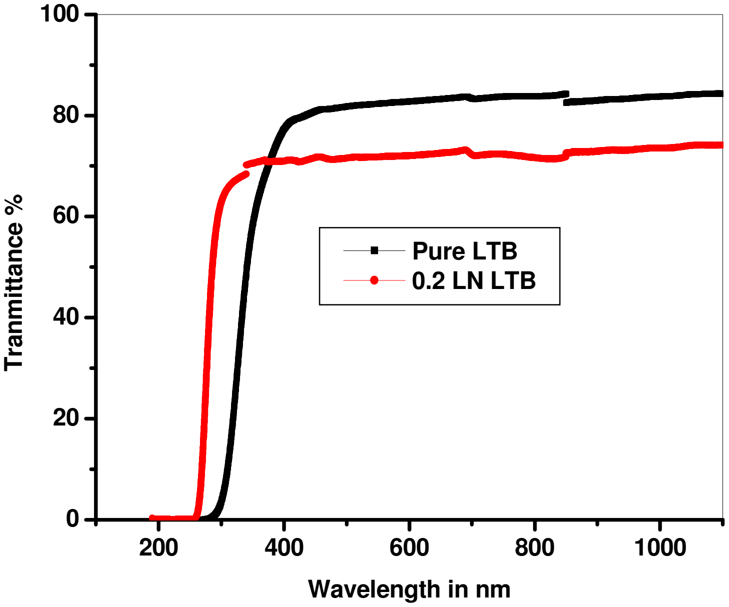

Fig. 6.8 Transmission spectra of lithium niobate nano particle dispersed in LTB glass

Second harmonic generation (SHG) studies were carried out for the lithium niobate nano particles dispersed in glass. For this purpose, a Nd: YAG laser of 7 ns pulse width was used. The laser has facility to vary pules energy 50-100 mJ. Ray diagram of SHG setup is shown in figure 6.9. The generated SHG signal was isolated from fundamental beam at 1064 nm using a KG 5 filter and subsequently passed through a monochromator set at 532 nm. The second harmonic signal was amplified using a PMT with high voltage power supply and the signal was recorded at an oscilloscope. Significant SHG signal was observed. Photograph of SHG setup and measured SHG signal is shown in figure 6.10(a) and 6.10(b) respectively.

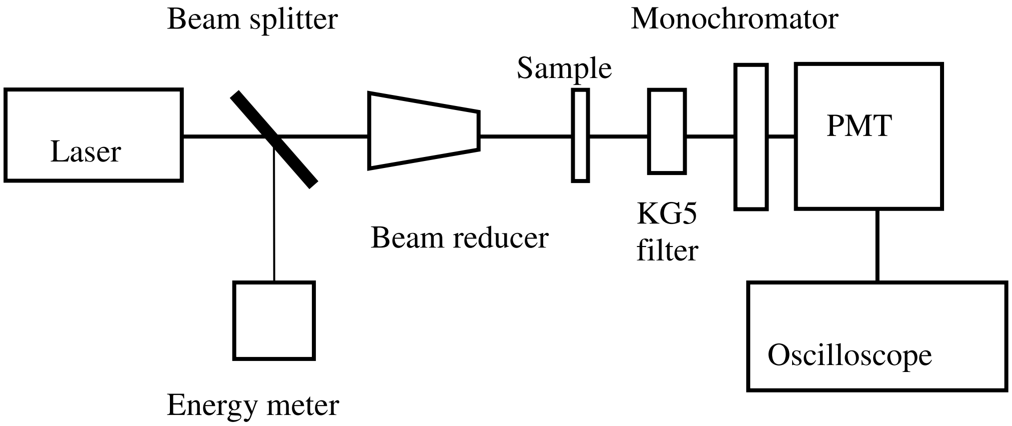

Fig. 6.9 Block diagram of SHG setup

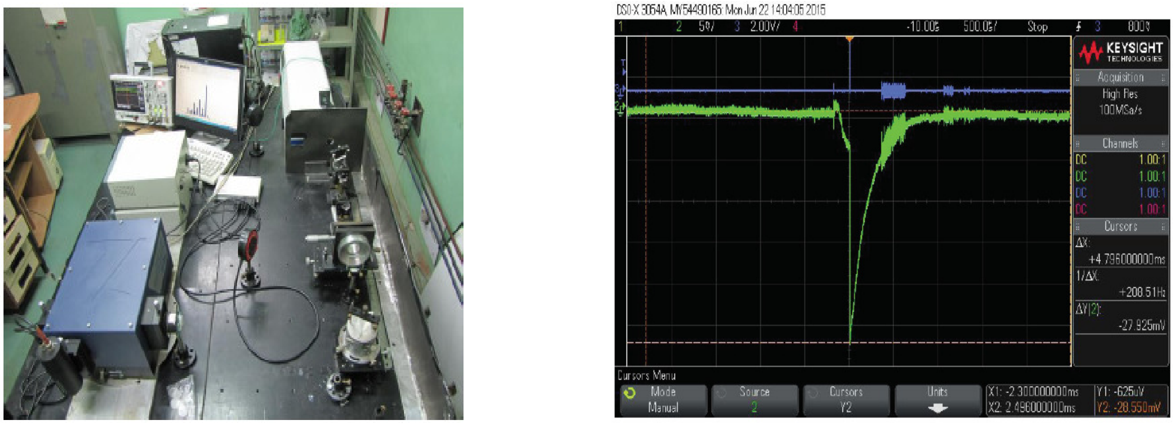

(a) **(b)**

Fig. 6.10 Photograph of (a) SHG setup (b) Measured SHG signal

The results show that the there is a small peak corresponding to the SHG generated from the LN nanoparticles. However, the signal obtained is very weak. It might be due to random orientation of LN nanoparticles. To enhance SHG signal oriented nanoparticles and further optimization is required.

6.3 Synthesis and characterization of lithium tetraborate (LTB) nanoparticles by high energy ball milling

6.3.1 Synthesis of lithium tetraborate nanoparticles

Stoichiometric composition of Li_2CO_3 and B_2O_3 were used to prepare $Li_2B_4O_7$ powder. Two chemicals were mixed for 1h in agate mortar. 0.2 Mole % CuO was added to the mixture to get Cu doped lithium tetraborate. The mixture was then milled for 1h at the rate of 300 rpm in a high energy ball mill. Homogeneously mixed powder was filled in a platinum crucible and was kept in the furnace and heated up to 400 °C at the heating rate of 100 °C per hour and kept for 3h. This powder was removed from the crucible and again mixed in an agate mortar for 1h. This mixture was kept in a platinum crucible again and annealed at 750 °C for 10h. In this process the single phase LTB polycrystalline powder was obtained. The material, prepared by solid state reaction was weighed and divided into 2 parts to put it into ball mill containers. For wet grinding, ethyl alcohol is used as a grinding medium. Milling was done for different milling time with milling speed 500 r.p.m. As the speed of machine is very high during rotation, temperature of the bowl may increase abruptly. To avoid this, pause time is required in between two rotation cycles. Pause time was set as 5 min for every cycle. Ball to powder mass ratio (BPMR) is also an important factor to reduce the particle size. In our experiment BPMR was kept 2:1. Milling is done for different time duration 5h, 10h and 15h. After milling, the powder was taken out for characterizations.

6.3.2 Characterizations of Cu:LTB nanoparticles prepared by high energy ball milling

A. X-ray diffraction study

X-ray diffraction was used to identify the crystalline phases and to estimate the crystallite size. The synthesized nanoparticles were examined by powder X-ray diffraction using Cu $K\alpha_1$ radiation ($\lambda = 1.5418716$Å, Rigaku Geiger Flex X-ray diffractometer). The XRD patterns were obtained with 2θ in the range of 20 to 70 degree by step scanning, using 2θ increment of 0.010. All peaks of X-ray diffraction are matching with known data (JCPDS). XRD pattern of 5h, 10h and 15 h milled LTB powder is shown in figure 6.11. It has been observed that as we increase the milling time XRD peaks become broader. From the powder

XRD pattern effective crystallite size was calculated using full width half maxima (FWHM) approach on the line broadening of XRD peaks. The apparent crystallite size D was calculated from the relation D=λ/B Cos θ_B , where λ is the wavelength used and B is the broadening. Calculated size was approximately 40 nm.

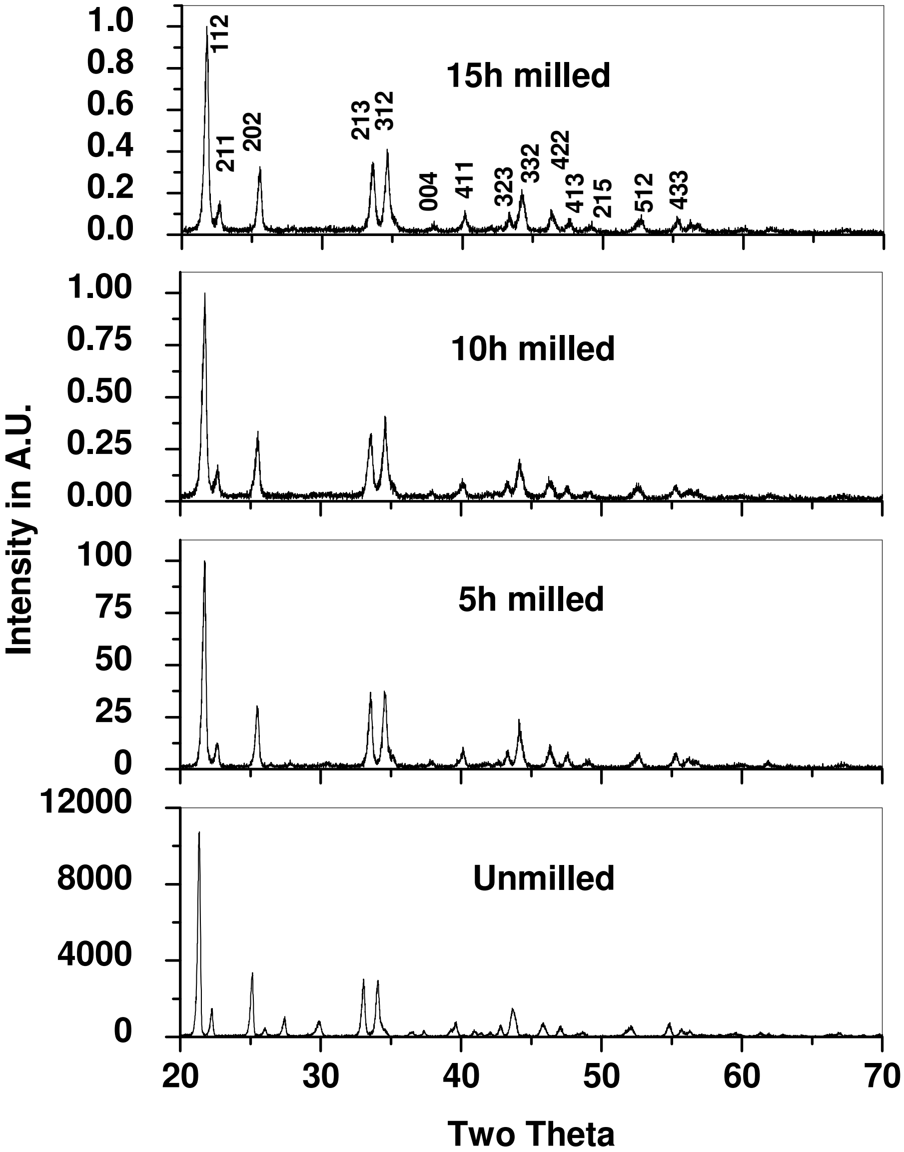

Fig. 6.11 XRD pattern of ball milled Cu: LTB powder

B. Transmission electron microscopy study

The powder samples were dispersed in ethanol for TEM study. TEM micro graph of LTB nanoparticles are shown in figure 6.12. The TEM study is useful tool to know about the local structure and the particle size of the nanomaterials. It can be seen through the picture that particle size is varying from 200 nm to 1 μm. It has been observed that particle size calculated from TEM analysis is much bigger than the crystallite size. This is because in a single particle many crystalline particles are present. All crystallite are not separate.

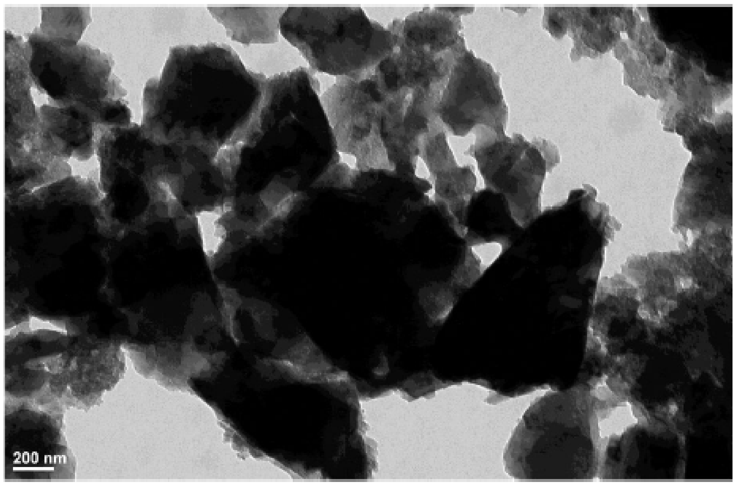

Fig. 6.12 TEM micrograph of LTB nanoparticles

C. Dynamic light scattering study

The synthesized lithium tetraborate nanoparticles were examined by Zetasizer nano series to study particle size distribution. Lithium tetraborate nanoparticles were suspended in acetone and ultrasonication was done for uniform dispersion. In dynamic light scattering method dynamic fluctuations of light scattering intensity is measured. Due to Brownian motion of the particle dispersed in a liquid medium fluctuation in concentration of particle occur within the medium. This causes local inhomogeneities of the refractive index and as a consequence fluctuation of intensity of the scattered light occurs. The representative particle size distribution for the lithium tetraborate sample ball milled for 15 hrs at 500 rpm is shown in figure 6.13.

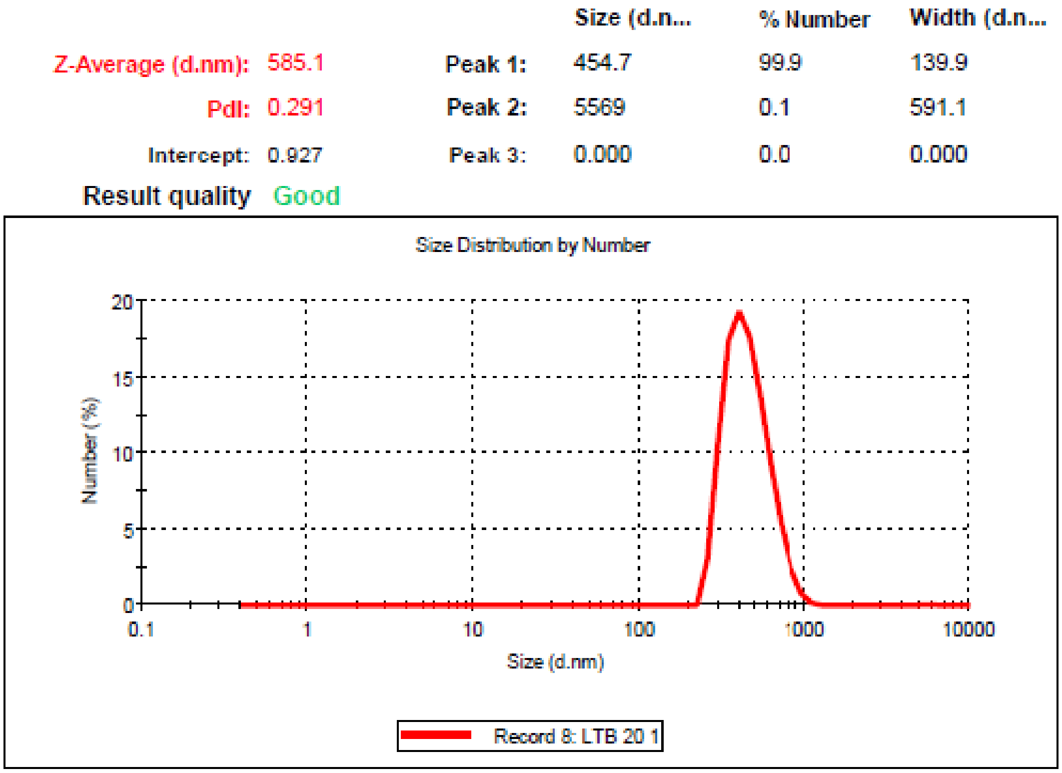

			Size (d.n...	% Number	Width (d.n...
Z-Average (d.nm):	585.1	Peak 1:	454.7	99.9	139.9
PdI:	0.291	Peak 2:	5569	0.1	591.1
Intercept:	0.927	Peak 3:	0.000	0.0	0.000

Result quality Good

Fig. 6.13 Size distribution of lithium niobate nanoparticle

Particle size of lithium tetraborate powder is around 454 nm. Distribution shows that size of 99% particles lies in this range.

D. Thermoluminescence study

Thermoluminescence study of LTB nanoparticle prepared by high energy ball milling was done. Pallets were prepared from LTB nanoparticles and were irradiated through ionizing radiation. TL glow curve of irradiated pallet made from LTB nanoparticles were taken through TL reader analyzer and compared with that of polycrystalline sample. TL glow curve of Cu doped LTB pallet made from polycrystal and nanoparticles are shown in figure 6.14 (a) and 6.14(b) respectively. It has been observed that TL intensity decreases almost 7-8 times in case nanocrystalline sample with respect to polycrystalline sample irradiated with same dose. Decrease of TL intensity in nanocrystalline sample is due to increase of surface to volume ratio. In case of nanoparticle energy storage capacity is less as number of unit cell in a grain is very less. Again in nanocrystals surface barrier energy is very high, hence low dose of ionizing radiation is unable to produce significant defect state to produce TL [12]. It is also reported by some researcher that in nano structured material energy levels bands are altered or reorganized due particle size effect and some time due to absence of crystal field effect [13, 14].

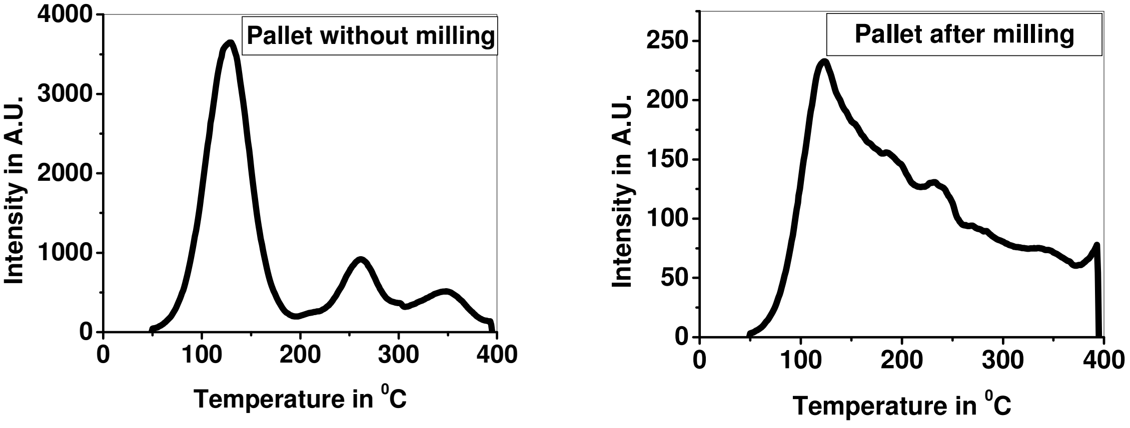

(a) (b)

Fig. 6.14 TL glow curve of Cu: LTB (a) polycrystalline pallet and (b) pallet of nanoparticles

6.4 Synthesis and characterizations of lithium tetraborate nanoparticles by melt quenching technique

6.4.1 Synthesis of lithium tetraborate nanoparticles by melt quenching technique

Lithium tetraborate ($Li_2B_4O_7$) is congruently melting with a melting point at 917 °C. The synthesis of Mn doped and Cu doped $Li_2B_4O_7$ glass was carried out from in platinum crucibles in air. Initially solid state synthesis was done. Then temperature of solid state reacted powder was raised to melting point. After melting compound was overheated to 1000 °C to remove traces of water and carbon dioxide, which were present in the melt. The platinum crucible containing the mixture covered with a lid was placed in a furnace. Homogenized melt was then poured into preheated stainless steel plate and pressed it by another steel plate. The flat glass plates of dimensions 20–25 mm, and 1–2 mm thicknesses were obtained. Glass samples are shown in figure 6.15. Quenched glass samples were polished properly by alumina powder. The glass samples were annealed at various temperatures 450°C, 470°C, 490°C, 570°C for 4-5 hr to get nanocrystalline sample.

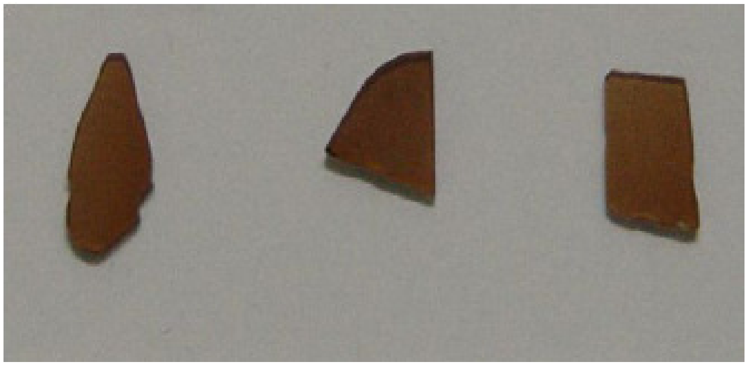

Fig. 6.15 Photograph of quenched LTB glass

6.4.2 Characterization of lithium tetraborate nanoparticles by melt quenching technique

A. X-ray diffraction study

The evolution of the crystalline structure of the LTB glass samples during the annealing process was recorded using powder X-ray diffraction (XRD). 18 kW RIGAKU X-ray generator with Cu K_α wavelength 1.5418Å was used for X-ray diffraction experiment. The diffraction patterns were taken for 2θ scan from 20 degree to 70 degree with a step of 0.02 degree. Figure 6.16 shows the XRD patterns taken for LTB glass samples annealed at various temperatures. It is clear from the XRD patterns that the as quenched sample and the sample annealed at up to 470°C are amorphous. After this temperature it has started showing the faint peaks for crystalline phase. This clearly indicates that after certain temperature randomly oriented atoms starts arranging in periodic order. XRD patterns taken at higher temperatures show the crystalline structure with single phase. However the grain size started increasing with higher annealing temperature as was expected. The well-resolved peaks are matching with JCPDS data for $Li_2B_4O_7$. From powder X-ray diffraction pattern the effective crystallite size was calculated using full width half maxima (FWHM) approach on line broadening of XRD peaks. In a single line analysis the apparent crystallite size D was calculated from the relation $D=\lambda/\beta \cos\theta_B$. During measurement broadening due to instrument has been deducted. Crystallite size was found in the range of 20-30 nm.

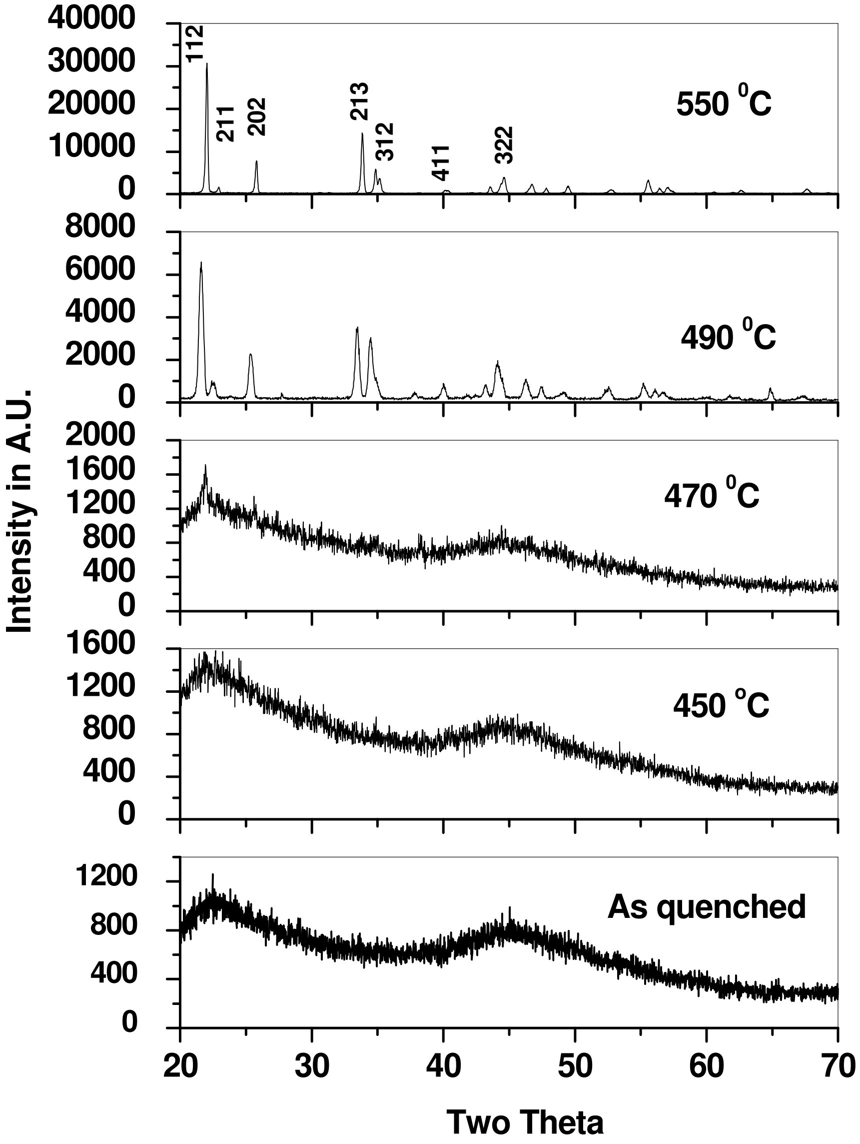

Fig. 6.16 XRD pattern of LTB glass annealed at different temperature

B. Scanning electron microscopy study

Scanning electron microscopy (SEM) was done on the glass samples to monitor the glassy surface and the crystallite sizes of the samples. Figure 6.17 shows the SEM micrographs taken from LTB glass samples annealed at 450°C and 570°C respectively. Figure 6.17 (a), the micrographs taken from the crushed sample annealed at 450°C shows the larger size lump with grains which are indicative of glassy phase. The crystallite sizes in figure 6.17 (b) observed were varying few tens of nm dispersed in glass matrix.

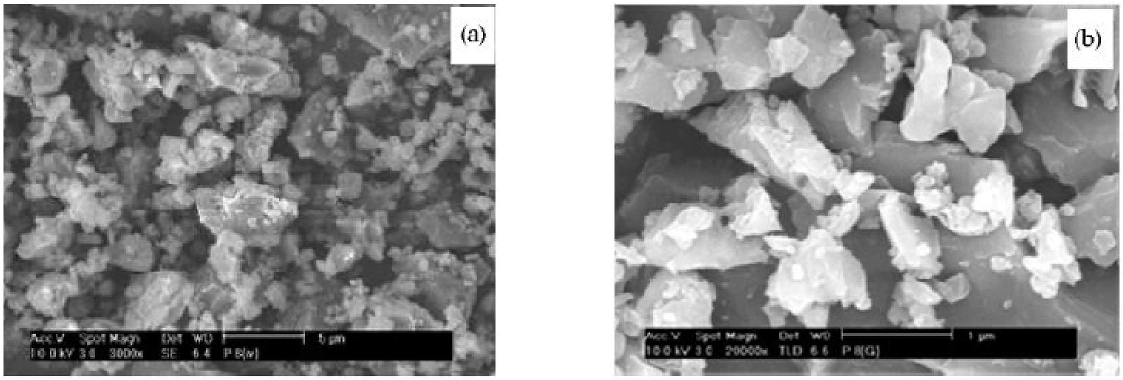

(a) (b)

Fig. 6.17 SEM micrograph for LTB sample annealed at (a) 450 °C and (b) 570 °C

C. Transmission electron microscopy study

High-resolution transmission electron microscopy (HRTEM) is a good tool to know the local structure, structural transformation and microstructural morphology of the polycrystalline material. HRTEM studies were conducted to investigate the microstructure and the crystalline size of the sample.

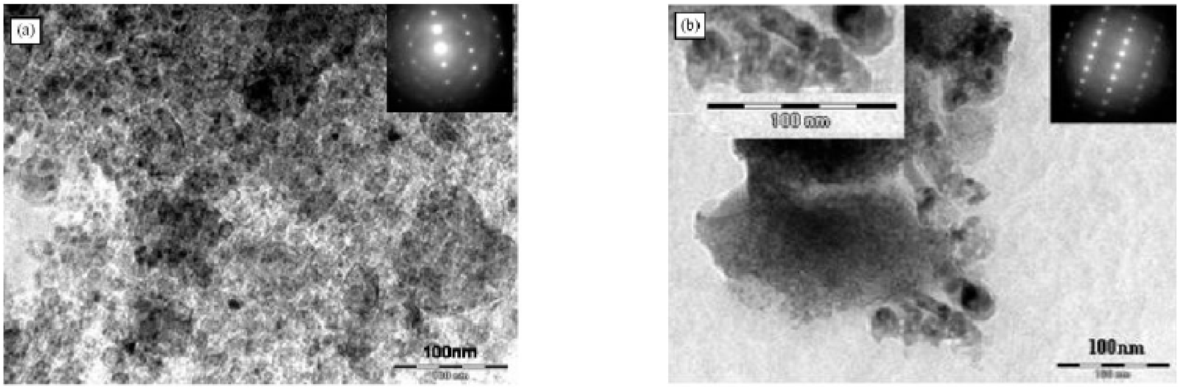

(a) **(b)**

Fig. 6.18 HRTEM bright field micrograph for the glass sample annealed at (a) 490 °C and (b) 570 °C

Figure 6.18 (a) and 6.18 (b) shows the representative HRTEM bright field micrograph for the glass samples annealed at 490°C and 570°C respectively. The micrograph shown in figure 6.18(a) is a clear indication of the transformation of the glass phase into polycrystalline phase. Inset in figure 6.18 (a) shows the corresponding selected area diffraction (SAD) pattern. The faint diffuse scattering along with the main diffraction spots in SAD pattern indicates that the crystallite sizes are of few nanometers. On the other hand the samples annealed at higher temperatures increases in crystallite size have clear diffraction spots (Fig. 6.18(b)). The nanoparticles are clearly seen in the micrograph. The crystalline sizes were measured about 20–30 nm. The clear spots in SAD pattern along with the diffuse rings are clear indication of nano-size crystalline particles with single phase. Figure 6.18(a) indicates the transformation of the glass phase into poly crystalline phase. The faint diffuse scattering along with the main diffraction spot in SAD pattern indicates that crystallite sizes are of few nm and fig 6.18 (b) shows increased crystallite size with clear diffraction spot.

References:

1. A. N. Morozovska, E. A. Eliseev, G. S. Svechnikov and S. V. Kalinin, J. Appl. Phys. 108 (2010) 042009.
2. E. Śliwińska, S. Mansurova, U. Hartwig, K. Buse, K. Meerholz, Appl. Phys. B 95 (2009) 519.
3. S. Mansurova, K. Meerholz, E. Sliwinska, U. Hartwig, K. Buse, Phys. Rev. B 79 (2009) 174208.
4. D. Psaltis, S. R. Quake, C. Yang, Nature 442 (2006) 381.
5. J. R. Adleman, H. A. Eggert, K. Buse, D. Psaltis, Opt. Lett. 31 (2006) 447.
6. A. Majchrowski, J. Ebothe, E. Gondek, K. Ozga, I. V. Kityk, A.H. Reshak, T. Łukasiewicz, J. Alloys & Compd. 485 (2009) 29.
7. Y. Djaoued, K. Ozga, A. Wojciechowski, A. H. Reshak, J. Robichaud, I. V. Kityk, J. Alloys & Compd. 508 (2010) 599.
8. A. Blázquez-Castro, J.C. Stockert, B. Lopez-Arias, A. Juarranz, F. Agulló, García-Cabañas and M. Carrascosa, Photochem.& Photobio. Sc. 10 (2011) 956.
9. J. Li, J.Qiu , W. Guo, S. Wang, B. Ma, X. Mou, M. Tanes, H. Jiang, H. Liu. Nano scale 8 (2016) 7416.
10. N. Khalilzadeh, E. B. Saion, H. Mirabolghasemi, J. Mater. Res. Technol. 5 (2016) 206.
11. V. S. Kortov, Radiat. Meas. 45 (3-6) (2010) 512.
12. L. Singh, V. Chopra, S. P. Lochab, J. Luminescence 131 (2011) 1177.
13. X. Gong, P. Wu, W.K. Chan, W. Chen, J. Phys. Chem. Solids 61 (2000)115.
14. M. Philip, Rep. Prog. Phys. 64 (2001) 297.

Chapter 7

Conclusions

Growth of good optical quality lithium niobate and lithium tetraborate crystal is very difficult. Major difficulties occur during growth of single crystals are crack formation, inclusions, etc. Crystals generally cracks during post growth cooling due to anisotropy in thermal expansion coefficient. Therefore optimizations of growth parameters are required. Various growth parameters such as pulling rate, rotation rate, axial temperature gradient above and below melt level, post growth cooling rate, crucible to crystal diameter ratio were optimized to grow good quality doped and undoped lithium niobate and lithium tetraborate crystal by Cz technique. Crack free, transparent and big size crystals were obtained. Grown crystals were characterized by XRD, HRXRD for phase identification and crystalline quality respectively. Optical quality of the grown crystal was checked by transmission spectra, birefringence interferometry and conoscopy pattern. Etching study of the grown crystal was performed to check the dislocation density. For the application point of view two special characterizations were performed on grown crystal. One is photo refractive study and other is thermoluminescence study.

As lithium niobate is a potential holographic material, photorefractive studies have been performed and various photorefractive parameters such as diffraction efficiency, recording time, erasing time, etc. were calculated. Proton exchange experiment was done on as grown doped lithium niobate sample. Photorefractive properties were studied on proton exchanged doped lithium niobate crystals. It has been observed that diffraction efficiency has been increased significantly in proton exchanged sample. Due to proton exchange, electro optic coefficient r_{33} of the crystal increases and as a result strong refractive index grating forms. This produces higher diffraction efficiency. Therefore proton exchange technique is useful for enhancing the photorefractive properties of the crystal.

Similarly as lithium tetraborate is a very efficient TLD material, thermoluminscence studies have been performed on undoped and doped lithium tetraborate crystal. Thermoluminscence glow curve were taken for irradiated samples. Different kinetic parameters such as order of kinetics, activation energy and frequency factors were calculated for doped and undoped lithium tetraborate (LTB) crystal. It has been observed from our study that the TL intensity of LTB single crystal is mass sensitive. Small variation of mass (0.1mg) gives very large changes in TL intensity. Therefore care has to be taken to measure the mass of TLD material for accurate measurement of absorbed dose. Total TL intensity per unit mass for same dose of undoped, Mn doped and Cu doped LTB samples were calculated. It has been observed that Cu doped LTB crystal produces highest TL intensity. Fading studies were also performed and 5 % fading was observed in single crystal sample. To compare thermoluminescence properties of single crystal with polycrystalline and glass form, TL studies was also performed on polycrystalline and glass sample. It has been observed that single crystal sample gives highest and glass sample gives lowest TL intensity.

In doped lithium tetraborate polycrystalline sample two well separated peaks were observed. We have proposed a new scheme for dual reading. As first peak fades very quickly, so this peak can be used for immediate dose measurement by heating the sample up to 210 °C without disturbing the second peak. After every irradiation, the dose may be measured separately by reading only first peak. The cumulative dose can be measured after a long time, say one or two months, by taking the TL glow curve in the temperature range of 50 to 320 °C. In this case only second peak will be observed in glow curve. It is hoped that this new method of multiple readout will revolutionize the use of TL detector for personnel dosimetry.

As it is known that the growth of single crystals is a costly and demanding exercise we have synthesized nanoparticle of lithium niobate and lithium tetraborate. Nanoparticles of these two materials were prepared by high energy ball milling and characterize for phase and particle size. Lithium niobate nanoparticles were dispersed in glass matrix and the SHG properties of the composite were investigated. Very weak SHG signal was observed. It might be due to random orientation of nanoparticles. To enhance SHG signal oriented nanoparticles and further optimization is required. Lithium tetraborate nanoparticles were used for making pallet for thermoluminescence study. It has been observed that the TL intensity decreases almost 7-8 times in case of nanocrystalline sample in compare to polycrystalline sample. This decrease in TL intensity is due to less energy storage capacity of nanoparticles. These nanoparticles can be used for high dose measurement.

Future scope

Proton exchanged Fe doped and Fe: Mn doped LN can be used for holography memory with higher diffraction efficiency. Cu doped lithium tetraborate single crystal can be used for TLD dosimeter for better performance. Precise measurement of mass of TLD crystal can allow people to measure dose more accurately. By utilizing dual reading scheme one can read first peak of glow curve of TLD immediately just after the irradiation and can get the dose information. Second peak can be used for cumulative dose information in future.